Wind Speed Downscaling of the WRF Model at Subkilometer Scale in Complex Terrain for Wind Power Applications

Francesco Di Paola ⓘ, Domenico Cimini ⓘ, Maria Pia De Natale ⓘ, Donatello Gallucci ⓘ, Sabrina Gentile ⓘ, Edoardo Geraldi ⓘ, Salvatore Larosa ⓘ, Saverio Teodosio Nilo ⓘ, Elisabetta Ricciardelli ⓘ, Ermann Ripepi ⓘ, Mariassunta Viggiano ⓘ, and Filomena Romano ⓘ

Abstract—**Mesoscale numerical weather prediction models are frequently utilized for wind speed analysis and forecasting in the planning and support of wind power generation. However, high computational costs only allow for routine use up to a kilometer scale, which is sometimes too coarse to support onshore wind power generation in areas with complex orography. To address this, an algorithm was developed in southern Italy to downscale the wind fields output using the weather research and forecasting (WRF) model for the first 250 m above ground level. The algorithm is based on artificial neural networks (ANNs) and uses the WRF model outputs on a 1.2 km regular grid, and the land surface height and orientation on a 240 m regular grid to downscale wind fields to a 240 m regular grid. To train the ANNs, a WRF simulation dataset in large eddy simulation (LES) mode was developed. Particular attention was paid to defining the ANN architectures and analyzing inputs to mitigate overfitting risk while maintaining manageable computation costs. The evaluation of outcomes conducted using independent test datasets from WRF-LES simulations reveals that the wind speed root-mean-square difference (RMSD) is 0.5 m/s over land and 0.2 m/s over the sea surface, respectively, at a spatial resolution of approximately 800 m. These figures are lower than the RMSD values of 1.6 m/s over land and 1.0 m/s over the sea surface, accompanied by a spatial resolution of 1.8 km, which were obtained through comparison with the spline interpolation method.**

Index Terms—**Artificial neural network (ANN), downscaling, remote sensing, resolution enhancement, wind speed, weather research and forecasting (WRF), weather research and forecasting large eddy simulation (WRF-LES).**

I. INTRODUCTION

WIND energy production has shown continuous growth over the last few decades and the escalating need to address climate change and reduce greenhouse gas emissions

suggests this growth trend will intensify in the upcoming years [1], [2].

Despite its widespread use and positive prospects, the current global cumulative power capacity of wind energy is 906 GW, with new installations accounting for 78 GW in 2022 alone (Global Wind Energy Council, 2023) [3]. However, the accurate characterization of wind resources is still a considerable forecasting and analytical challenge, especially in areas with complex orography, varied surfaces, land-use types, and terrain roughness. High variability in wind fields significantly impacts the uncertainty of available wind power as it varies roughly with the cube of wind speed [4].

Datasets used for statistical analyses to evaluate existing wind power plants or to support site selection for new installations have significant limitations [5]. Radiosondes and weather balloons, generally the most accurate measuring instruments, provide timely information yet lack widespread territorial coverage. With measurements taken only 2–4 times a day, they fail to capture the daily cycle of wind fields accurately. The Integrated Global Radiosonde Archive [6] shows further limitations regarding vertical resolution. Typically, the first two levels are near the surface, around 10 and 200 m height above ground level (HAGL) respectively, resulting in a data gap from 40 to 140 m HAGL, encompassing most onshore wind turbine heights. Satellite-derived products offer superior spatial coverage but only for the sea surface at 10 m HAGL as Level 2 OCN ocean wind field component with a spatial resolution of 1 km and a revisit time of six days (https://sentinels.copernicus.eu/web/sentinel/ocean-wind-field-component). These products often have a coarse spatial resolution, such as the *global ocean wind products of Copernicus Marine Environment Monitoring Service*, with a daily revisit time and spatial resolution of approximately between 12 and 50 km [7].

The limitations of observational data can often be mitigated using wind data from the global numerical weather models (GNWMs). These models analyze the changes in atmospheric processes by assimilating various types of data, such as in situ measurements, radiosondes, and satellite observations. Notable models include the ERA5 by the European Centre for Medium-Range Weather Forecasts (ECMWF) [8], the *Reanalysis 1 by the* National Centers for Environmental Prediction (NCEP) and National Center for Atmospheric Research (NCAR) [9], and

the NASA *Modern-Era Retrospective analysis for Research and Applications*, version 2 [10]. However, GNWMs typically have relatively coarse spatial resolutions, around 10 km or more, and with only two or three vertical levels below 200 m HAGL [11]. Several statistical approaches have been proposed to counter these limitations by downscaling the horizontal spatial resolution based on a higher resolution dataset or by performing a vertical interpolation to the desired HAGL [12], [13]. The increasing availability of computational resources in recent years has greatly influenced the analysis of wind fields, steering toward the use of mesoscale numerical weather prediction models (NWPMs) in reanalysis mode [14]. Similar to GNWMs, NWPMs simulate the Earth's atmosphere and its evolution over time by numerically solving equations that govern atmospheric processes, albeit at finer spatial scales that can approach 1 km. These numerical weather prediction (NWP) simulations can be used directly or downscaled using various methods, contributing to the development of wind atlases or for specific in situ analyses [15].

Wind resource forecasting is a critical element in wind power distribution [16]. Inaccurate forecasts can lead to an imbalance between energy supply and demand, leading to costs as high as 10% of the total income from energy sales by wind farm operators [17]. This issue arises from the day-ahead market mechanism, where energy producers commit to supplying a certain amount of energy in the upcoming days. If the actual supply differs from that agreed, the energy producers have to pay penalties to offset the costs incurred by transmission system operators in correcting the imbalances caused by inaccurate forecasts [18]. To address this issue, it is vital to provide reliable and accurate forecasts of wind speed at the height of wind turbines [19]. This need can be met by using statistical or physical approaches for wind field forecasting or a combination of both [20], [21].

The physical approach primarily involves NWPMs [22], while the statistical approach is based on the analysis of historical data using various mathematical methods, such as the Kalman filter [23], autoregression [24], wavelet transform [25], artificial neural networks (ANNs) [26], and support vector machine (SVM) [27]. The statistical approach becomes useful when high spatial resolution forecasts are needed, from a few hundred meters up to a specific site, although the time horizon is generally short-term (from 30 min to 6 h [28]), and consequently, it is not suitable for day-ahead electricity markets; therefore, the physical approach is most common for medium-term forecasts, ranging from 6 h to 72–96 h.

For both wind speed reanalysis and forecasting, the use of NWPMs is often the most suitable choice, despite the drawback of grid spacing usually greater than 1 km [29]. In regions with complex terrain, the unresolved subgrid-scale orography can lead to sudden speed-ups, slowdowns, or channelings of the wind flow, or shifts in direction. This results in a deviation between the forecast grid point and the values at the subgrid scale. While state-of-the-art NWPMs can operate at subkilometer scale in a complex terrain [30], the high computational cost makes this approach expensive for operational use [31]. To address this issue,

various studies have focused on downscaling the wind field of the NWPM using deterministic or statistical approaches [32]. A common deterministic method is computational fluid dynamics, which is generally suitable for a single wind farm or areas of a few kilometers due to high computational costs [33]. Statistical approaches primarily employ machine learning algorithms, particularly ANNs and SVMs, often trained using NWP output as input and wind resources, typically the power generated by turbines at a specific site, as output [34]. These methodologies are typically highly accurate yet are often tailored to specific locations. In areas characterized by a dispersed distribution of wind energy plants, such as southern Italy—where wind turbines may be standalone or under different ownerships—appropriate algorithms designed for specific sites may be unavailable. To address this challenge, our research presents a method for the downscaling of wind field simulations produced by an NWPM over a large region with complex topography. The novelty of our method lies in its capacity to bridge between site-specific algorithms and the more generalized output of NWPMs, enhancing resolution from the kilometer to the subkilometer scale while keeping computational demands low. Specifically designed for a region in southern Italy encompassing roughly 150 000 km^2, this technique is capable of downscaling an hour of simulation data in mere minutes, thereby offering a practical solution for its routine application within the operational forecasting processes of NWPMs.

Specifically, the article outlines the wind field resolution enhancement (WiFiRE), which is an algorithm based on ANNs utilizing high-resolution (HRES) surface data to downscale the wind field output of the weather research and forecasting (WRF) NWPM, advanced research WRF core, version 4 (hereafter referred to as WRF) [35]. HRES terrain altitude and orientation were obtained using the digital elevation model (DEM) from the shuttle radar topography mission (SRTM) [36] and were used to drive this downscaling.

The WiFiRE algorithm was designed to operate in southern Italy, where 96.4% of the country's total wind power is produced [37]. Given the region's geographical characteristics, downscaling presents a significant challenge with a peninsular area dominated by the Apennine Mountain range, featuring uneven surfaces, diverse land use, and numerous coastal areas where local thermal and mechanical orographic processes strongly influence wind fields. Thus, local circulation features are often triggered, such as slope winds, mountain-valley breezes, land-sea breezes, and flow splitting by mountains, or channeling in valleys, with spatial scales reaching the microscale (1 km or less) [38].

This article is organized into five sections. Section II explains the fundamental principles of ANNs and associated training algorithms. Section III details the WRF model and the use of its outputs for constructing the training dataset. Section IV introduces the WiFiRE algorithm, along with the selection of inputs, and the configuration and training of the ANNs. Section V outlines the procedure adopted to assess the spatial. Sections VI and VII show and discuss the results, while Section VIII summarizes the conclusions and provides suggestions for future research.

II. ARTIFICIAL NEURAL NETWORK

ANN is a powerful computing system, inspired by biological neural networks that can approximate any complex and non-linear function with a desirable degree of accuracy. This study utilized a feed-forward fully connected multilayer perceptron ANN. The operation, use, and key features of this ANN, employed as a regression model, are extensively outlined in the literature and will, therefore, not be addressed in this study [39], [40].

The ANN's weights and biases were determined using a supervised training process applied to a training dataset consisting of input–output pairs. This process relied on the error back-propagation algorithm, which iteratively adjusts the weights and biases to minimize a suitable cost function—in this study, the mean square error (MSE). Two distinct training algorithms were chosen: the Resilient Backpropagation [41] and the *Levenberg–Marquardt* [42], [43]. While both algorithms are efficient [44], the Resilient Backpropagation is a first-order method with low computational costs [45]. Conversely, the Levenberg–Marquardt is a second-order method, requiring higher computational costs but generally yielding more precise results [46]. Due to its low computational cost, the Resilient Backpropagation algorithm was used to define the number of nodes using a grid search approach. This required the training of numerous ANNs, necessitating an efficient and quick algorithm (see Section IV-C). The Levenberg–Marquardt algorithm was used for input selections (see Section IV-D) and final training (see Section IV-E) to achieve the best-performing ANNs possible.

Appendix A provides detailed information on the operation of the two training algorithms, helping to define the choice of some parameters required for their use, although not critical.

III. WEATHER RESEARCH AND FORECASTING MODEL

The WRF is an atmospheric modeling system, a collaborative effort from various research institutes under the coordination of the NCAR. It is designed for a broad range of applications, from meters to global scale. The system solves the fully compressible, nonhydrostatic Euler equations, using terrain-following hybrid σ-pressure vertical coordinates, with Arakawa C-grid staggering. It is based on time-split integration, using a second- or third-order Runge–Kutta scheme [47].

The WRF was configured and run with three one-way nesting domains at 3.6 km, 1.2 km, and 240 m grid spacings, referred to as $D01$, $D02$, and $D03$, respectively. There were 40 vertical σ-levels, of which 8 were within the initial 250 m HAGL. The weather analysis was conducted using the ECMWF HRES model, which can be found at https://confluence.ecmwf.int/display/FUG/HRES+-+High-Resolution+Forecast (accessed on 04/06/2023). This model features a grid spacing of 0.125° by 0.125° in latitude and longitude, approximately 14 km by 11 km in southern Italy, and 12.5 km on average across both dimensions. The model also boasts a temporal resolution of 6 h, which was utilized for setting the initial and boundary conditions. The model ran in reanalysis mode, using only the weather analysis of the ECMWF HRES, to generate as realistic atmospheric simulations as possible. The

terrestrial data used for $D01$ and $D02$ domains were based on the land use/land cover (LULC) and Global Multiresolution Terrain Elevation Data 2010, both with a nominal spatial resolution of 30 arc-seconds (approximately 900 m), provided by the U.S. Geological Survey [48]. The $D03$ domain, on the other hand, was based on the LULC of the Coordination of Information on the Environment Program with a spatial resolution of 3 arc-seconds (about 90 m) [49] and the DEM of the SRTM with the nominal spatial resolution of 1 arc-second (about 30 m). The primary model settings were as follows:

1) Thompson aerosol-aware microphysics;
2) rapid radiative transfer model for global circulation models short-wave and long-wave radiative schemes;
3) nonlocal Yonsei University scheme for the planetary boundary layer (PBL);
4) Noah land surface model [35], [50], [51].

The D03 was configured in the large eddy simulation (LES) mode [52], [53] to explicitly resolve large turbulence processes within the PBL.

The size and grid spacing of the three domains were chosen to tradeoff computational cost, domain extensions, and the WRF's 3:1 or 5:1 ratio constraint between the grid spacing of parent and child domains. In detail was necessary to maintain, as much as possible, the edge of the so-called "terra incognita" or "gray zone." This refers to the range where grid spacing becomes comparable to the length scale of the most energetic, turbulent eddies. In this range, both 1-D PBL mesoscale schemes and 3-D LES microscale formulations may not accurately resolve turbulent features [54]. The range limit is not clearly defined but could be roughly set between about 1 km and 100 m [55]. The adopted solution was to avoid the gray zone [56], using respectively 1.2 km and 240 m for $D02$ and $D03$ (ratio 5:1), thus preventing unrealistic wind speed oscillations [57].

In the context of the grid size ratio between the global model employed for initialization and boundary conditions and the mother domain of the WRF model, explicit constraints are not defined. However, based on empirical evidence, it is advisable to adhere to the recommended ratios between child and parent domains within the WRF framework, ideally maintaining a 1:3 to a maximum of 1:5 ratio. In our research, the ratio is approximately 1:3.5, aligning with other studies employing the WRF model. For instance, the ECMWF HRES analyses utilized in our study have also been applied in similar contexts, such as in the work by Zhang et al. [58], which featured a mother WRF domain with a 3 km grid spacing (resulting in a ratio of about 1:4.2), and by Arnault et al. [59], where the WRF domain was set at 2.8 km (yielding a ratio of approximately 1:4.5). In the study by Jiménez et al. [60], the global ECMWF Reanalysis - Interim (ERA-Interim) model, with a grid spacing of about 79 km [61], was integrated with a WRF domain of 27 km (achieving a ratio of around 1:2.9). Furthermore, the NCAR, the main contributor to the development of the WRF model, employs the NCEP global forecast system model for operational forecasts. This model, accessible at https://www.nco.ncep.noaa.gov/pmb/products/gfs/ (accessed on 14/02/2024), features a grid spacing of 0.5° in latitude and longitude, roughly equivalent to 50 km. It is coupled with a WRF domain of 15 km, maintaining a grid size

TABLE I
DATES SELECTED FOR BUILDING THE LEARNING DATASET

| Data and time interval (UTC) |
| --- |
| 20-01-2017 07:00 − 21-01-2017 06:00 |
| 21-02-2017 19:00 − 22-02-2017 18:00 |
| 20-03-2017 19:00 − 21-03-2017 18:00 |
| 04-04-2017 19:00 − 05-04-2017 18:00 |
| 25-05-2017 07:00 − 26-05-2017 06:00 |
| 03-06-2017 19:00 − 04-06-2017 18:00 |
| 10-07-2017 07:00 − 11-07-2017 06:00 |
| 08-08-2017 19:00 − 09-08-2017 18:00 |
| 07-09-2017 07:00 − 08-09-2017 06:00 |
| 16-10-2017 19:00 − 11-10-2017 18:00 |
| 24-11-2017 07:00 − 25-11-2017 06:00 |
| 06-12-2017 19:00 − 07-12-2017 18:00 |
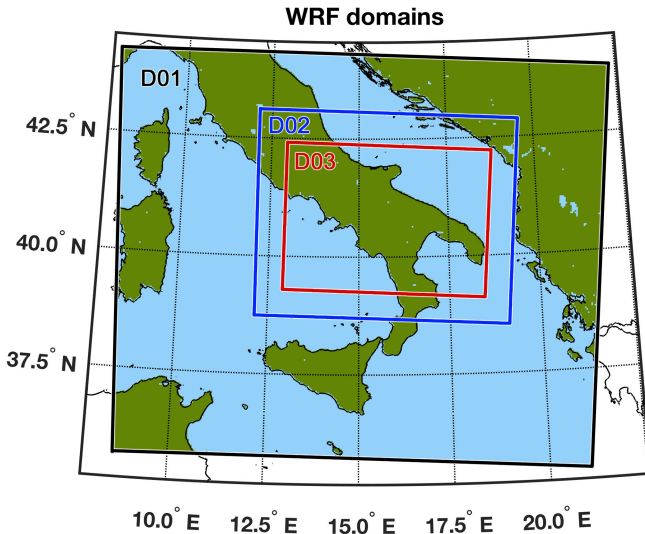
Fig. 1. Domains used in this study—$D01$ at 3.6 km spatial grid (black square), $D02$ at 1.2 km spatial grid (blue), and $D03$ at 240 m (red).

ratio of about 1:3.3, as detailed at https://www2.mmm.ucar.edu/projects/wrf-model/plots/realtime_main.php (accessed on 14/02/2024).

In detail, 12 WRF simulations were executed, one day per month, as listed in Table I. Each lasted 30 h with an output every hour, discarding the first six hours for model spin-up, yielding a total of 288 (12 days × 24 h) simulated scenarios. The days were chosen somewhat randomly but excluding days with similar wind. Fig. 1 presents the three configured domains, with the $D01$ domain consisting of (309 × 259) grid points corresponding to approximately (1108 × 928) km, the $D02$ domain consisting of (489 × 399) grid points corresponding to roughly (586 × 478) km, and the $D03$ domain consisting of (1930 × 1420) grid points corresponding to about (463 × 343) km.

A. Spatial Resolution Analysis of the WRF Output

The key concept behind the development of the WiFiRE algorithm was the training of separate ANNs for different σ-levels. The idea was to use the input–output pairs from the WRF outputs in $D02$ and $D03$ domains as a training dataset. In this way, for routine use, the ANNs can be then applied to the WRF output in the $D02$ domain at 1.2 km grid spacing to generate wind fields at 240 m grid spacing. The outputs from the WRF model in the D02 and D03 domains are derived from terrestrial data with nominal spatial resolutions of 30 arc-seconds and 3 arc-seconds, respectively. Therefore, a variation in spatial resolution between these two domains is anticipated. As a result, the outputs from the ANN are also expected to exhibit a higher spatial resolution compared to their inputs. However, the degree of difference in spatial resolution is unlikely to match the disparity observed between the terrestrial datasets utilized to construct these domains.

However, for the proposed method to work, a strong correspondence is required between the input and output meteorological fields, albeit with different grid model spacing and/or with a different spatial resolution. The former refers to spatial sampling, while the latter pertains to "the scale or size of the smallest unit within an image that is capable of differentiating objects." [62]. Despite these expectations, the analysis of the WRF output revealed a lack of such correspondence.

Take U and V horizontal wind components as examples: U is directed along the model grid's X-axis from left to right and V along the Y-axis from bottom to top. They are similar—although not identical—to the customary zonal and meridional wind components along parallels and meridians. Fig. 2 depicts these fields for the third σ-level (around 60 m $HAGL$) for the WRF simulation of 20-01-2022, 07:00 UTC.

Fig. 2(a) and (b) represents the $D02$ domain, while panels (c) and (d) illustrate the $D03$ domain. Fig. 2(e) and (f) displays the differences in wind components between $D02$ and $D03$ domains sampled at 1.2 km ($D03_{1.2km}$), obtained via a decimation process. This process entails extracting one pixel every (5 × 5) and selecting the one closest to the $D02$ domain's grid points. Despite a general alignment between the wind components of $D02$ and $D03$ (panels (a)–(c) and (b)–(d) look very alike), Fig. 2(e) and (f) reveals that $D02$ values cannot be considered the same as those in $D03_{1.2km}$. This indicates that the wind fields of $D02$ and $D03$ cannot be seen as the same fields with differing spatial sampling.

Reducing the spatial resolution of $D03$ wind fields yielded similar results. This was accomplished by smoothing, using a simple average over an area of (1.2×1.2) km^2, i.e., (5×5) pixel box at 240 m, followed by a decimation process at 1.2 km ($\overline{D03}_{1.2km}$). Fig. 2 does not show this comparison as the images would appear too similar to those of panels (e) and (f). Overall, these results indicate that U and V at 240 m cannot be considered the same as those at 1.2 km, regardless of the greater spatial sampling or increased spatial resolution.

The differences in U and V wind components between the two domains are not confined to the wind fields but generally extend to all meteorological fields of the WRF model. Table II quantifies this analysis not only for atmospheric variables U
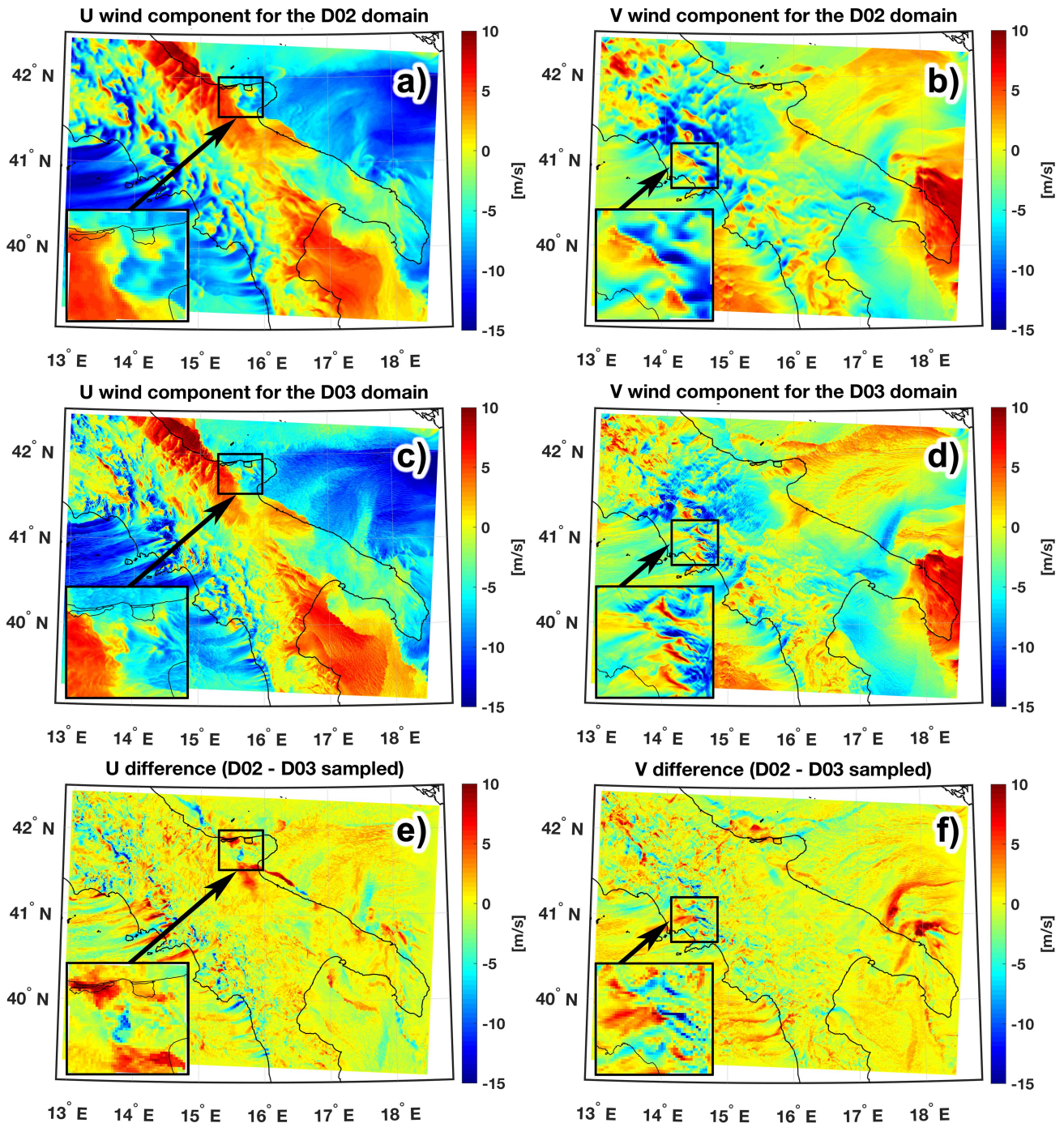
Fig. 2. Comparison of the U and V wind components between $D02$ and $D03$ domains for the third σ-level (60 m $HAGL$) for the 20-01-2017, 07:00 UTC WRF simulation. The lower-left inset in each panel shows a detail zoom to better evaluate the differences between the wind fields in the two domains.

and V but also for other meteorological fields used as inputs for the ANNs. These fields are the *vertical wind component* (W), *temperature* (T), *pressure* (P), *water vapor mixing ratio* (Q), *geopotential height* (H), and *friction velocity* (U^*).

By using all the 288 simulated scenarios, the root-mean-square difference (RMSD) was calculated for each meteorological field, comparing its value on the $D02$ domain with those on the $D03$ domain sampled at 1.2 km ($D03_{1.2km}$, second column), and compared with the standard deviation calculated on the $D02$

domain (fourth column). This could be seen as representative of the within-field variability.

The last two columns report the standard deviation at the kilometer scale, calculated for all the (3×3) and (5×5) pixel boxes of the $D02$ domain, corresponding respectively to (3.6×3.6) km and (6×6) km. Generally, the D02 - $D03_{1.2km}$ RMSD is less than the standard deviation calculated on the $D02$ domain. This suggests an agreement between the atmospheric variables of the two domains. However, it is

TABLE II
COMPARISONS OF RMSDs WITH THE STANDARD DEVIATIONS FOR SELECTED ATMOSPHERIC VARIABLES

Atmospheric variable	a) RMSD $(D02, D03_{1.2km})$	b) RMSD $(D02, \overline{D03}_{1.2km})$	Std. Dev. $(D02)$	(3×3) std. dev. $(D02)$	(5×5) std. dev. $(D02)$
U	1.5 m/s	1.4 m/s	3.1 m/s	0.57 m/s	0.80 m/s
V	1.4 m/s	1.3 m/s	2.6 m/s	0.52 m/s	0.72 m/s
W	0.29 m/s	0.20 m/s	0.18 m/s	0.11 m/s	0.14 m/s
T	0.82 K	0.79 K	2.6 K	0.38 K	0.55 K
P	5.0 hPa	4.0 hPa	38.5 hPa	5.4 hPa	8.2 hPa
Q	0.94 g/kg	0.92 g/kg	2.2 g/kg	0.23 g/kg	0.33 g/kg
H	46 m	37 m	346 m	50 m	75 m

comparable with the local standard deviations calculated on (3 × 3) and (5 × 5) pixel boxes at 1.2 km. This indicates a lack of agreement between the meteorological fields at kilometer scales.

For the W wind component, the alignment is the worst as the $RMSD$ is greater than all the standard deviations, indicating no agreement either on the whole domain or on the kilometric scales. Similar results were observed when analyzing the third column of Table II, showing the RMSD calculated between the variables on the $D02$ domain and those on the $D03$ domain after smoothing and sampling ($\overline{D03}_{1.2km}$). The results in Table II are averages over all the first eight σ-levels, with minimal differences between the various levels.

These discrepancies at the kilometer scale could be attributed both to the differing spatial resolution of LULC and DEM used for the two domains and to the functioning mechanisms of the WRF model. Even though the $D02$ domain output serves as the lateral boundary conditions for the $D03$ domain, the simulations on the two domains run separately and evolve slightly differently due to different terrestrial data, grid spacing, and the scheme used for the large eddies simulation (3-D LES on $D03$ versus 1-D PBL scheme on $D02$).

These differences in the key atmospheric variables between the two domains at the kilometric scale, not solely attributable to variations in spatial resolution or spatial sampling, necessitated a change in approach. Specifically, the atmospheric variables from the $D02$ domain could not be effectively used as input for training the ANNs intended to produce outputs for the $D03$ domain.

B. Constructing the Learning Dataset at 1.2 km

Owing to the significant variances in crucial atmospheric variables between the $D02$ and $D03$ domains, as outlined in Section III-A, the inputs for the ANN training process cannot be based on the WRF simulations in the $D02$ domain (hereafter referred to as true fields). As such, it is imperative to reproduce them using the WRF simulations in the $D03$ domain by downgrading their spatial resolution and sampling them at the $D02$ grid points (hereinafter referred to as synthetic fields). This approach yielded synthetic fields with the same spatial characteristics to those of the true fields in the $D02$ domain but in full coherence with those in the $D03$ domain. To calculate the synthetic fields, which involves the smoothing and sampling of the WRF outputs of the $D03$ domain, a convolution process with

a two-dimensional Gaussian filter was performed. This process was subsequently followed by sampling the results on a 1.2 km grid

$$\bar{x}_{1.2km}(x,y) = [x_{240m}(x,y) * g_\sigma(x,y)]_{1.2km} \quad (1)$$

where $*$ denotes the convolution operator, $[\cdot]_{1.2km}$ denotes the decimation process needed to reduce the sampling to 1.2 km. x_{240m} is the generic WRF output on the $D03$ domain, $\bar{x}_{1.2km}$ is the resulting smoothed and sampled value, x and y are the spatial coordinates, and g_σ is the sampled Gaussian kernel based on the radially symmetric Gaussian function f_σ with zero mean and identical standard deviation $\sigma_x = \sigma_y = \sigma$ on the two axes [63]

$$f_\sigma = \frac{1}{2\pi\sigma} e^{-\frac{x^2+y^2}{2\sigma^2}}. \quad (2)$$

The kernel g_σ is a square matrix with an odd number of values in both dimensions, obtained by sampling f_σ at 240 m and truncating along the x and y axes to 3σ, followed by normalizing the sum of its values to 1.

The full-width at half-maximum (FWHM) of g_σ relates to the standard deviation according to Sobrino and Jiménez-Muñoz [64]

$$\text{FWHM} = 2\sqrt{2ln2}\,\sigma \cong 2.355\,\sigma. \quad (3)$$

Similarly to instrumental observations, the FWHM can serve as a measure to characterize the spatial resolution of the smoothed image [65]. The convolution of (1) can be resolved using the discrete Fourier transform (DFT) of each term, which transforms this operation into a simple product [66]

$$x_{240m}(x,y) * g_\sigma(x,y) = \text{DFT}^{-1}[X_{240m}(u,v) \cdot G_\sigma(u,v)]. \quad (4)$$

The inverse operation of the DFT is indicated by DFT^{-1}, u and v are the spatial frequency coordinates, and $X_{240m}(u,v)$ and $G_\sigma(u,v)$ are the Fourier transforms of $x_{240m}(x,y)$ and $g_\sigma(x,y)$, respectively, calculated using the fast Fourier transform algorithm [67].

A one-dimensional grid search approach was used to identify the optimal width of the Gaussian kernel g_σ, which functions as a low-pass filter to align the spatial resolutions of the smoothed and sampled WRF outputs in the $D03$ domain with those in the $D02$ domain as closely as possible. The FWHM was varied from 0 to 5000 m in 10 m increments. For each FWHM value, the resulting field $\bar{x}_{1.2km}(x,y)$ was computed, and its DFT $\bar{X}_{1.2km}^{HW}(u,v)$ was compared with the corresponding DFT $X_{1.2km}^{HW}(u,v)$ in $D02$ domain. The superscript HW
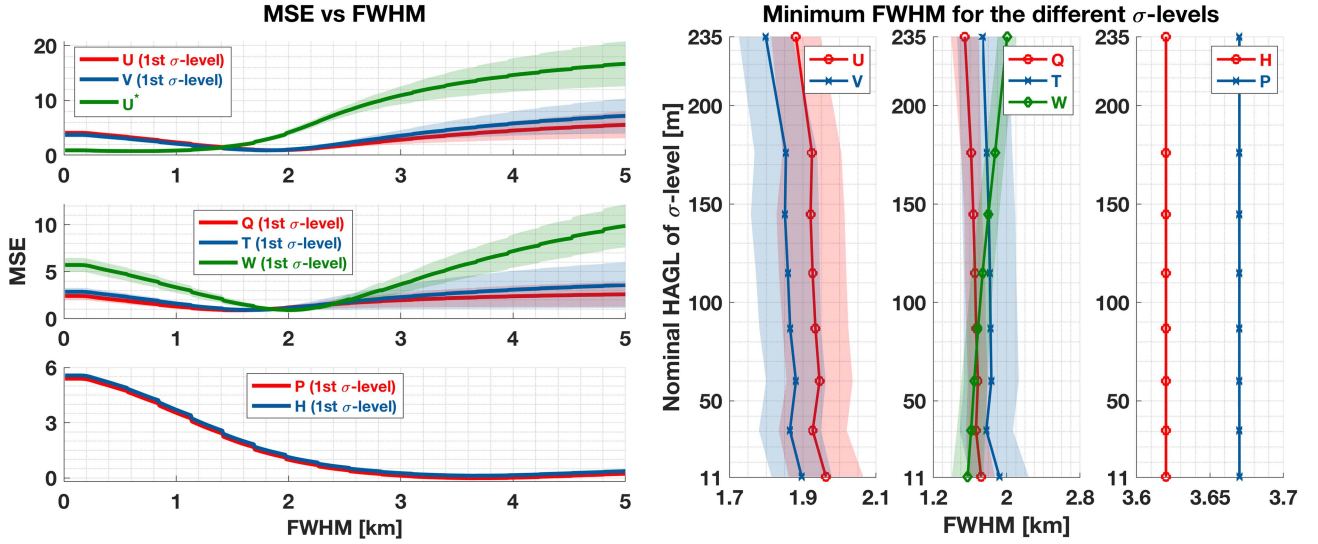
Fig. 3. Left panels display the mean and standard deviation of the MSE of the DFT amplitude against the FWHM for the first σ-levels; right panels show the mean and standard deviation of the minimum FWHM for the different σ-levels.

denotes the windowing of the considered fields $\bar{x}_{1.2\text{km}}$ and $x_{1.2\text{km}}$ applied before the DFT calculation. This was done using the Hanning window to minimize spectral leakage to higher frequencies due to the rectangular domain [68]. In detail, the windowing operation was performed by weighting each element of the matrices $\bar{x}_{1.2\text{km}}$ and $x_{1.2\text{km}}$ with the corresponding element of the matrix calculated using the following matrix multiplication (row-by-column multiplication):

$$HW = hw_{x-\text{axis}} \cdot hw_{y-\text{axis}} \quad (5)$$

where row $hw_{x-\text{axis}}$ and column $hw_{y-\text{axis}}$ are both defined as the one-dimensional Hanning window

$$hw\,(t) = \begin{cases} 0.5 + 0.5 \cos\left(\frac{2\pi t}{T-1}\right), & \text{if } 0 \le t \le T-1 \\ 0, & \text{otherwise} \end{cases} \quad (6)$$

where t is the index along the x-axis or y-axis, and T is the corresponding number of grid points. The comparison between $\bar{X}_{1.2\text{km}}^{HW}$ and $X_{1.2\text{km}}^{HW}$ was performed in terms of the natural logarithm of the amplitudes $A(u,v)$ [69]

$$A\,(u,v) = \sqrt{R(u,v)^2 + I(u,v)^2} \quad (7)$$

where $R(u,v)$ and $I(u,v)$ are the real and imaginary parts of the considered DFTs.

The amplitudes $A_{\bar{X}_{1.2\text{km}}}(u,v)$ and $A_{X_{1.2\text{km}}}(u,v)$ of $\bar{X}_{1.2\text{km}}(u,v)$ and $X_{1.2\text{km}}(u,v)$ were used to calculate the MSE

$$\text{MSE} = \frac{1}{N \cdot M} \sum_{u=1}^{N} \sum_{v=1}^{M} \left\{ ln \left[\left(A_{\bar{X}_{1.2\text{km}}}\,(u,v) \right) \right] \right.$$
$$\left. - ln\,[A_{X_{1.2\text{km}}}\,(u,v)] \right\}^2. \quad (8)$$

Finally, the FWHM that minimizes the MSE of (8) was selected to perform the smoothing and subsequent sampling of the WRF output on the $D03$ domain. This procedure was performed for each of the 288 simulated scenarios, and all the WRF fields deemed inputs or outputs for the ANNs, as elaborated in Section IV-A. These consist of $U, V, W, P, Q, T,$ $H,$ and U^*.

The left panels of Fig. 3 summarize this procedure for the aforementioned fields for the first σ-level (except U^* which is a surface variable). They illustrate the trend of the mean and standard deviation of the MSE of (8) calculated on the 288 simulated scenarios against the FWHM, while the right panels display the mean and standard deviation of the minimum FWHM for each σ-level. The mean values and the standard deviation of FWHMs for the different fields calculated on the 288 simulated scenarios and averaged across the first 8 σ-levels are also listed in Table III. For fields $U, V, W, Q,$ and $T,$ the mean FWHM values range in approximately [1.6–1.9] km with standard deviations ranging from about [0.1–0.3] km. For H and P, the mean value reaches about 3.7 km with a negligible standard deviation. For U^*, the mean and standard deviation are about 0.64 km and 0.18 km, respectively.

Fig. 4 presents an example of the true U wind component first σ-level for $D03$ and $D02$ domains, for the simulated scenario of February 21, 2017, at 21:00 UTC, and the corresponding DFT log-amplitudes. The spatial frequencies increase outward from the center, starting from the zero-frequency corresponding to the mean value, and ascending to the maximum values at the edges that match the highest spatial resolution [70]. Fig. 4(a) demonstrates a higher spatial resolution and sampling than panel (c), and correspondingly, the DFT log-amplitude for the $D03$ domain; panel (b) displays not only a higher limit value for its spatial frequency (approximately 2.1 km^{-1}) than panel (d) for the $D02$ domain (0.4 km^{-1}) but also greater magnitudes for the same spatial frequencies. Fig. 5 shows three distinct smoothings of the U wind field (synthetic field), calculated by applying

TABLE III
MEAN AND STANDARD DEVIATION CALCULATED ACROSS EACH SIMULATED SCENARIO AND AVERAGED ACROSS ALL σ-LEVELS OF THE FWHMS OF THE
GAUSSIAN FILTERS USED FOR SMOOTHING THE WRF OUTPUTS

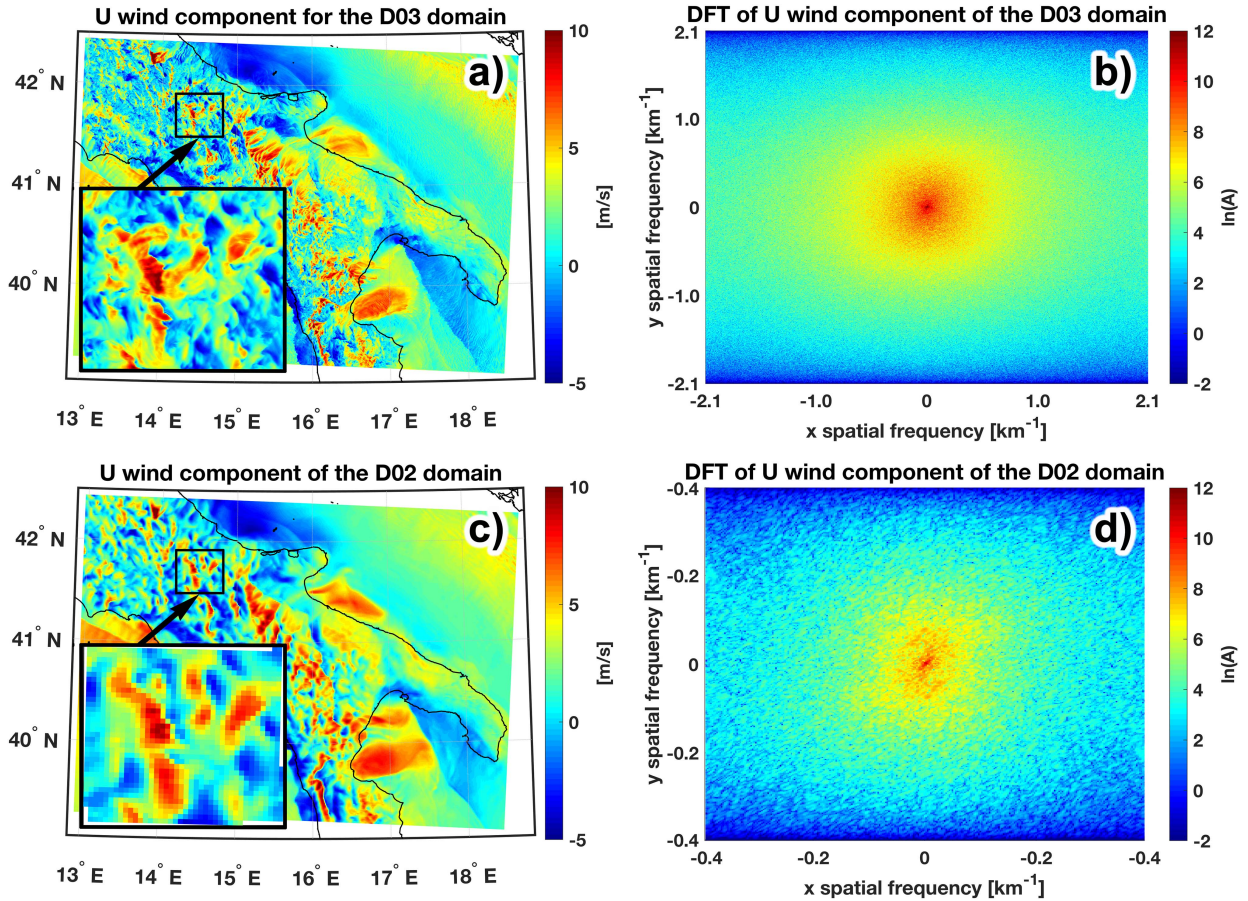|	U	V	W	T	Q	P	H	U*
Mean [km]	1.93	1.86	1.74	1.81	1.65	3.67	3.67	0.64
Std. Dev. [km]	0.09	0.08	0.13	0.29	0.12	<0.01	<0.01	0.18

Fig. 4.   Example analysis of the U wind component for the first σ-level for the simulated scenario of February 21, 2017, at 21:00 UTC. Panels (a) and (c) depict the U wind component for D03 and D02 domains, respectively, while panels (b) and (d) display the log-amplitudes of the corresponding DFTs.

three g_σ kernels with FWHM equal to 0.50 km, 1.91 km, and 3.0 km to the true U wind component at 240 m [see Fig. 5(a)] and the corresponding DFT log-amplitudes. The intermediate smoothing was chosen using the previously described procedure, with its value aligning with the minimum value of the red line in Fig. 3. The other two values were chosen for comparison. The DFT log-amplitudes in Fig. 5(b), (d), and (e) reveal a progressive reduction of their values at high spatial frequencies, with that relating to FWHM = 1.91 km [see Fig. 5(d)] being the most similar among the three to that corresponding to the true U wind component at 1.2 km [see Fig. 4(d)]. This conclusion aligns with a more accurate resemblance in terms of spatial resolutions demonstrated in the lower left insets between Figs. 4(c) and 5(c), compared to Fig. 5(a) or (d). As a result of this analysis, the smoothed field depicted in Fig. 5(c), obtained with FWHM = 1.91 km, was used to construct the ANN training dataset. This was performed alongside other inputs, smoothed in the same manner, and coupled to the HRES outputs as in Fig. 4(a).

IV. WiFiRE ALGORITHM

The WiFiRE algorithm was designed to downscale U and V horizontal wind components. Its foundation includes 16 ANNs, 8 for each of the two wind components, for all 8 vertical σ-levels. The mean HAGL, from the average of the 12 WRF simulations on the WRF domain $D03$, is approximately 11, 35, 60, 87, 115, 145, 176, and 235 m, henceforth known as the nominal HAGL. This upper limit was selected considering the increasing global trend in onshore turbine height [71]. As detailed in the next section, each ANN calculates the downscaled principal components (PCs) [72] of U and V at (7×7) grid points at 240 m, centered around each grid point at 1.2 km, as shown by the left panel of Fig. 6 which also shows the input for each ANN consisting of the PCs of some meteorological fields at (5×5) and (3×3) grids at 1.2 m. The input also includes the PCs of some static surface fields computed on the same (7×7) box at 240 m used for the output.
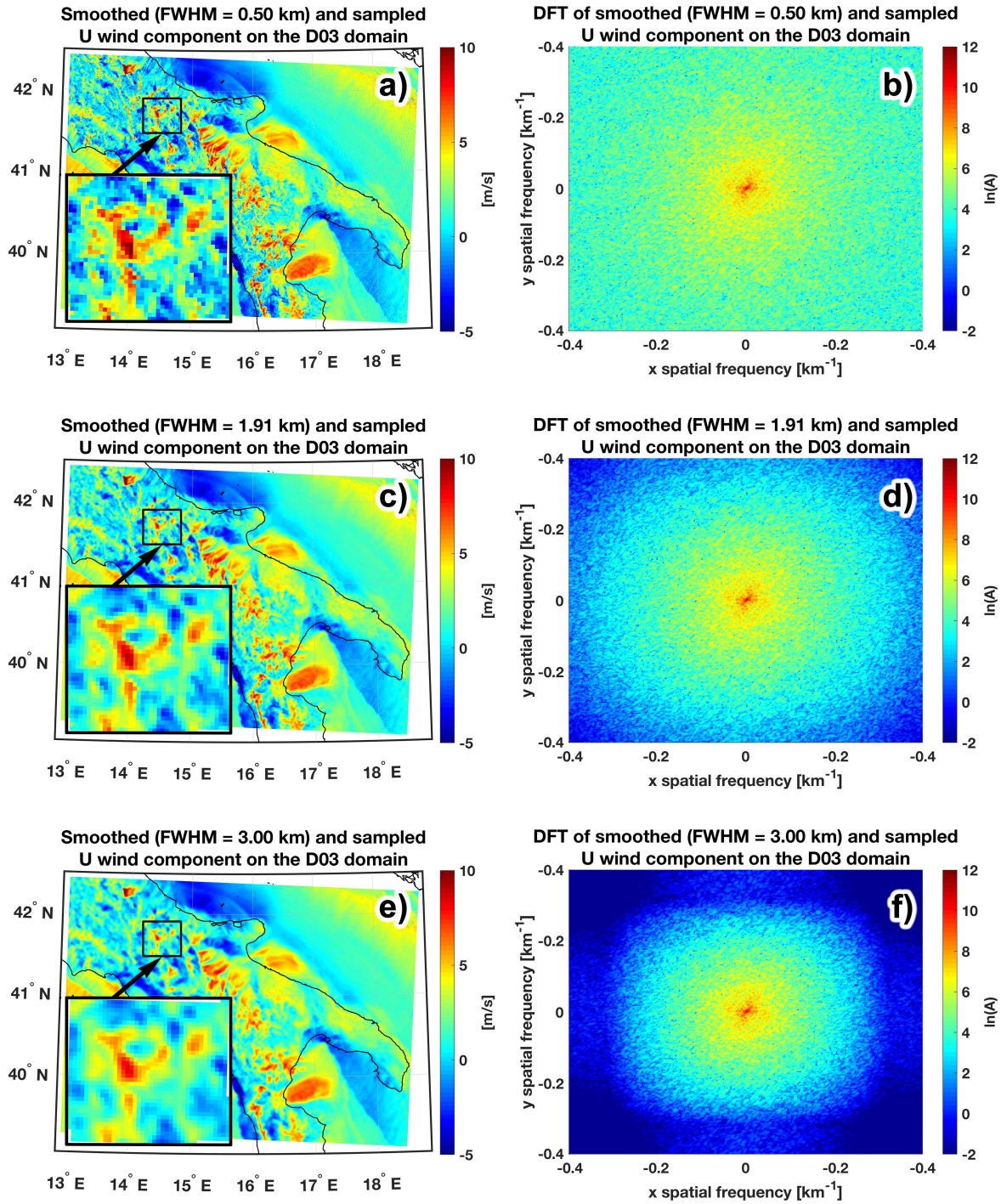
Fig. 5. Example analysis of the U wind component for the first σ-level for the simulated scenario of 21-02-2017, 21:00 UTC. Panels (a) and (c) depict the U wind component for D03 and D02 domains, respectively, while panels (b) and (d) display the log-amplitudes of the corresponding DFTs.

Despite the (5×5) box for the output might seem more consistent due to the ratio between the two $D02$ and $D03$ domain grid spacings being 5 [1.2 km–240 m], the larger (7×7) box was favored. This approach allows two or four ANN output overlapping between adjacent boxes, thus avoiding the boxy artifact [73]. As a result, the WiFiRE algorithm's final output at the edge of each (5×5) box can be obtained by merging 2 or 4 overlapping outputs. This is achieved using coefficients

computed with the inverse weighted distance from the grid point at 240 m and the central one at 1.2 km

$$a_p = \frac{b_p}{\sum_{p=1}^{P} b_p} \tag{9}$$

where P is the number of overlapping ANN outputs (2 or 4), p is the index ranging from 1 to P, b_p is the inverse distance between the grid point at 240 m and the central one at 1.2 km related to
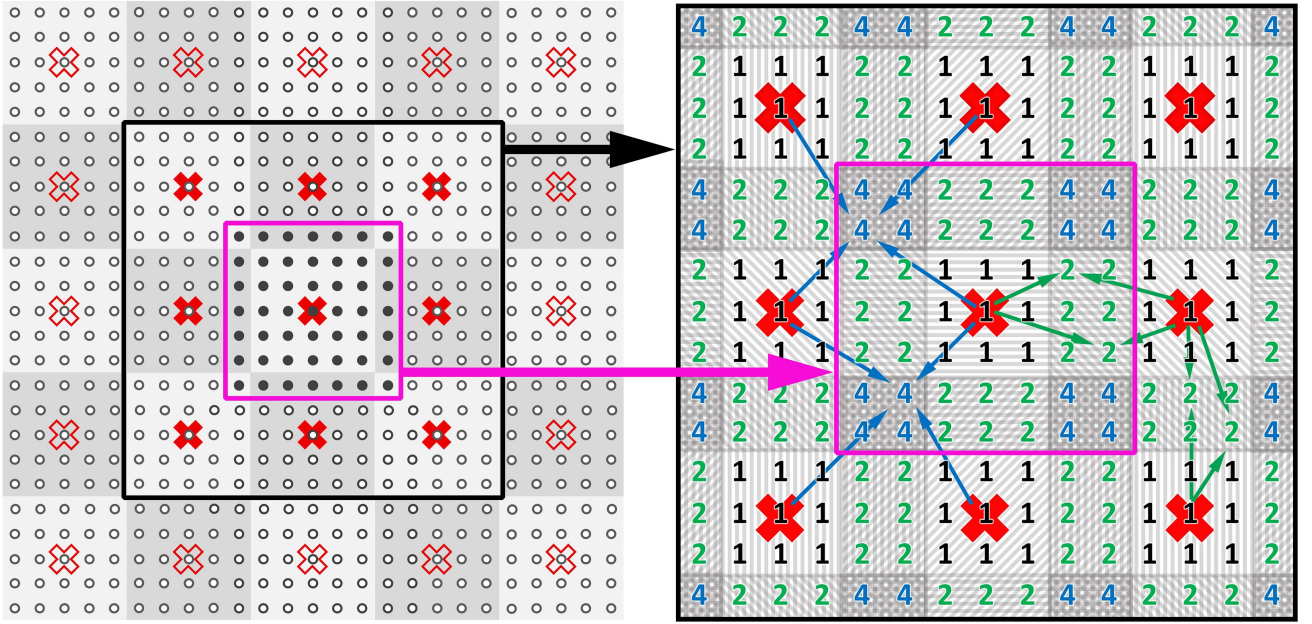
Fig. 6.   Left: A geometric scheme of grid points for the D02 domain at 1.2 km (marked by red cross markers, both empty and filled) and the D03 domain at 240 m (indicated by black circle markers, both empty and filled). The periodic alternation of light and dark gray boxes underscores the correspondence between the (5×5) grid points at 240 m and the central 1.2 km grid point within these boxes. Right: the WiFiRE output reconstruction process. For grid points marked with black "1" flags, the algorithm's output comes from a single ANN output. In overlapping areas marked by green "2" flags, the algorithm output utilizes the IDW mean of the two nearest ANN outputs, with pairs of green arrows representing distances. For the grid points at overlapping corners flagged with blue "4," the algorithm output is achieved using the IDW mean of the four closest ANN outputs, with the four blue arrows indicating distances.

two or four outputs, and a_p is the coefficient used to calculate the combination of the outputs. The right panel of Fig. 6 illustrates the distances grid and the overlapping ANN outputs.

When the WiFiRE algorithm gets in input the WRF outputs on the $D02$ domain at 1.2 km and the surface static fields on the $D03$ domain at 240 m, it delivers U and V downscaled to the same grid of the $D03$ domain at 240 m for the first eight σ-levels.

A. Input and Output Definitions

The learning dataset for each ANN was assembled by coupling certain input and output vectors, most of which were from the principal component analysis (PCA) of a particular field computed on a specific spatial scheme. In all PCAs, the selected components are those explaining 99.9% of the variance of the relative field.

The ANN output consists of the PCs computed on the (7×7) grid points at 240 m of the variable to be downscaled, i.e., U and V separately (represented by the filled black circle marker in the left panel of Fig. 6). To calculate the PCs, 49 values of the (7×7) box were arranged from left to right and from bottom to top, as depicted in Fig. 7.

The selection of the ANNs' inputs, the so-called features, was carried out in two stages. The first stage, detailed in this section, considered the PCs of a few variables that may correlate with the ANNs output or that could help characterize both the atmospheric conditions and the Earth's surface. The second stage, detailed in Section IV-D, discarded less important or irrelevant features.
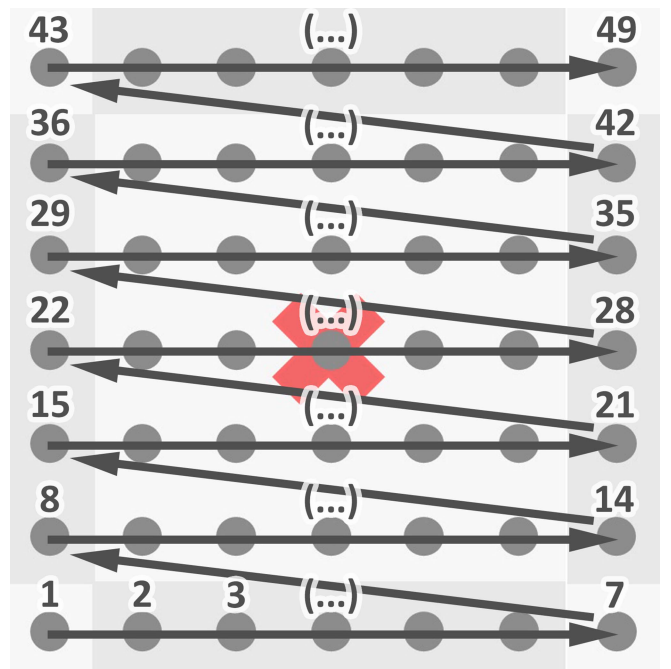

Fig. 7.   Rearrangement order of the ANNs output in the (7×7) box for PCA.

The preliminary input for U and V downscaling consists of four variable sets.

1) Three sets of PCs of the U, V, and H fields corresponding to the (5×5) grid points at 1.2 km, as illustrated in the left panel of Fig. 6 with both empty and filled red cross

markers. The PCs were performed by arranging the (5×5) values from left to right, and from bottom to top, similar to the output.

2) Seven sets of PCs of meteorological fields corresponding to the (3×3) grid points at 1.2 km, as shown in the left panel of Fig. 6 with filled red cross markers, rearranged from left to right, and from bottom to top. The selected fields included the horizontal wind speed (WS) due to its close correlation with U and V output, W, P, T, Q, and air density (D), offering additional information on atmospheric conditions, and U^*, useful for characterizing wind shear at the boundary [74].

3) Six sets of PCs of static fields related to the Earth's surface, corresponding to the same (7×7) grid points at 240 m used to define the output. These static fields include surface altitude (HGT), surface roughness length (SRL), land fraction (LF), and the three components of the versor normal to the Earth's surface (VN and VE parallel to the $D02$ model grid, northward and eastward respectively, and VZ orthogonal to both VN and VE and directed toward increasing altitudes). These inputs were used due to the close relationship between the wind field and the orography to introduce information at 240 m, and thereby to guide the downscaling process. Although the algorithm was designed for downscaling over land surface, LF input was considered to evaluate potential land/sea surface interactions with the downscaling, due to the large coastal areas of the Italian peninsula, and to develop an algorithm that can also work on the sea surface.

4) Three single values for Latitude (LAT), Longitude (LON), and the cosine of the solar zenith angle (SZA) corresponding to the central position of the (7×7) box, as shown in the left panel of Fig. 6, where the filled black circle marker overlays the filled red cross marker.

The first two input sets were chosen at the same level as the output variable, except for U^*, which is single level, while the last two sets were constant for all ANNs, irrespective of the σ-level of the output to be downscaled. The input areas in the first two sets, corresponding to the (5×5) and (3×3) grid points at 1.2 km, were selected based on their relevance to the outputs. The largest area was chosen for U and V input features as they were considered most correlated with the U or V outputs at 240 m, and for H to explore the importance of altitude as an input while the smallest area was chosen for less important features. U and V downscaling was prioritized over direct WS downscaling to leverage the relationships between them and the surface geometry, which can both guide and impede the two components.

The PCAs of U, V, H, W, P, T, Q, WS and D, used for both input and output, was conducted separately at each σ-level. This was done using all (7×7) boxes at 240 m, or all (5×5) or (3×3) grid boxes at 1.2 km across the 288 simulated scenarios. Likewise, the PCA for U^* used all (3×3) grid points at 1.2 km from all the simulated scenarios. The PCAs for the static fields related to Earth's surface used all (7×7) grid point boxes at 240 m within the $D03$ domain.

The WS input was obtained by applying the static WRF outputs *COSALPHA* and *SINALPHA* to convert the horizontal wind components from grid-relative (U and V) to Earth-relative ($\hat{U}$ and $\hat{V}$) [75], given

$$\hat{U} = U \cdot COSALPHA - V \cdot SINALPHA \quad (10)$$

$$\hat{V} = V \cdot COSALPHA + U \cdot SINALPHA \quad (11)$$

$$WS = \sqrt{\hat{U}^2 + \hat{V}^2}. \quad (12)$$

The D input was derived as

$$P_{WV} = \frac{P \cdot Q}{\varepsilon + Q} \quad (13)$$

$$P_{AD} = P - P_{WV} \quad (14)$$

$$D = \frac{P_{AD}}{R_{AD} \cdot T} + \frac{P_{WV}}{R_{WV} \cdot T} \quad (15)$$

with P_{WV} as the water vapor pressure, $\varepsilon = 621.97$ as the ratio of molecular weights of water and dry air, P_{AD} as the air-dry pressure, $R_{AD} = 287.05$ J·kg^{-1}·K^{-1} and $R_{WV} = 461.495$ J·kg^{-1}·K^{-1} as the gas constants for dry air and water vapor and (15) contain the sum of the universal gas laws for dry air and water vapor [76], [77]. Even though WS and D are derived from other fields already provided as inputs, they can enhance the ANN performance when used as additional inputs. This is because feature engineering can significantly contribute to machine learning [78].

The WRF preprocessing system tool [79] directly provides the static fields HGT and SRL. The parameters VN, VE, and VZ are calculated based on the terrain slope (SL) and aspect (AS) [80]. SL represents the degree of incline of the earth's surface, with a zero-value indicating flat terrain, while AS is the horizontal orientation, measured clockwise in degrees from 0 to 360°. Calculations for SL and AS involve the use of HGT gradients along the y and x axes of the $D03$ domain grid. This process also represents feature engineering, such as that used for *WS* and *D*. As shown in Fig. 8, using the HGT values in the (3×3) grid spacing at 240 m as the z-axis, the two gradients δ_z/δ_y and δ_z/δ_x at the central point (x, y) were calculated by using its eight neighbors [81] with

$$\frac{\delta_z}{\delta_y} = \frac{(z_{x+1,y+1} + 2z_{x,y+1} + z_{x-1,y+1})}{}$$
$$+ -\frac{(z_{x+1,y-1} + 2z_{x,y-1} + z_{x-1,y-1})}{8\Delta y} \quad (16)$$

$$\frac{\delta_z}{\delta_x} = \frac{(z_{x+1,y+1} + 2z_{x+1,y} + z_{x+1,y-1})}{8\Delta x}$$
$$+ -\frac{(z_{x-1,y+1} + 2z_{x-1,y} + z_{x-1,y-1})}{8\Delta x} \quad (17)$$

where $\Delta x = \Delta y = 240$ m. The gradient δ_z/δ_y was calculated by weighing twice the vertical gradient passing through the central point, i.e., $(x, y + 1) \rightarrow (x, y) \rightarrow (x, y - 1)$ and once each of the two vertical gradients adjacent. Similarly, the gradient δ_z/δ_x is obtained by weighing twice the horizontal
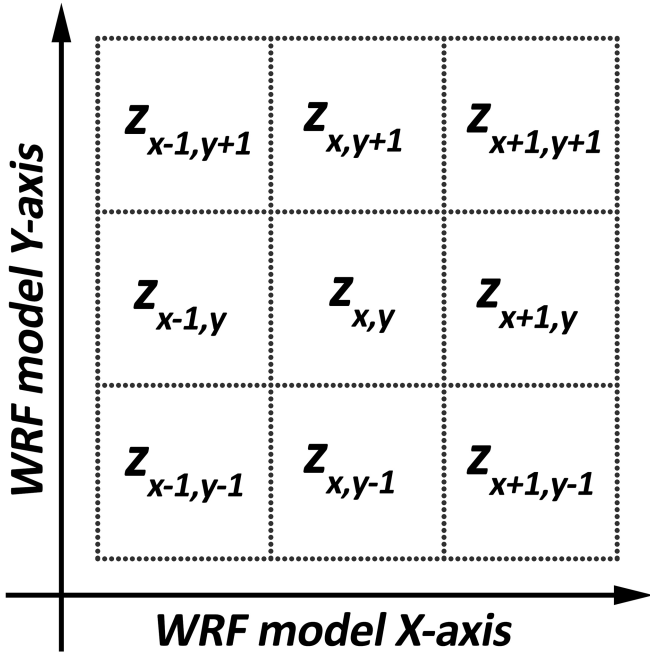
Fig. 8.   Layout of the HGT values in the (3×3) grid spacing at 240 m, used for calculating slope and aspect.

gradient $(x+1, y) \rightarrow (x, y) \rightarrow (x-1, y)$, and once each the two adjacent horizontal gradients. SL and AS were obtained as a function of the two gradients, by means of

$$SL = \text{atan} \left(\sqrt{ \left(\frac{\delta_z}{\delta_x} \right)^2 + \left(\frac{\delta_z}{\delta_y} \right)^2 } \right) \tag{18}$$

$$AS = \begin{cases} 90° - \frac{180°}{\pi} \text{atan} \left(\frac{\frac{\delta_z}{\delta_y}}{\frac{\delta_z}{\delta_x}} \right), & \text{if } \frac{\delta_z}{\delta_x} < 0 \\ 270° - \frac{180°}{\pi} \text{atan} \left(\frac{\frac{\delta_z}{\delta_y}}{\frac{\delta_z}{\delta_x}} \right), & \text{otherwise} \end{cases}. \tag{19}$$

Finally, the three components VZ, VN, and VE of the versor, normal to the terrain surface, are calculated as follows:

$$VZ = \cos(SL) \tag{20}$$

$$VN = \sin(SL) \cdot \cos(AS) \tag{21}$$

$$VE = \sin(SL) \cdot \sin(AS). \tag{22}$$

Table IV provides a summary of the size of the physical parameters chosen for the preliminary inputs and the outputs of the ANNs, and their down-size downstream of the PCs that reduced the number of the inputs and outputs by about 30% and 50%, respectively, for both U and V downscaling.

B. Reducing the Learning Dataset

The learning dataset comprises simulations from the WRF model, spanning 12 days at 24-h intervals, resulting in 288 distinct scenarios. For each scenario, the dataset for training the ANNs consisted of input–output pairs from a grid of 386 by 284

points, each with a spatial resolution of 1.2 km. This configuration yielded a total of over 30 million input–output pairs across the entire dataset for each of the eight σ-levels, collectively referred to as the Learning dataset. Due to the extensive number of training patterns, combined with the size of the initial inputs and outputs, the computational burden of training 16 ANNs was nearly overwhelming. As a result, it was necessary to scale down the full Learning dataset to manage the computational demands. Two different reductions were performed for each of the 16 ANNs. The first, comprising approximately $N = 10^5$ samples (hereafter DB100k), was used to design the ANNs, defining their architectures and reducing the input features. The second, with roughly $N = 10^6$ samples (hereafter DB1M), was used to refine the weights and biases calculated in the design phase.

To reduce the dataset, a similar approach to the one described by Di Paola et al. [82] was adopted. This involved building an M-dimensional histogram, with one dimension for each variable, and grouping the full dataset into several bins with each bin containing samples with similar characteristics. The reduced dataset was then created by randomly selecting a single sample from each bin. Specifically, $M = 9$ was set, with M variables including the date ($DATE$) of the WRF simulation (see Table I), the mean values of variables LAT, LON, SZA, HGT, U, and V, and the standard deviations of U and V in the (7×7) grid points at 240 m. This selection ensured the reduced dataset of the entire area (LAT, LON), time of day (SZA), ground elevation (HGT), time of year ($DATA$), and wind speeds and directions, along with their local variability.

To build the 16 small datasets DB100ks, two datasets for U and V for each of the eight σ-levels, $DATE$ was divided into $ki = 4$ equal intervals, one for each season, the mean values of LAT, LON, SZA, HGT were divided into $gi = 5$ equal intervals. The number of xi intervals for the means and standard deviations of U and V was determined through an iterative approach, starting from $xi = 1$. With each iteration, the corresponding M-dimensional histogram was developed, and the reduced dataset was then constructed by randomly picking one sample from each bin. If the number of samples N was less than 10^5, xi was incremented by 1 and a new iteration was performed. For the small U and V datasets, nine iterations were conducted for each vertical level, thereby setting $xi = 9$. This resulted in slightly more than $N = 10^5$ samples for each small dataset and each σ-level. Although the number of bins exceeds 10^5 ($ki \cdot gi^4 \cdot xi^4 \cong 1.6 \times 10^7$), only a small fraction (0.1%) of the total number of bins was populated.

For the 16 large datasets DB1Ms, the parameters were $ki = 12$ (one interval for each simulated date, Table I), $gi = 10$ for the intervals of LAT, LON, SZA, and HGT. Consequently, following the iterative process, $xi = 11$ was achieved for the resulting number of intervals for the means and standard deviations of U and V, accounting for a total of 1.8×10^9 bins. Just over $N = 10^6$ of these were populated with at least one sample. With this dataset building method, approximately 10% of DB100ks and DB1Ms were located over sea, and the remaining 90% over land. The DB1Ms and DB100ks datasets were randomly divided into three distinct datasets: Training, Validation, and Test, distributed in a ratio of 60:20:20. The

TABLE IV
NUMBER OF INPUTS AND OUTPUTS USED FOR EACH ANN FOR *U* AND *V* DOWNSCALING

σ-level	PCs of 49 outputs (7×7) @240m	PCs of 25 inputs (5×5) @1.2m			PCs of 9 inputs (3×3) @1.2km							PCs of 49 inputs (7×7) @240m						Total inputs
		U	V	H	W	WS	P	Q	T	D	UST	HGT	RL	VE	VN	VZ	LF	
#1	U 31 / V 32	20	21	10	9	9	6	6	6	5	9	11	49	39	25	25	47	300
#2	U 28 / V 29	19	20	10	9	9	6	7	6	5	9							299
#3	U 26 / V 27	19	20	10	9	9	6	7	6	5	9							299
#4	U 25 / V 26	19	19	10	9	9	6	7	6	5	9							298
#5	U 25 / V 25	18	19	10	9	8	6	7	6	5	9							296
#6	U 24 / V 24	18	19	10	9	8	6	7	6	5	9							296
#7	U 25 / V 25	18	19	10	9	8	6	8	6	5	9							297
#8	U 22 / V 22	17	18	10	9	8	6	7	5	5	9							293

The total inputs also consider latitude, longitude, and the cosine of the solar zenith angle. The PCs of 49 inputs @240 m are common to all the σ-levels because they are relative to the Earth's surface.

Training dataset served to calculate weights and biases using the two algorithms mentioned earlier. The Validation dataset facilitated the fine-tuning of ANN parameters, including the number of nodes and the number of epochs during the training phase. The Test dataset is used in the development phase, enabling the evaluation of various options and conducting initial tests.

C. Architecture of the ANNs

Defining the architecture of the ANNs entailed the determination of the number of hidden layers, the number of nodes in each hidden layer, and the transfer functions for both the hidden and output layers. Aside from heuristic approaches reliant on expert experiences or rules of thumb, the trial-and-error method is a common approach for designing the ANN architecture [83], [84]. However, this method is time-consuming as it involves designing, training, and testing multiple ANNs, varying the number of hidden layers and nodes, and the transfer functions, and finally choosing the most fitting architecture. This exhaustive approach must be repeated for each of the 16 different ANNs, which makes it impractical. To mitigate the computational cost, certain simplifications were necessary.

The first simplification concerned the transfer functions, which were set as pure lines for the output layer and hyperbolic tangent for the hidden layer

$$\tanh(x) = \frac{e^x - e^{-x}}{e^x + e^{-x}}. \tag{23}$$

This usually yields the best results among other sigmoid functions [85]. This is possible as any feedforward ANN with at least one hidden layer containing a sufficient number of nodes, with an arbitrary bounded, nonconstant activation function in

the hidden layer, such as the hyperbolic tangent, and a pure line activation function in the output layer, can approximate continuous functions under very general conditions [86], [87]. Consequently, the choice of transfer functions is not crucial and can be predetermined as indicated, excluding it from the trial-and-error search.

Moreover, based on these considerations, the number of hidden layers can be preset to one. However, two hidden layers are usually preferred as they provide benefits such as fewer total nodes, higher efficiency of the training algorithms, and better generalization ability than a single hidden layer [88]. There is no theoretical reason to use more than two hidden layers for this study [89]. Given these considerations, the number of hidden layers was set to two, therefore eliminating the selection of this parameter from the trial-and-error search.

The trial-and-error method was used to determine the number of nodes on the two hidden layers. Using the Resilient Backpropagation algorithm with the reduced datasets DB100k, an initial architecture with just one node on both hidden layers was trained. This was followed by the comparison of two different ANN architectures using an iterative procedure, each was obtained by incrementing the number of nodes by one unit, separately on the first and second hidden layers. The configuration that produced the minimum MSE calculated on the Validation dataset was chosen for each iteration. Five ANNs were trained for each configuration, using five different random initializations of weights and biases. The best-performing configuration was chosen each time. The iterative procedure concluded when the progressive addition of nodes on the two hidden layers led to ten consecutive increases in the three-point moving average of the MSE evaluated on the Validation dataset, indicating that further increasing the nodes would not significantly enhance
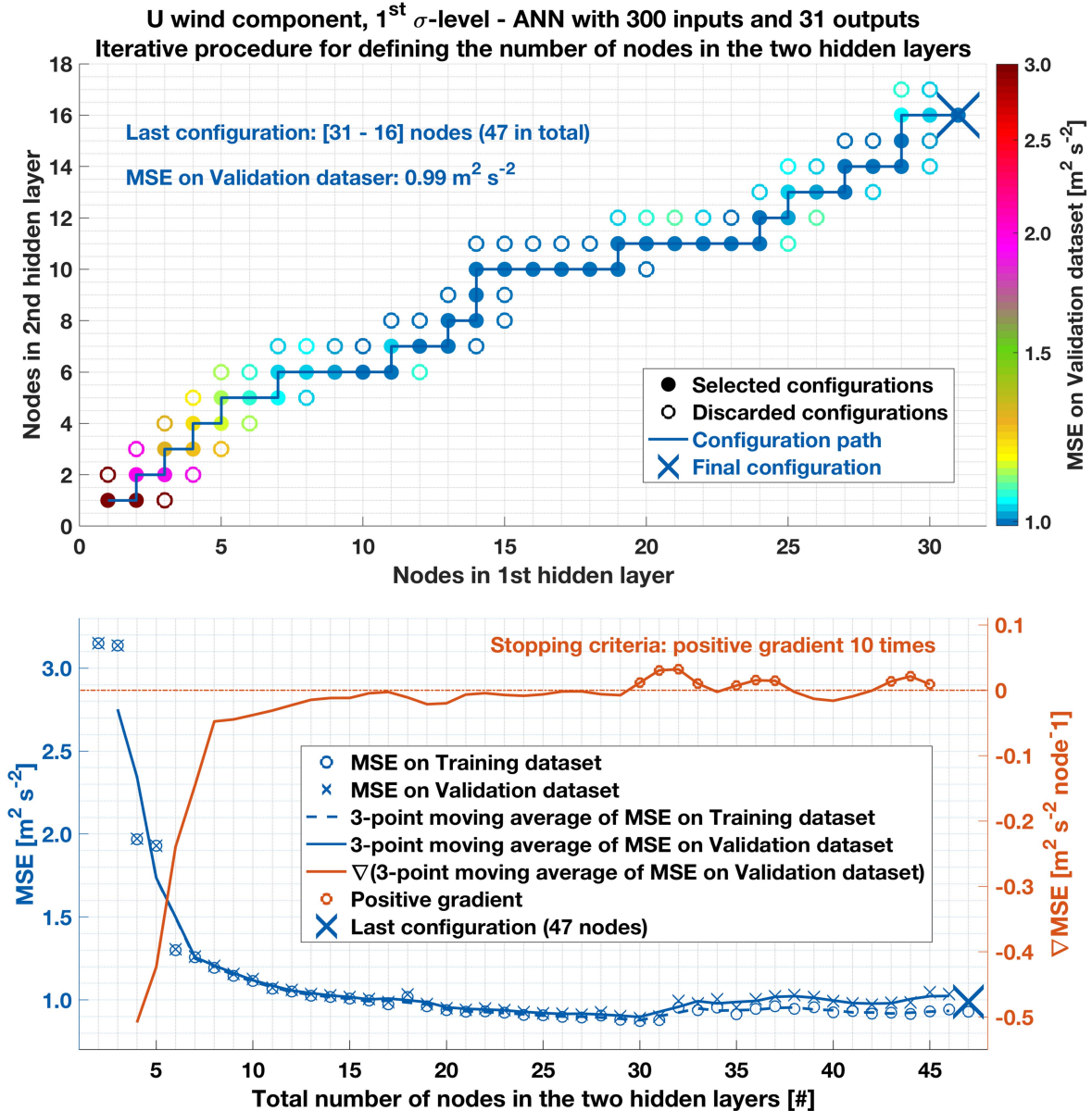
Fig. 9. Procedure for defining the number of nodes of the ANN, for the U wind component, first σ-level. Top: separate node growth on the two hidden layers. Circular filled markers represent the selected configurations, while the empty ones indicate the discarded configurations. The color represents the MSE calculated on the validation dataset. Bottom: trend of the MSE and its gradient as a function of the total number of nodes. The left y-axis in blue refers to the MSE, while the right y-axis in orange refers to the gradient of the MSE. The x-axis represents the total number of nodes on the two hidden layers.

performance. Fig. 9 exemplifies this procedure for the U wind component for the first σ-level, using the MSE calculated on the reconstructed values on the (7×7) box @240 m, in turn calculated with the inverse transformation of the PCA obtained from the ANN output. The iterative procedure ceased when the total number of nodes reached 47, with 31 and 16 in the first and second hidden layers, respectively. Although choosing the configuration corresponding to the minimum value of the MSE, around 30 total nodes, may seem plausible, the more complex ANN with the highest number of nodes was favored, risking a minor possibility of overfitting instead of underfitting. This is because in the following steps, some inputs will be eliminated, reducing the complexity of the ANNs and consequently the risk

of overfitting. Finally, the larger training dataset DB1Ms will be employed, further reducing the risk of overfitting.

For both U and V across all σ-levels, the total number of nodes configured for each ANN ranges from 39 to 51, with 20–33 nodes on the first hidden layer and 15–24 nodes on the second hidden layer.

D. ANNs Input Selection and Training

The input variables identified in Section IV-A and subsequently reduced through PCA were chosen due to their potential to contain valuable information for the training of ANNs. This choice stems from either a direct correlation with the outputs or
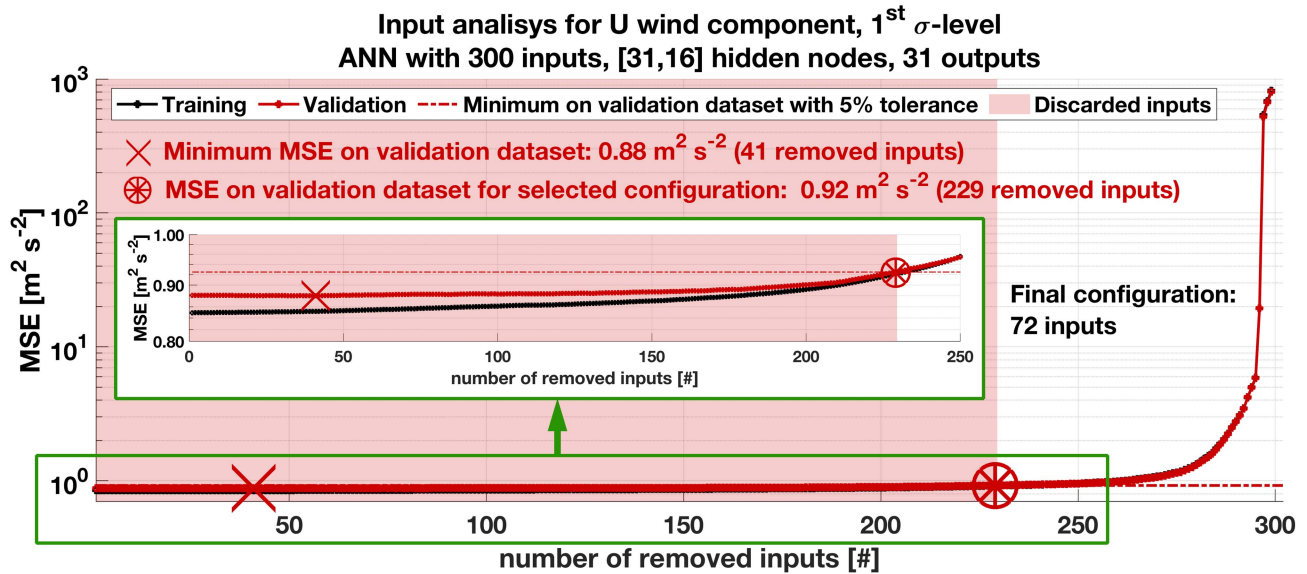
Fig. 10. Input removal procedure for the U wind component, first σ-level. The green box highlights the area around MSE $= 0.9 \text{ m}^2/\text{s}^2$, magnifying it. The removal of 229 out of the initial 300 inputs considered defines a final ANN configuration with 71 inputs.

their ability to characterize atmospheric conditions and surface characteristics. Nevertheless, some inputs may provide negligible or even counterproductive contributions to the ANNs, increasing both the computational costs of the final ANN training and the risk of overfitting. As a result, an iterative procedure was implemented to evaluate each input's contribution and, if necessary, eliminate it. This process initially requires a thoroughly trained ANN; hence, using the ANN defined and trained as described in Section IV-C. Its training was enhanced by conducting further training epochs using the Levenberg–Marquardt algorithm. Subsequently, in the first iteration, the significance of each input was evaluated by eliminating them one by one to identify the least important input—the one that, after its elimination and subsequent update of the ANN weights, resulted in the lowest MSE value calculated on the Validation dataset. Once the least significant input of the ANN was identified, it was permanently removed.

The ANN's weight update was considered definitive, and the iterative process continued with subsequent iterations, removing one input at a time until reaching the minimum MSE value on the Validation set within a 5% tolerance. Ideally, additional training epochs should be conducted to update the ANN weights at each iteration but this method would be computationally intensive and nearly impractical. To address this, the weight updates were performed using a procedure akin to the one developed by Castellano and Fanelli [90], as detailed in Appendix B. This procedure redistributed the weights of the removed input among the other weights of the remaining inputs using the conjugate gradient (CG) method [91], [92]. This redistribution aimed to maintain, as much as possible, the input values of each node of the first hidden layer, eliminating the need to retrain the network.

Fig. 10 summarizes, as an example, the ANN input removal procedure for the U wind component for the first σ-level. The MSE trend calculated on the Validation Dataset (red solid line

with a filled circle) as a function of the number of removed inputs initially remains almost constant and approximately equal to the minimum value of $0.88 \text{ m}^2/\text{s}^2$ obtained when 41 inputs were removed (red cross marker). After the removal of around 150 inputs, the MSE starts to increase by a few percentage points, reaching about $0.92 \text{ m}^2/\text{s}^2$, which corresponds to the chosen 5% threshold of the minimum value (red dashed line). Beyond this point (red wheel marker), corresponding to 229 removed inputs, the MSE increases more rapidly, and no further inputs are removed. In addition, the initial difference between the MSE calculated on the Validation dataset and that calculated on the Training dataset (black solid line with a filled circle), approximately $0.03 \text{ m}^2/\text{s}^2$, indicates a small initial overfitting. The input removal procedure has significantly reduced this overfitting, bringing this difference to about $0.004 \text{ m}^2/\text{s}^2$, confirming that reducing the number of inputs helps lower the risk of overfitting.

Once the negligible inputs were removed, the ANNs weights and biases were updated to their final versions. Additional training epochs were performed using the Levenberg–Marquardt training algorithm applied to the DB1M datasets described in Section IV-B. Fig. 11 illustrates a flowchart of the process of developing and using the WiFiRE algorithm.

V. SPATIAL RESOLUTION ANALYSIS

Spatial resolution can be described as *"the size of the smallest distinguishable feature"* [93]. It is measured in units of length (e.g., kilometer) and can theoretically be determined as the inverse of the maximum spatial frequency specifically related to the signal, which is expressed in units of inverse length (e.g., km^{-1}). When an image is sampled at constant ΔS intervals in both directions, the Nyquist limit (N_L) dictates that the highest spatial frequency present in the image is $N_L = 2\Delta S^{-1}$.
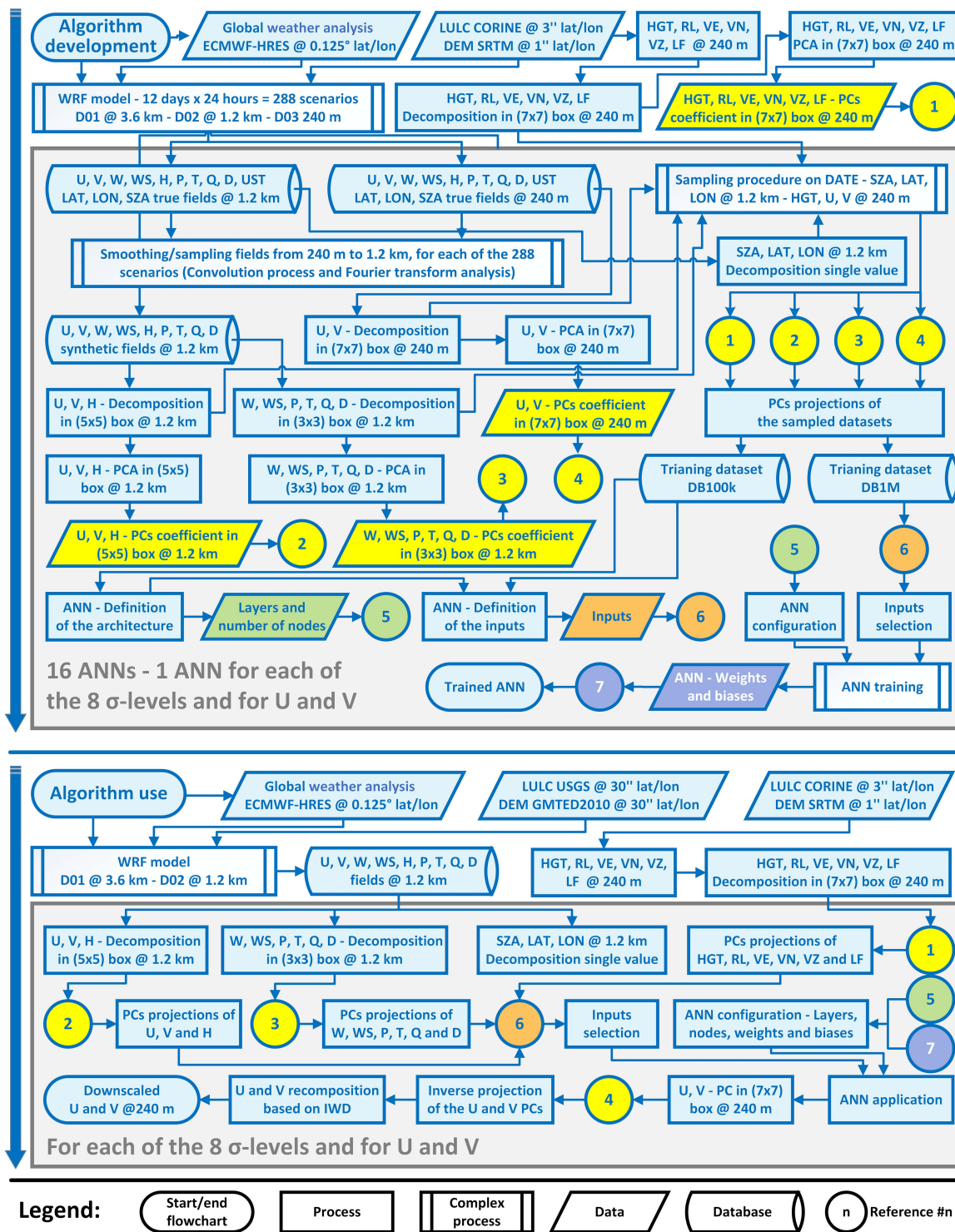
Algorithm development

Global weather analysis ECMWF-HRES @ 0.125° lat/lon

LULC CORINE @ 3'' lat/lon DEM SRTM @ 1'' lat/lon

HGT, RL, VE, VN, VZ, LF @ 240 m

HGT, RL, VE, VN, VZ, LF PCA in (7x7) box @ 240 m

WRF model - 12 days x 24 hours = 288 scenarios D01 @ 3.6 km - D02 @ 1.2 km - D03 240 m

HGT, RL, VE, VN, VZ, LF Decomposition in (7x7) box @ 240 m

HGT, RL, VE, VN, VZ, LF - PCs coefficient in (7x7) box @ 240 m   (1)

U, V, W, WS, H, P, T, Q, D, UST LAT, LON, SZA true fields @ 1.2 km

U, V, W, WS, H, P, T, Q, D, UST LAT, LON, SZA true fields @ 240 m

Sampling procedure on DATE - SZA, LAT, LON @ 1.2 km - HGT, U, V @ 240 m

Smoothing/sampling fields from 240 m to 1.2 km, for each of the 288 scenarios (Convolution process and Fourier transform analysis)

SZA, LAT, LON @ 1.2 km Decomposition single value

U, V, W, WS, H, P, T, Q, D synthetic fields @ 1.2 km

U, V - Decomposition in (7x7) box @ 240 m

U, V - PCA in (7x7) box @ 240 m

(1) (2) (3) (4)

U, V, H - Decomposition in (5x5) box @ 1.2 km

W, WS, P, T, Q, D - Decomposition in (3x3) box @ 1.2 km

U, V - PCs coefficient in (7x7) box @ 240 m

PCs projections of the sampled datasets

U, V, H - PCA in (5x5) box @ 1.2 km

W, WS, P, T, Q, D - PCA in (3x3) box @ 1.2 km

(3) (4)

Trianing dataset DB100k

Trianing dataset DB1M

U, V, H - PCs coefficient in (5x5) box @ 1.2 km   (2)

W, WS, P, T, Q, D - PCs coefficient in (3x3) box @ 1.2 km

(5) (6)

ANN - Definition of the architecture

Layers and number of nodes   (5)

ANN - Definition of the inputs

Inputs   (6)

ANN configuration

Inputs selection

16 ANNs - 1 ANN for each of the 8 σ-levels and for U and V

Trained ANN   (7)

ANN - Weights and biases

ANN training

Algorithm use

Global weather analysis ECMWF-HRES @ 0.125° lat/lon

LULC USGS @ 30'' lat/lon DEM GMTED2010 @ 30'' lat/lon

LULC CORINE @ 3'' lat/lon DEM SRTM @ 1'' lat/lon

WRF model D01 @ 3.6 km - D02 @ 1.2 km

U, V, W, WS, H, P, T, Q, D fields @ 1.2 km

HGT, RL, VE, VN, VZ, LF @ 240 m

HGT, RL, VE, VN, VZ, LF Decomposition in (7x7) box @ 240 m

U, V, H - Decomposition in (5x5) box @ 1.2 km

W, WS, P, T, Q, D - Decomposition in (3x3) box @ 1.2 km

SZA, LAT, LON @ 1.2 km Decomposition single value

PCs projections of HGT, RL, VE, VN, VZ and LF   (1)

(5)

(2) PCs projections of U, V and H

(3) PCs projections of W, WS, P, T, Q and D

(6) Inputs selection

ANN configuration - Layers, nodes, weights and biases   (7)

Downscaled U and V @240 m

U and V recomposition based on IWD

Inverse projection of the U and V PCs

(4) U, V - PC in (7x7) box @ 240 m

ANN application

For each of the 8 σ-levels and for U and V

Legend: Start/end flowchart   Process   Complex process   Data   Database   (n) Reference #n

Fig. 11.   WiFiRE algorithm flowchart: development (top) and use (bottom).

Consequently, the maximum theoretical spatial resolution is $2\Delta S$. This leads to one of the common definitions of spatial resolution, defined as *"a measure of how close to each other two objects can be located such that they can be distinguished"* [94]. However, determining the spatial frequency, and thereby the spatial resolution, lacks a universal method. This complexity arises as the highest frequencies may correspond to noise rather than the actual information content of the image, and the Fourier transformation can include all frequencies from zero to N_L seamlessly.

To address this challenge, an analogy can be drawn from real-world observations using radiometers or lenses, where spatial

resolution can be inferred from the FWHM of the point spread function (PSF). The PSF acts as a low-pass filter, cutting off higher frequencies beyond its width, allowing the spatial resolution of an image to be gauged by the instrument's "*capacity to resolve high spatial frequencies*" [95]. Assuming a Gaussian-shaped PSF (2), the approach proposed by Mizutani et al. [96] can be used. This method involves plotting the logarithm of the average squared amplitudes of the DFT (A^2) against the square of the spatial frequency distance from the origin (d^2) for each 5 × 5 pixel block. The standard deviation σ_g of the Gaussian PSF is determined from the slope φ of the linear regression applied to the data points on the left side of the distribution

$$\sigma_g = \frac{\sqrt{\varphi}}{2\pi}. \tag{24}$$

From σ_g, the FWHM of the PSF (3) can also be computed, serving as an estimate of the spatial resolution of the whole image. However, Mizutani et al.'s [96] approach requires manually selecting a threshold value d_{thr}^2 on the d^2-axis to determine the subset of points within the range $[0 - d_{\mathrm{thr}}^2]$ for linear regression. To avoid manual selection, an iterative procedure was adopted, initially considering the 5% of points nearest the d^2-axis origin and gradually expanding the interval for linear regression with 1% increments toward higher d^2 values. Each iteration calculates a new linear regression and its Pearson correlation coefficient (PCC), with d_{thr}^2 chosen at the peak PCC value. The application of this method to the wind fields examined in this study lacks rigor, as it relies on analogy with observed data. However, employing a PSF with circular symmetry, which is inherently general, provides a rough estimation facilitating the comparison of spatial resolutions across various wind fields.

Since high spatial frequency signals may be related to noise rather than to actual high-frequency information content, assessing noise becomes essential, especially as spatial resolution enhancement methods can sometimes introduce random noise artifacts [97], [98], [99]. Consequently, the method proposed by Immerkaer [100], which assumes additive noise with zero mean, was adopted. This method uses a spatial filter L obtained from the differences between two Laplacian kernels $L1$ and $L2$

$$L1 = \begin{vmatrix} 0 & 1 & 0 \\ 1 & -4 & 1 \\ 0 & 1 & 0 \end{vmatrix} \quad L2 = \begin{vmatrix} 1 & 0 & 1 \\ 0 & -4 & 0 \\ 1 & 0 & 1 \end{vmatrix} \tag{25}$$

$$L = L2 - 2\,L1 = \begin{vmatrix} 1 & -2 & 1 \\ -2 & 4 & -2 \\ 1 & -2 & 1 \end{vmatrix}. \tag{26}$$

Applying the spatial filter L to an image strips off structural features, such as edges or textures, enabling noise estimation as the standard deviation σ_n of the filtered image

$$\sigma_n = \sqrt{\frac{\pi}{2}}\,\frac{1}{6\,(W - 2)\,(H - 2)}\sum |I * L| \tag{27}$$

where W and H represent the image dimensions, I represents the image, $|\cdot|$ denotes the absolute value, $*$ is the convolution operator, and the summation is performed on all the elements of the convolution product.
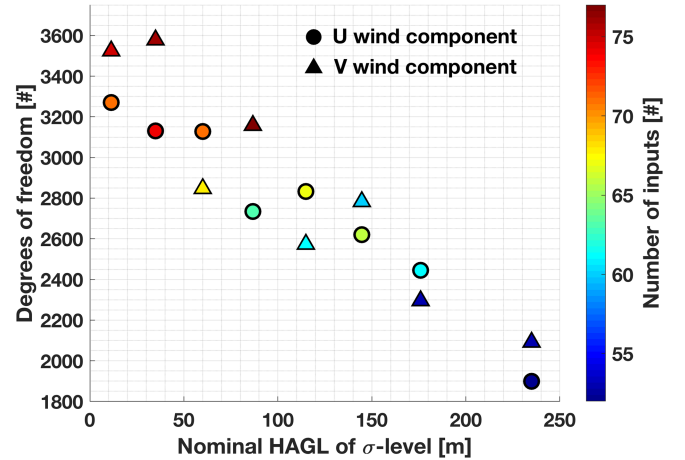

Fig. 12. Number of DoFs and inputs of the ANNs for the different σ-levels.

VI. Results

Fig. 12 displays the number of inputs, varying from 52 to 77, and the degrees of freedom (DoFs)—i.e., the total number of weights and biases—for U and V across the different σ-levels. Both the number of inputs and DoF, which vary from 52 to 75 and approximately 1800 to 3600 respectively, show a decreasing trend with increasing σ-levels. Fig. 13 provides a summary of the number of inputs and outputs used for the ANNs of the different σ-levels. As expected, among the dynamic inputs made up of the 1.2 km WRF outputs, the most crucial variable for downscaling the wind component U (V) is the same wind component U (V) at 1.2 km with an average of 18 (19) PCs. This is followed by the other horizontal wind component V (U) with 7 (6) PCs, wind speed WS with 6 (5) PCs, vertical wind component W with 6 (5) PCs, and friction velocity U^* with 5 (5) PCs, all of similar importance. Pressure P, humidity Q, and density D contribute on average with 1 PC, while temperature (T) is somewhat more significant, contributing on average with 3 (2) PCs. Among the 240 m static variables, the surface altitude HGT is the most important, with about 8 (8) PCs, followed by the VE (VN) component of the normal versor to the earth's surface, parallel to the wind component U (V) with 4 (5) PCs, and the upward-directed component VZ with 2 (3) PCs. The remaining input variables are almost negligible or absent. Of the 49 output PCs, an average of 26 PCs was considered for both U and V.

This study focuses primarily on providing a detailed examination of the WiFiRE algorithm and assessing its effectiveness in downscaling wind speed as simulated by the WRF model. The study does not aim to analyze the reliability of these simulations. Consequently, the algorithm's performance was not assessed by comparing the downscaled field with measured data using anemometers or wind profilers. Such a comparison would inherently depend on the performance of the WRF model, which is influenced by a wide range of physical options, parameters, and configurations. The resulting assessment would, therefore, be related to the WRF model, not the WiFiRE algorithm. To evaluate the algorithm's performance, its outputs were compared
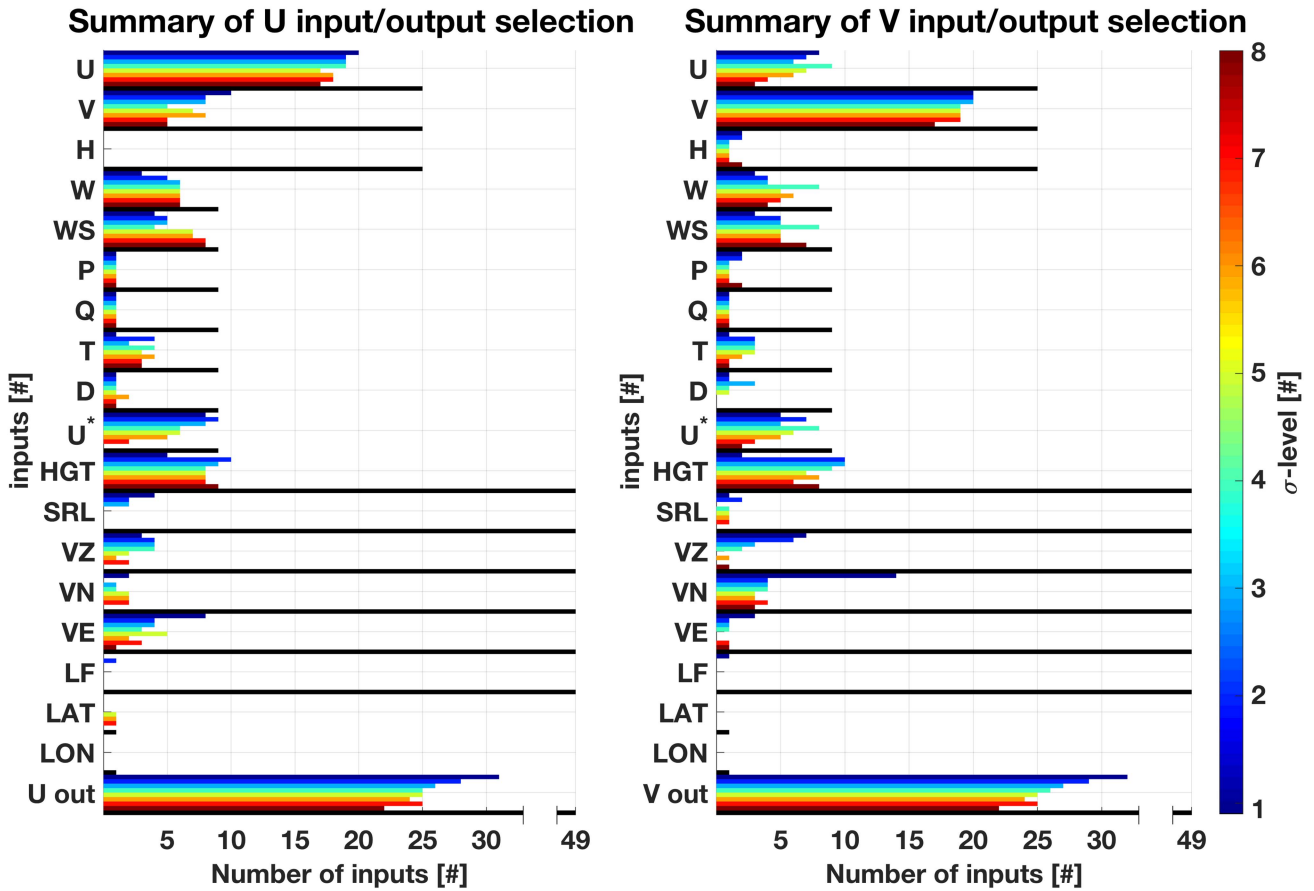
Fig. 13. Summary of the number of inputs and outputs of the different ANNs. Each color represents the inputs/outputs selected for a specific σ-level, while the black line under each group of variables indicates the total number of inputs/outputs initially considered.

to those from the WRF-LES model using an independent dataset. This dataset was also generated using the WRF-LES, using the same settings and configurations outlined in Section III-B. It comprises 24-h simulated scenarios for four specific dates in 2017: 15-03-2017, 10-06-2017, 23-09-2017, and 25-12-2017, one for each season, resulting in approximately 10^7 patterns for each of the eight σ-levels (hereinafter *Evaluation dataset*).

Since the WiFiRE algorithm operates similarly to bidimensional spatial interpolations—i.e., bringing from a coarser regular grid (1.2 km) to a finer one (240 m)—the algorithm's performance was evaluated against two common interpolation methods, Linear and Spline interpolation.

Due to the subtle variations in the structure of the WRF fields between the D02 and D03 domains, as discussed in Section III-A, two distinct evaluations were conducted. The initial assessment involved a point-by-point analysis, where the WiFiRE algorithm was applied to synthetic fields at a 1.2 km resolution. These downscaled fields were then compared with the WRF-LES fields at a 240 m resolution to assess the algorithm's capability in reconstructing field structures. The second evaluation applied the WiFiRE algorithm to the true fields at a 1.2 km resolution and involved comparing the DFT amplitudes of the downscaled fields with those of the WRF-LES fields at 240 m. While the DFT amplitude analysis loses details on the

field's structure, it effectively maintains information regarding spatial resolution. This approach enables a comparison of the spatial resolutions of the fields, despite minor structural differences between them.

A. Assessment of the Structures of the Downscaled Fields

Fig. 14 shows the average vertical profiles of U, V, and WS, separately for land and sea surfaces, corresponding to the nominal HAGL of the eight σ-levels. The WiFiRE algorithm's output is compared to the WRF-LES output—used as reference data—and to the downscaled values computed using the two interpolation methods. Overall, all the profiles follow a trend qualitatively similar to the logarithmic wind profile law [101]. In general, all profiles exhibit a trend that qualitatively aligns with the logarithmic wind profile law [101]. A comparative analysis indicates that the vertical profiles generated by the WiFiRE algorithm bear a closer resemblance to those from the WRF model than those produced by the two interpolation methods. On land, the deviations between the WiFiRE algorithm and the interpolation methods average around 0.1 m/s for U and V, and 0.3 m/s for WS across all vertical levels. Over the sea, the mean discrepancies across all levels are nearly negligible, less than 0.1 m/s for U, V, and WS. However, for U and
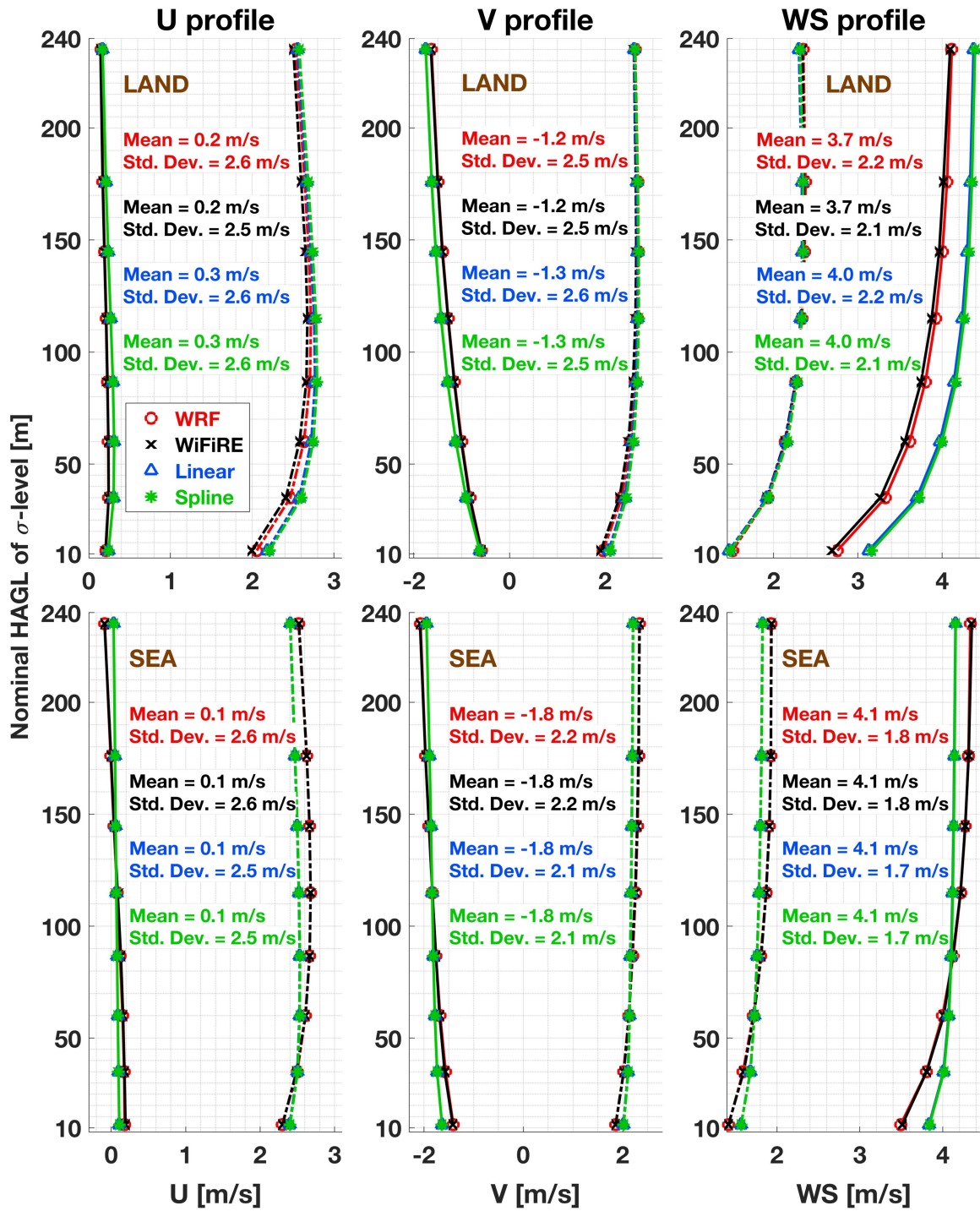
Fig. 14. Mean values (solid lines) and standard deviations (dashed lines) of the U, V, and WS across different σ-levels and separately for land and sea surface.

V, the interpolation methods tend to underestimate the WRF model at lower altitudes and overestimate it at higher ones. In contrast, for WS, the pattern is reversed, with underestimation occurring below approximately 80 m HAGL and overestimation above. The WiFiRE algorithm, however, produces profiles that are closely aligned with those from the WRF model. Fig. 14 also presents the average standard deviations for U, V, and WS. To compute the average standard deviation, individual

standard deviations were calculated for each of the 96 hourly scenarios (spanning 24 h across 4 days), both on land and sea, and then averaged. Subsequently, the average of these standard deviations across the vertical levels was computed as the mean of the average standard deviations (hereafter referred to simply as the standard deviation) for the eight σ-levels. Even in terms of standard deviations, the vertical profiles from the WiFiRE algorithm more closely mirror those from the WRF model than

do those from the interpolation methods. The most accurate results are observed over the sea, where the WiFiRE algorithm's profiles nearly perfectly match those from the WRF model, while the interpolation methods underestimate U, V, and WS by approximately 0.1 m/s. To enhance the assessment of the algorithm's effectiveness, three key metrics were utilized: mean bias difference (MBD), RMSD, and PCC

$$\text{MBD} = \frac{1}{N} \sum_{i=1}^{N} Y_{D,i} - Y_{W,i} \tag{28}$$

$$\text{RMSD} = \sqrt{\frac{1}{N} \sum_{i=1}^{N} \left(Y_{D,i} - Y_{W,i} \right)^2} \tag{29}$$

$$\text{PCC} = \frac{\sum_{i=1}^{N} \left(Y_{D,j} - \overline{Y_{D,i}} \right) \left(Y_{W,i} - \overline{Y_{W,i}} \right)}{\sqrt{\sum_{i=1}^{N} \left(Y_{D,i} - \overline{Y_{D,i}} \right)^2} \sqrt{\sum_{i=1}^{N} \left(Y_{W,i} - \overline{Y_{W,i}} \right)^2}} \tag{30}$$

where N is the number of samples, $Y_{D,i}$ are the wind values (U, V, or WS) downscaled by the WiFiRE algorithm or by the two proposed interpolation methods, $Y_{W,i}$ are the wind values of the WRF model, and the notation $\bar{X}$ indicates the mean value of X.

The MBD should ideally be minimal in absolute terms and close to zero. It is deemed acceptable if it is at least an order of magnitude smaller than the mean value calculated from the WRF model, which serves as the benchmark. Similarly, the RMSD should be as low as possible, ideally nearing zero. A maximum acceptable limit for RMSD is the standard deviation of the reference variable. Values exceeding this threshold suggest that the downscaling process's accuracy is inferior to simply using the mean value of the WRF model's field as the downscaled field. The PCC ranges from -1 to 1. Higher values indicate a stronger correlation between the downscaled fields and the WRF model fields. A PCC value above approximately 0.3 is considered moderately acceptable. However, for the algorithm to be deemed successful, it must not only meet these thresholds but also surpass the corresponding metrics achieved by the two interpolation methods.

Fig. 15 illustrates that the MBDs are consistently at least an order of magnitude smaller than the mean values depicted in Fig. 14. The MBE calculated with WiFiRE are almost always negligible, with absolute values ranging from 10^{-2} to 10^{-3}, both on land and sea, and separately or averaged over all vertical levels. In contrast, the two interpolation methods exhibit larger MBDs in absolute values. Over land, their mean values reach about 0.3 m/s for WS. Over the sea, while mean values are generally negligible, they peak at 0.4 m/s at lower levels and -0.2 m/s at higher levels. Fig. 15 also shows the average RMSD, calculated as the mean of the RMSDs for each scenario and level. All values are less than those of the corresponding standard deviations of the WRF model, which is used as the threshold. Notably, the WiFiRE algorithm achieves the most favorable outcomes, with an average RMSD of approximately 0.5 m/s over land for U, V, and WS, in stark contrast to the 1.6–1.7 m/s RMSD obtained with the two interpolation methods. Over the sea, the WiFiRE algorithm continues to improve recording an

RMSD of 0.2 m/s compared to the 1.0–1.2 m/s RMSD associated with the interpolation methods. Fig. 16 compares the three downscaling methods in terms of the average PCC, calculated as the mean of the PCCs for each scenario and level. All PCC values exceed 0.6, marking them as acceptable. However, the WiFiRE algorithm surpasses the interpolation methods here as well, with PCC values approximately between 0.96 and 0.98 on land and 0.99 and 1.00 on sea, compared to the 0.71–0.79 and 0.82–0.89 ranges, respectively, for the interpolations. Figs. 17–22 show a binned analysis performed separately for each σ-level for WS, a critical variable for wind power generation. This analysis segments the WS data from the WRF model into 1 m/s bins, ranging up to 15 m/s over land and 12 m/s over the sea. Fig. 17 shows the trend of MBD over land for the WiFiRE algorithm, showing values close to zero for low WS values and a decrease to a minimum of -1.5 m/s for higher WS values. Conversely, the interpolation methods exhibit larger MBD absolute values, starting around 1.5 m/s for low WS values and escalating to over -4 m/s at WS values around 15 m/s. These trends are more pronounced at lower σ-levels and diminish at higher levels. On average, the WiFiRE algorithm's MBD ranges from -0.5 to -0.1 m/s, whereas the interpolation methods range from -0.3 to -1.3 m/s. Fig. 18 depicts the MBD trend over the sea, with dynamics similar to those over land but with less pronounced variations. At lower σ-levels, the WiFiRE algorithm's MBD varies between approximately 0 and -0.5 m/s, while the interpolations range from about 1 to -2 m/s. Averaging across all σ-levels, the WiFiRE algorithm's MBD lies between -0.2 and -0.01 m/s, while for the interpolation methods, it varies between -0.2 and -0.4 m/s.

Fig. 19 presents the RMSD analysis over land. For the first σ-level, it reveals that the WiFiRE algorithm's RMSD starts at approximately 0.5 m/s for low WS values and ascends to around 1 m/s for higher WS values. The RMSD for the interpolation methods begins at roughly 2 m/s for low WS values, dips to a minimum of 1.2 m/s for WS in the 3–5 m/s range, and then climbs to over 4 m/s at higher WS values. In the other vertical levels, the trends are similar; more marked at lower σ-levels and become less pronounced with increasing σ-levels. Across all σ-levels, the WiFiRE algorithm's RMSD ranges from 0.6 to 0.9 m/s, whereas the interpolations show an RMSD between 1.9 and 2.3 m/s. Similar to the land analysis, Fig. 20 shows that the sea RMSD trends for the WiFiRE algorithm are less distinct, with the maximum increase in WS causing a variation of about 0.2–0.6 m/s, while for the interpolations, it is approximately 1–2 m/s. The averages across all WS and σ-levels range from 0.2 to 0.4 m/s for the WiFiRE algorithm and from 1.2 to 1.6 m/s for the interpolations.

Fig. 21 analyzes the PCC on land, indicating that the WiFiRE algorithm consistently outperforms the interpolation methods, achieving PCCs higher than those obtained through the two interpolations. Typically, the WiFiRE algorithm's PCC starts at around 0.3 for low WS values and quickly rises to about 0.5 for WS values around 2–3 m/s, then either decreases with increasing WS at lower σ-levels or remains steady at higher σ-levels. The interpolations exhibit a similar trend but with lower PCC values around 0.2–0.3. Over the sea, as depicted in Fig. 22,
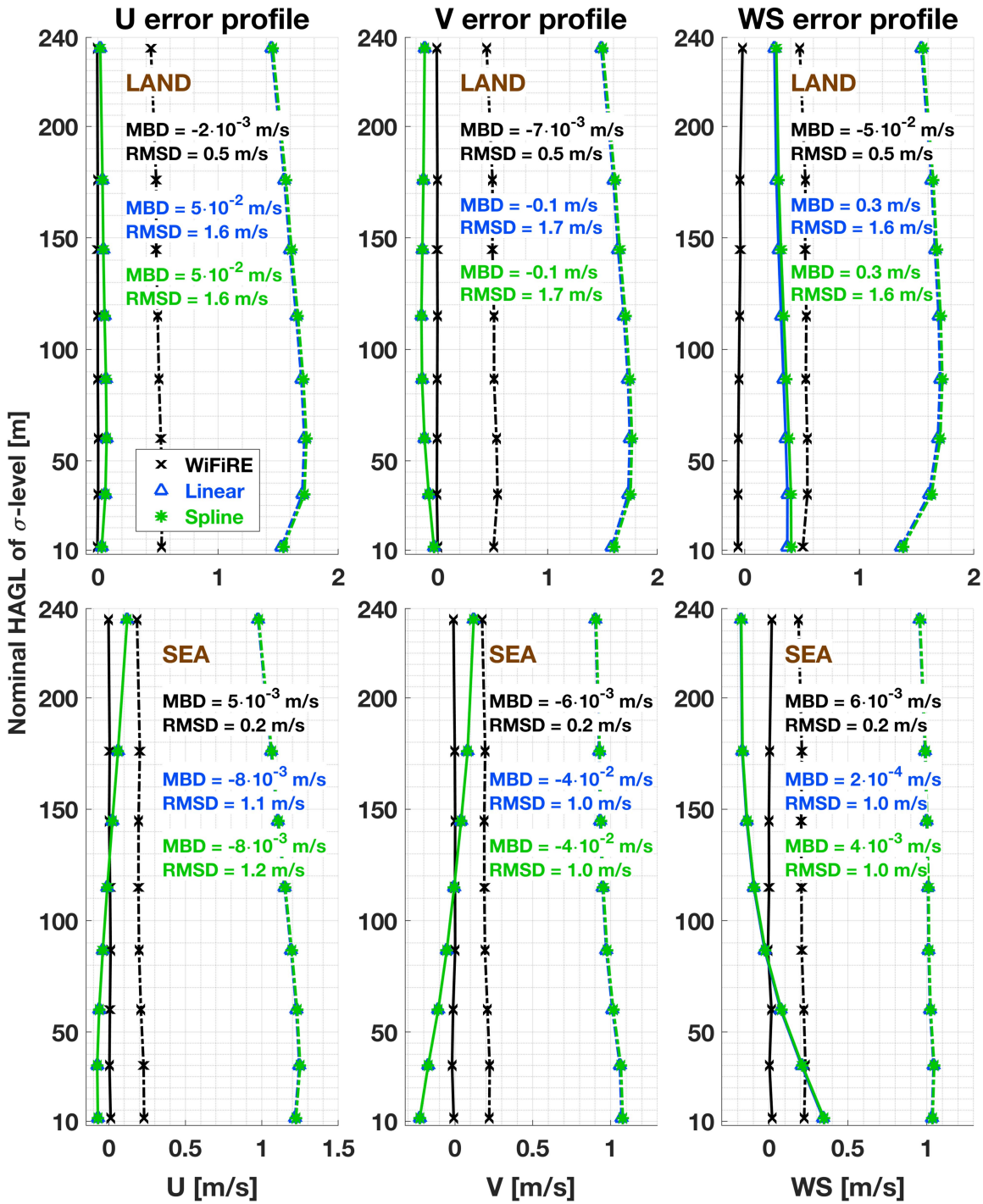
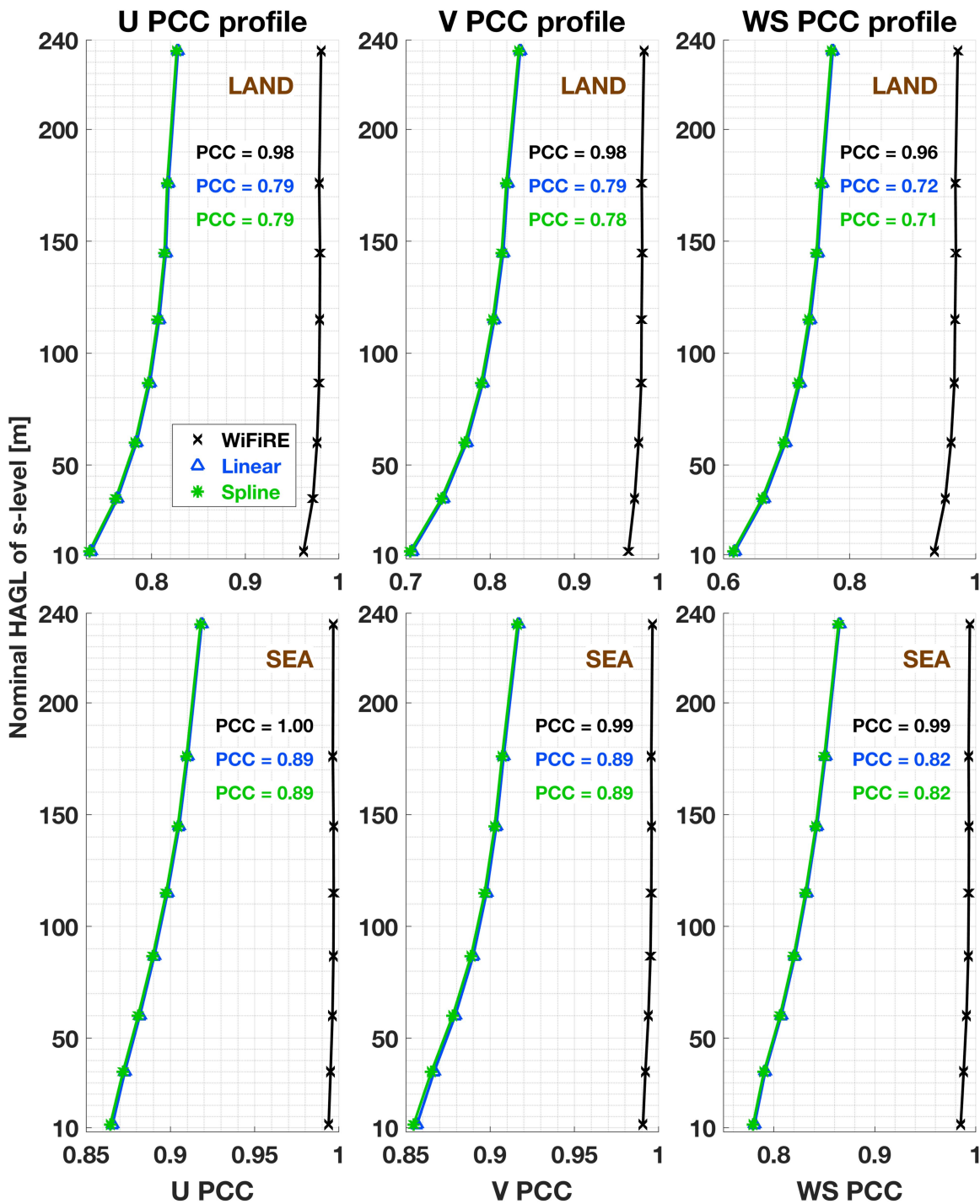Fig. 15. Comparative analysis of the MBDs (solid lines) and RMSDs (dashed lines) among the outputs generated by the WiFiRE algorithm and those calculated by the two proposed interpolation methods across different σ-levels and separately for land and sea surface.

the trend is qualitatively similar but with higher PCC values. The average PCC across all WS for the WiFiRE algorithm ranges from 0.64 to 0.77, whereas for the interpolations, it spans from 0.17 to 0.23. The lower PCC values observed in Figs. 21 and 22, compared to those shown in Fig. 15, result from the binned analysis. By restricting the analysis to WS values of the WRF at 0.1 m/s intervals, the numerator in the PCC equation decreases more than the denominator, leading to lower PCC values.

Fig. 23 displays the linear regression of WS across all vertical levels, comparing the outcomes of the three downscaling methods with the reference values from the WRF model. The WiFiRE method demonstrates a more concentrated distribution of data
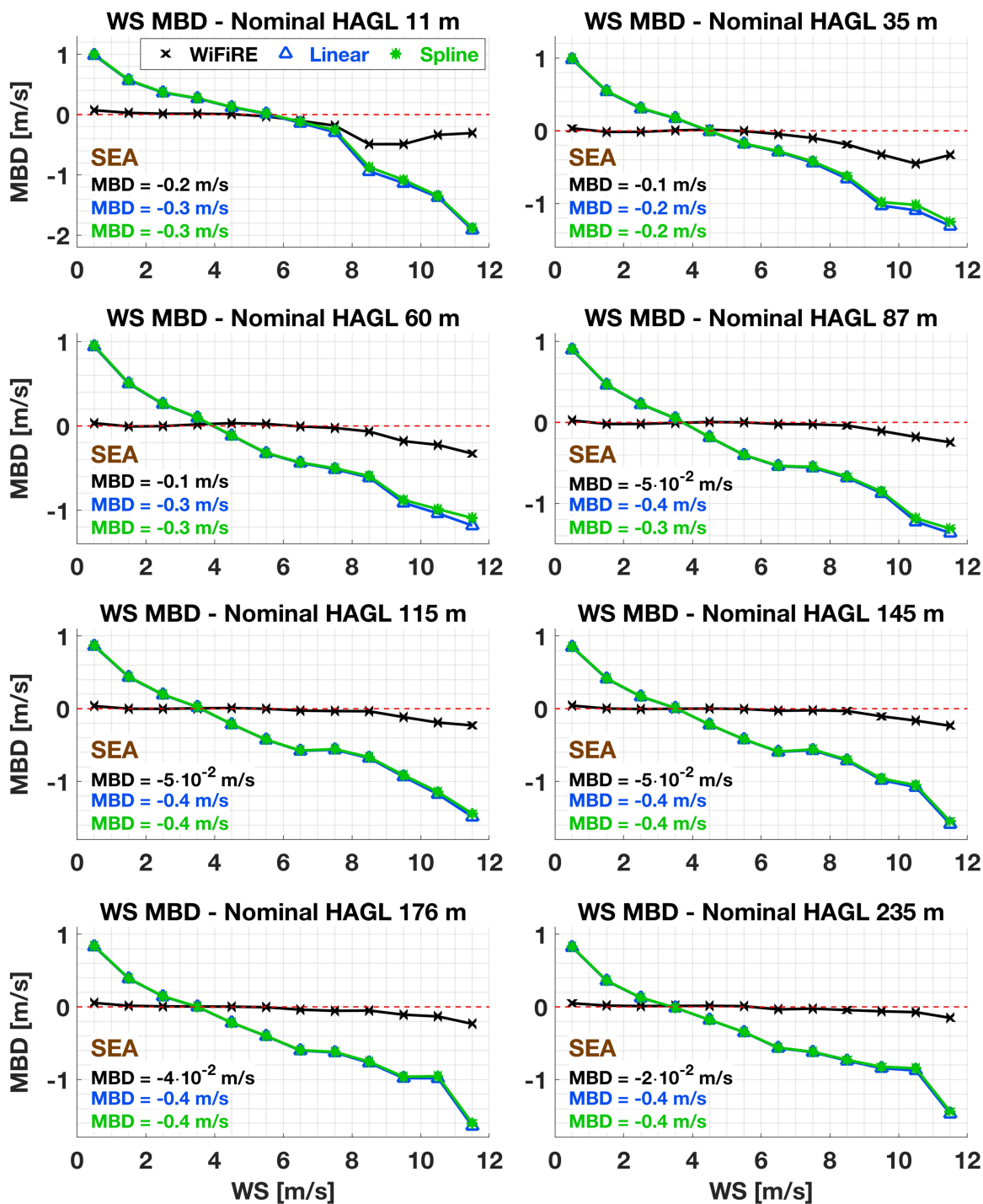
Fig. 16.   Comparative analysis of the PCCs among the outputs generated by the WiFiRE algorithm and those calculated by the two proposed interpolation methods across different σ-levels and separately for land and sea surface.

points around the diagonal bisector of the plot, indicating less scatter compared to the interpolation methods. This observation is supported by the coefficient of determination (R^2), which stands at 0.96 for the WiFiRE algorithm, significantly higher than the 0.68–0.69 range for the interpolation methods over land, and 0.99 for WiFiRE versus 0.84 for the interpolations over the sea. Fig. 24's WS density plot further illustrates these

trends. Over land, the distribution curves of the WRF model and the WiFiRE algorithm are closely aligned, as evidenced by their similar skewness values of 1.06 and 1.05, respectively. In contrast, the distributions from the interpolation methods are shifted toward higher WS values and exhibit a broader spread, with both methods showing a skewness of 1.00. Over the sea, the distribution curves for the model and the WiFiRE algorithm
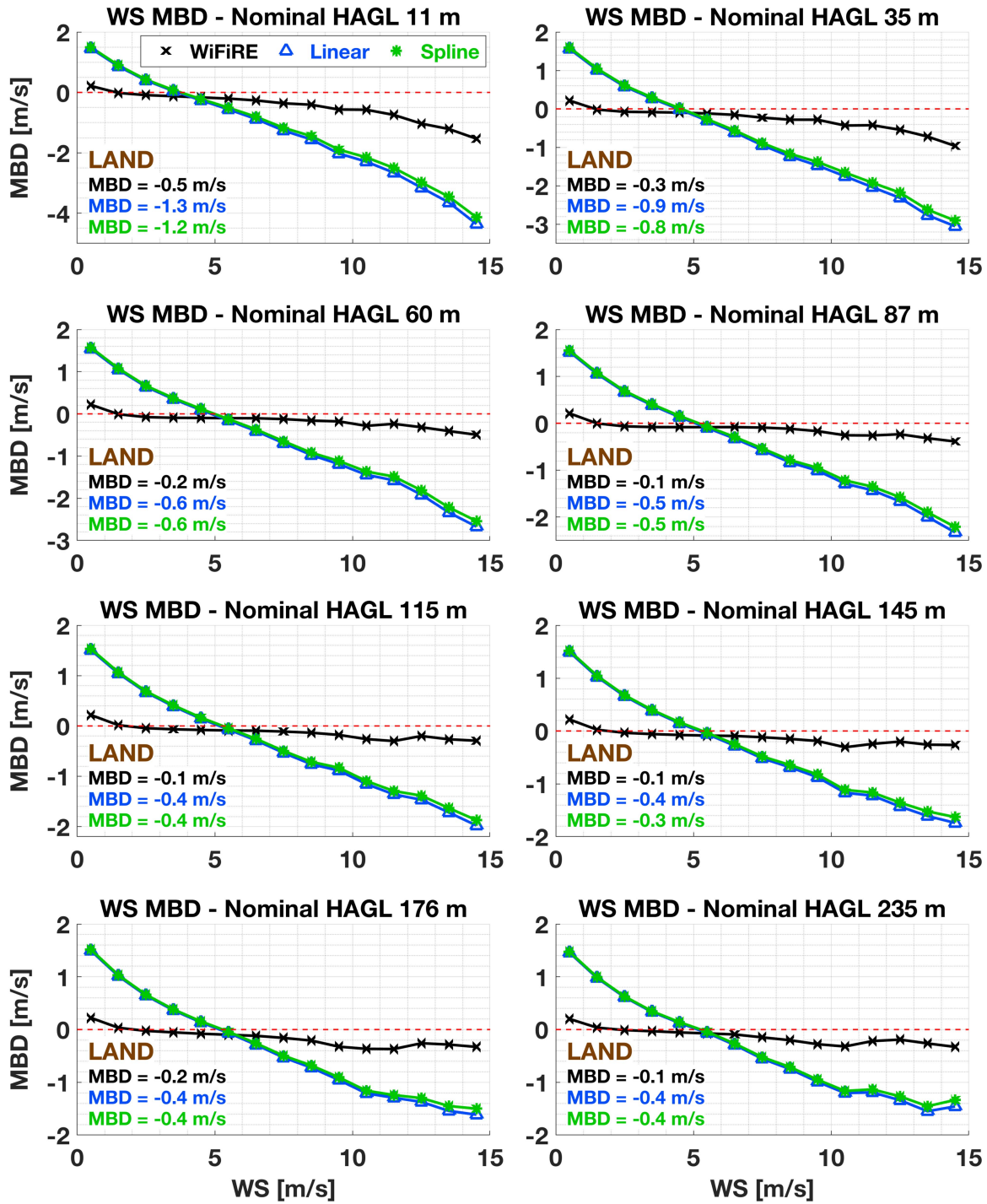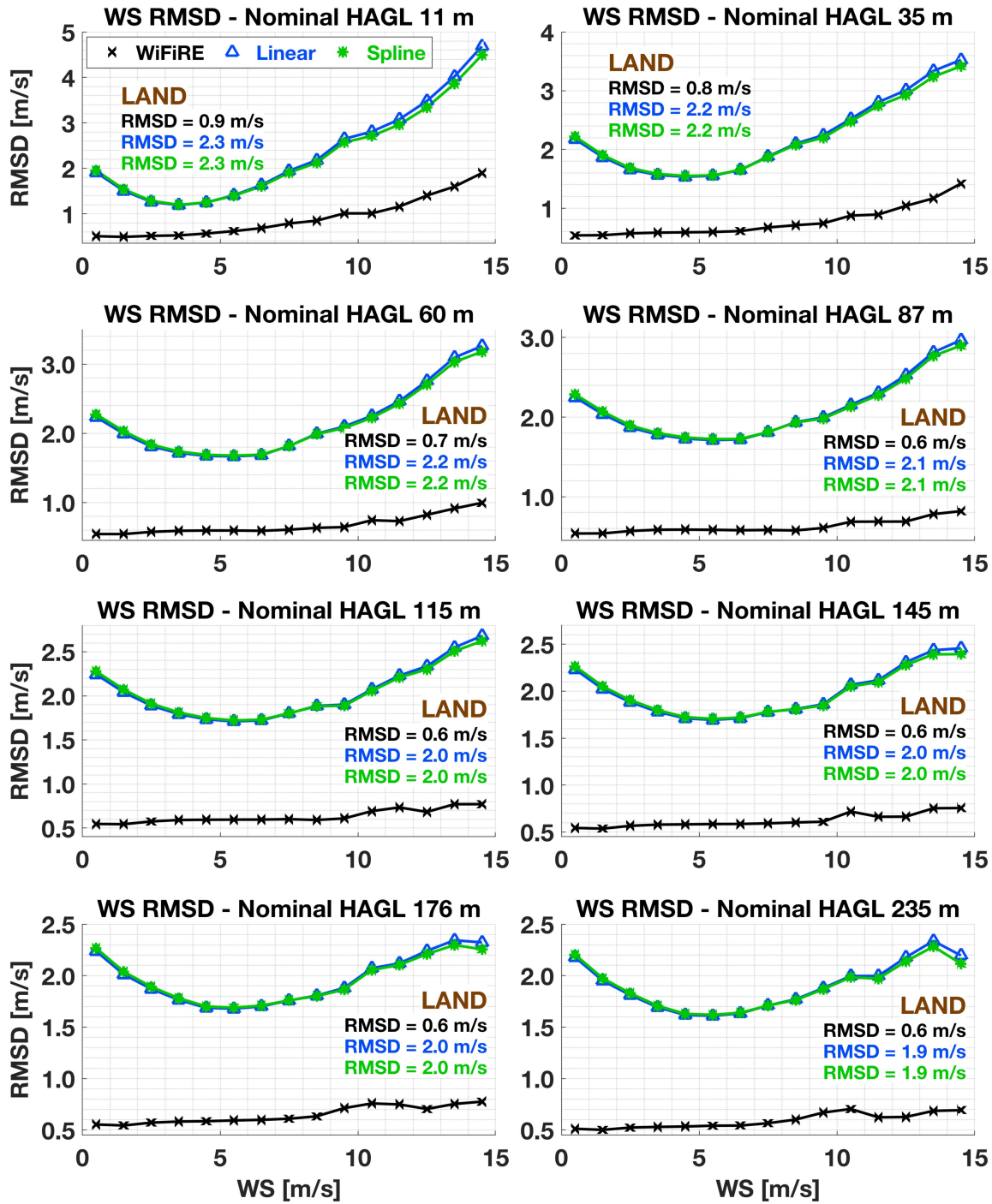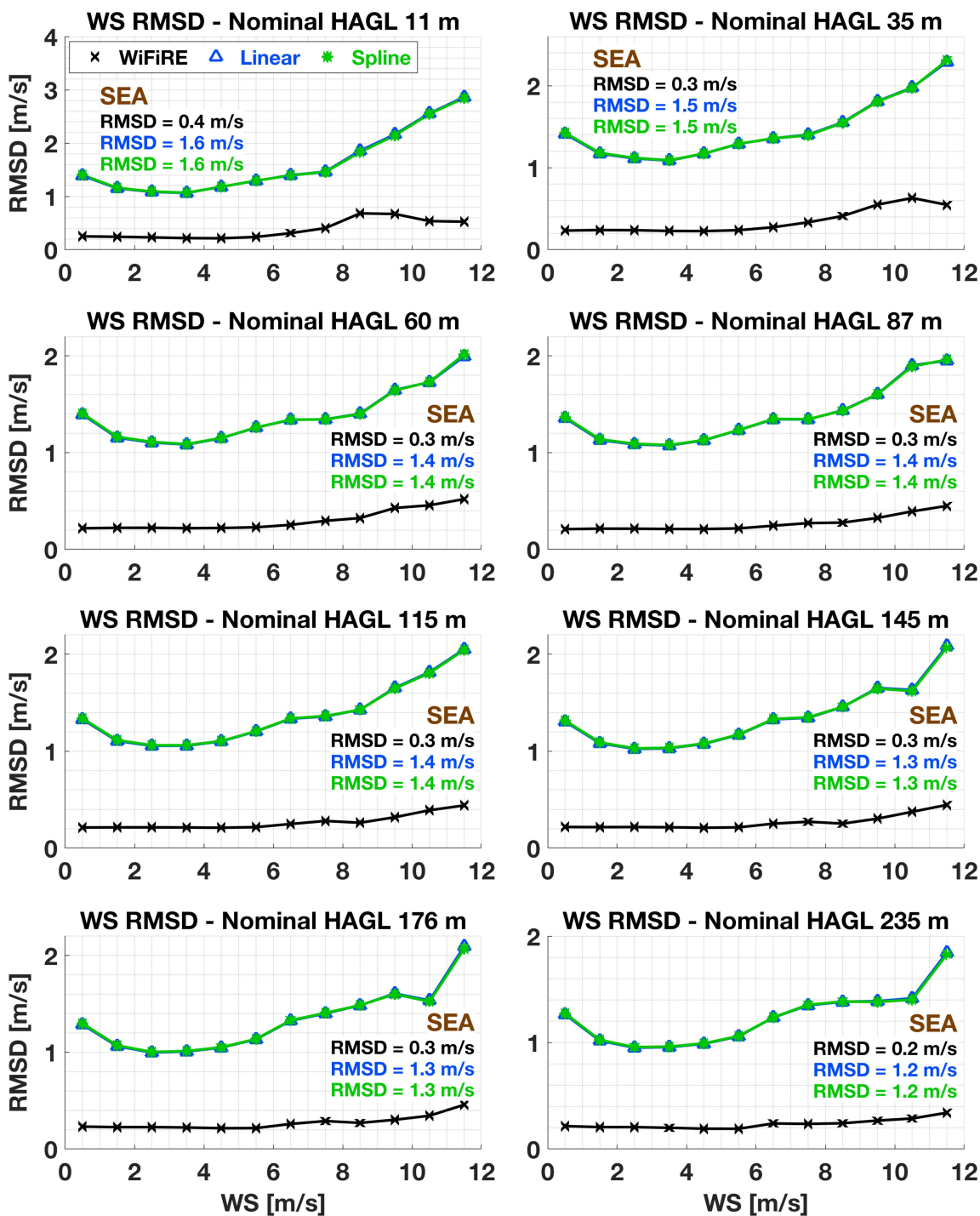
Fig. 17. Comparative binned analysis of the MBD for WS among the outputs generated by the WiFiRE algorithm and those calculated by the two proposed interpolation methods across different σ-levels over land surface.

also closely resemble each other, whereas the curves for the interpolations are slightly shifted toward lower WS values. In terms of skewness, the WRF model and the WiFiRE algorithm show more comparable values of 0.92 and 0.90, respectively, as opposed to 0.86 for the interpolations.

Fig. 25 shows an example of WS downscaling for the third σ-level on March 15, 2017, at 06:00 UTC.

B. Evaluation of the Spatial Resolution of the Downscaled Fields

Fig. 26 illustrates the DFT log-amplitudes of WS, providing a comparison among the WRF output at 240 m, the results obtained from the Spline interpolation, and those from the WiFiRE algorithm. The intensities of the DFT log-amplitudes and the rate

Fig. 18. Comparative binned analysis of the MBD for WS among the outputs generated by the WiFiRE algorithm and those calculated by the two proposed interpolation methods across different σ-levels over sea surface.

at which they decline from the center outward represent spatial resolution, with a faster drop and lower intensity indicating lower resolution. At the center of the DFT log-amplitude, denoted by coordinates $(0, 0)$ km^{-1}, the intensity of the background spatial component, known as the DC continuous component, is depicted.

As spatial frequencies increase, progressing toward the DFT log-amplitude's edge, the intensities of progressively smaller spatial components are depicted. At the maximum spatial frequencies, corresponding to half of the sampling frequency $(1/480$ m$^{-1})$ as per the Nyquist limit, the intensities of spatial components at the smallest scale (480 m), such as step signals,
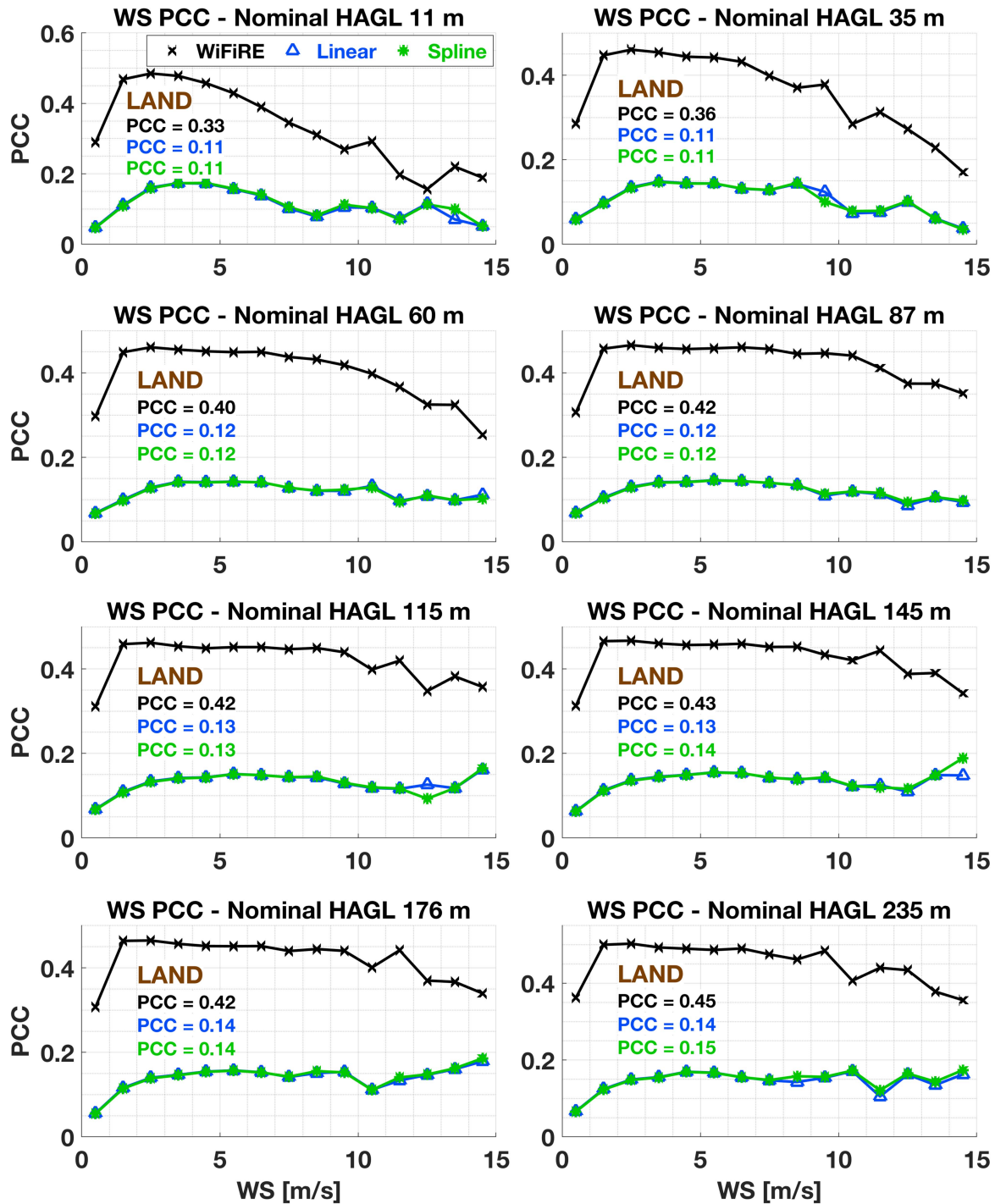
Fig. 19. Comparative binned analysis of the RMSD for WS among the outputs generated by the WiFiRE algorithm and those calculated by the two proposed interpolation methods across different σ-levels over land surface.

are represented. Consequently, the Spline interpolation in Fig. 26 exhibits the lowest spatial resolution, followed by that associated with the WiFiRE algorithm, and finally, the highest spatial resolution among the three is observed in the WRF output at 240 m. While it is evident that images possess different spatial frequency content, it is not straightforward to determine the highest frequency actually correlated with a signal, thus defining

the spatial resolution. Hence, the procedure outlined in Section V was employed to address this limit.

To achieve this, all examined scenarios underwent preliminary preprocessing with the Hanning window, as detailed in Section III-B, before being subjected to Mizutani's method for analysis. Fig. 27 provides an illustration of the spatial resolution assessment procedure applied to the same dataset depicted in
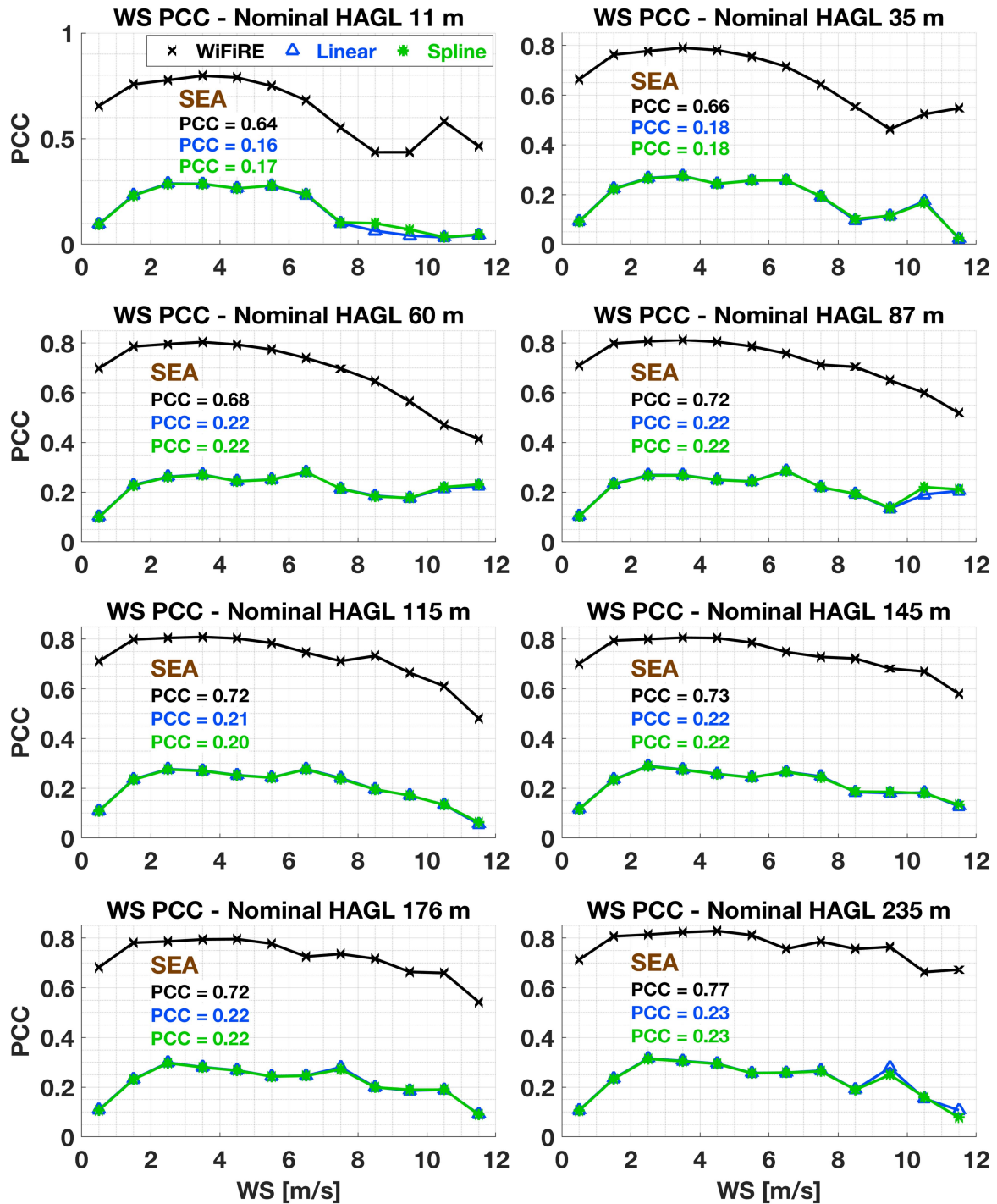
Fig. 20. Comparative binned analysis of the RMSD for WS among the outputs generated by the WiFiRE algorithm and those calculated by the two proposed interpolation methods across different σ-levels over land sea.

Fig. 26. The resulting spatial resolution of WS is approximately 0.68 km for the WRF model output, 1.69 km for the Spline interpolation, and 0.76 km for the WiFiRE algorithm. Fig. 28 displays the profiles of mean values and standard deviations of spatial resolutions calculated across all 96 scenarios of the Evaluation dataset. Overall, minimal variation is observed along the vertical profile. The averaged values over eight σ-levels indicate

a spatial resolution of 0.6–0.7 km for the WRF model, 0.8 km for WiFiRE, 1.8–1.9 km for Spline interpolation, and 2.0–2.4 km for linear interpolation. The standard deviations remain less than 0.2 km across the board. Fig. 29 summarizes the results of the noise assessment using Immerkaer's method, presenting vertical profiles of mean and standard deviation calculated across 96 scenarios of the Evaluation dataset. The mean value of the noise

Fig. 21. Comparative binned analysis of the PCC for WS among the outputs generated by the WiFiRE algorithm and those calculated by the two proposed interpolation methods across different σ-levels over land surface.

is maximum for the WRF model, approximately 2×10^{-2} m/s across all σ-levels in average. For the WiFiRE output, the estimated noise is 1×10^{-2} m/s, while for the two interpolation methods, values are one or two orders of magnitude smaller. Generally, the standard deviations are one order of magnitude smaller than the mean values.

VII. DISCUSSION

The analysis of the number of DoFs reveals that the ANNs were trained with a sufficiently small number of inputs and nodes to mitigate the risk of overfitting. Generally, the number of DoFs indicates the complexity of the ANN; the higher it is, the more capable the ANN is of fitting the training dataset, but

Fig. 22.   Comparative binned analysis of the PCC for WS among the outputs generated by the WiFiRE algorithm and those calculated by the two proposed interpolation methods across different σ-levels over sea surface.

there is also a higher risk of overfitting. The DoFs value for the ANNs trained for the WiFiRE algorithm is approximately 3×10^3, which is two orders of magnitude smaller than the size of the training dataset (around 6×10^5), and three orders of magnitude smaller than the number of training equations. The latter was calculated by multiplying the size of the training dataset by the number of outputs, ranging from 22 to 32

(see Table IV). These large differences mitigate the risk of overfitting and validate the method adopted for defining the ANN architectures [102]. As expected, the number of inputs and DoFs decreases with increasing $HAGL$. This is because the wind fields nearest to the surface exhibit greater spatial variability and thus require more information and complexity for downscaling.
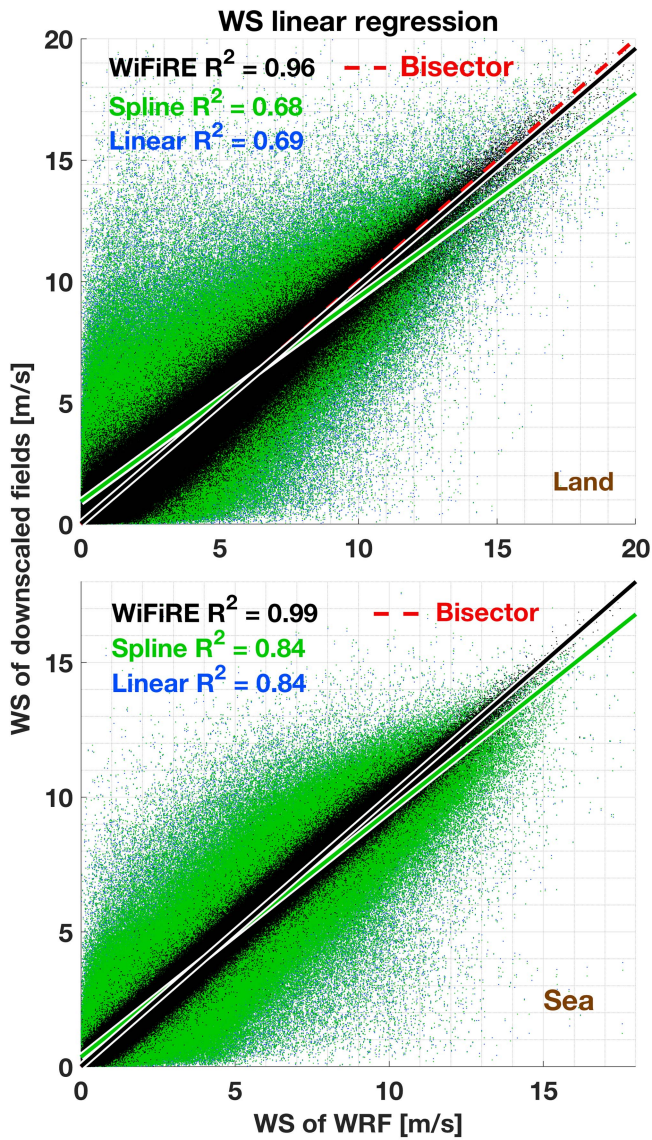
Fig. 23. WS linear regression for the output of the WiFiRE algorithm, spline, and linear interpolation against the target value of the WRF-LES model. To enhance the readability of the graph, only one data point per every 500 points is displayed.
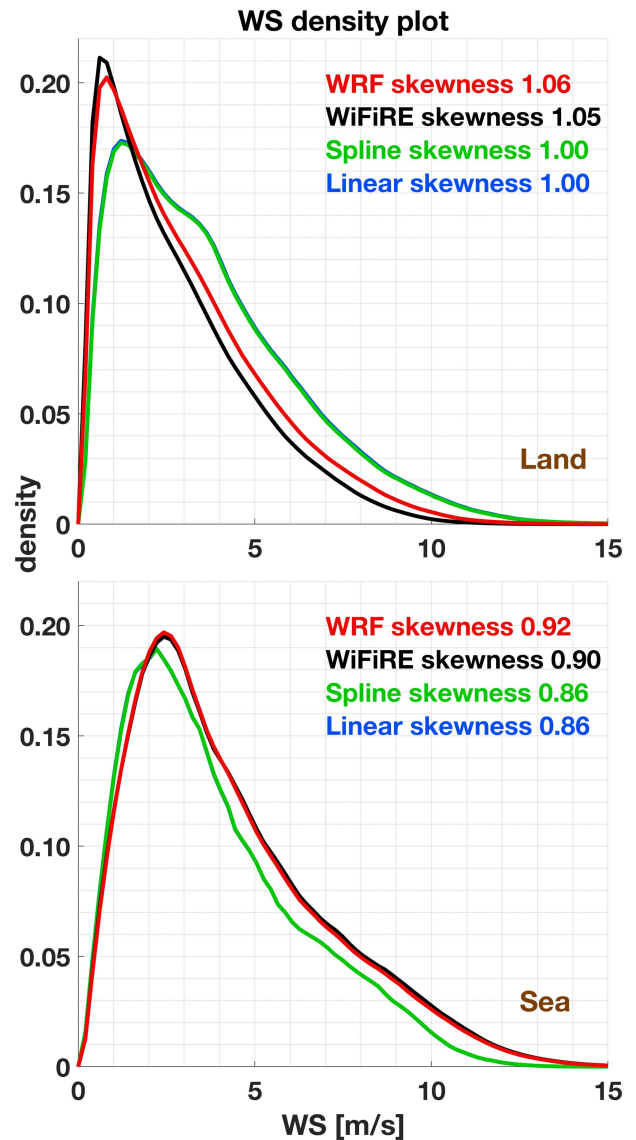
Fig. 24. WS density plot for the output of the WiFiRE algorithm, the spline and linear interpolation, and the WRF-LES model.

The analysis of inputs and outputs confirms our expectations, highlighting the horizontal wind component as the most influential input in the downscaled process. In addition, other crucial inputs from the WRF model include the vertical wind component and the friction velocity. Although of lesser significance, variables such as temperature, pressure, humidity, and air density also play a role in characterizing atmospheric conditions. Among the static variables, surface altitude emerges as the most influential, followed closely by the component of the normal versor to the earth's surface, particularly in alignment with the downscaled wind component. Conversely, variables, such as land fraction, exhibit minimal impact, likely due to redundancy with surface roughness, which itself is of low importance due to the redundancy of friction velocity. Geopotential height, despite its wide variation within a σ-level, appears negligible, possibly

because it redundantly conveys information already captured by ground height combined with the near-constant value over the entire σ-level. Overall, a diminishing trend in the number of PCs with HAGL is evident, affecting both the outputs and several inputs. As the σ-level lowers, the number of selected PCs increases, a result of the enhanced spatial variability brought about by wind interactions with the ground surface.

A comparison between the outcomes of the WiFiRE algorithm and those of the interpolations underscores the WiFiRE's superior ability to capture the high spatial variability of WS with a level of detail that the interpolation methods lack. In contrast, the interpolations tend to smooth out the WS, reducing the range between the minimum and maximum values observed at 1.2 km grid spacing. This flattening effect is attributed to the coarser resolution and sampling inherent in the interpolations compared to the finer resolution achieved with the WiFiRE algorithm. As a
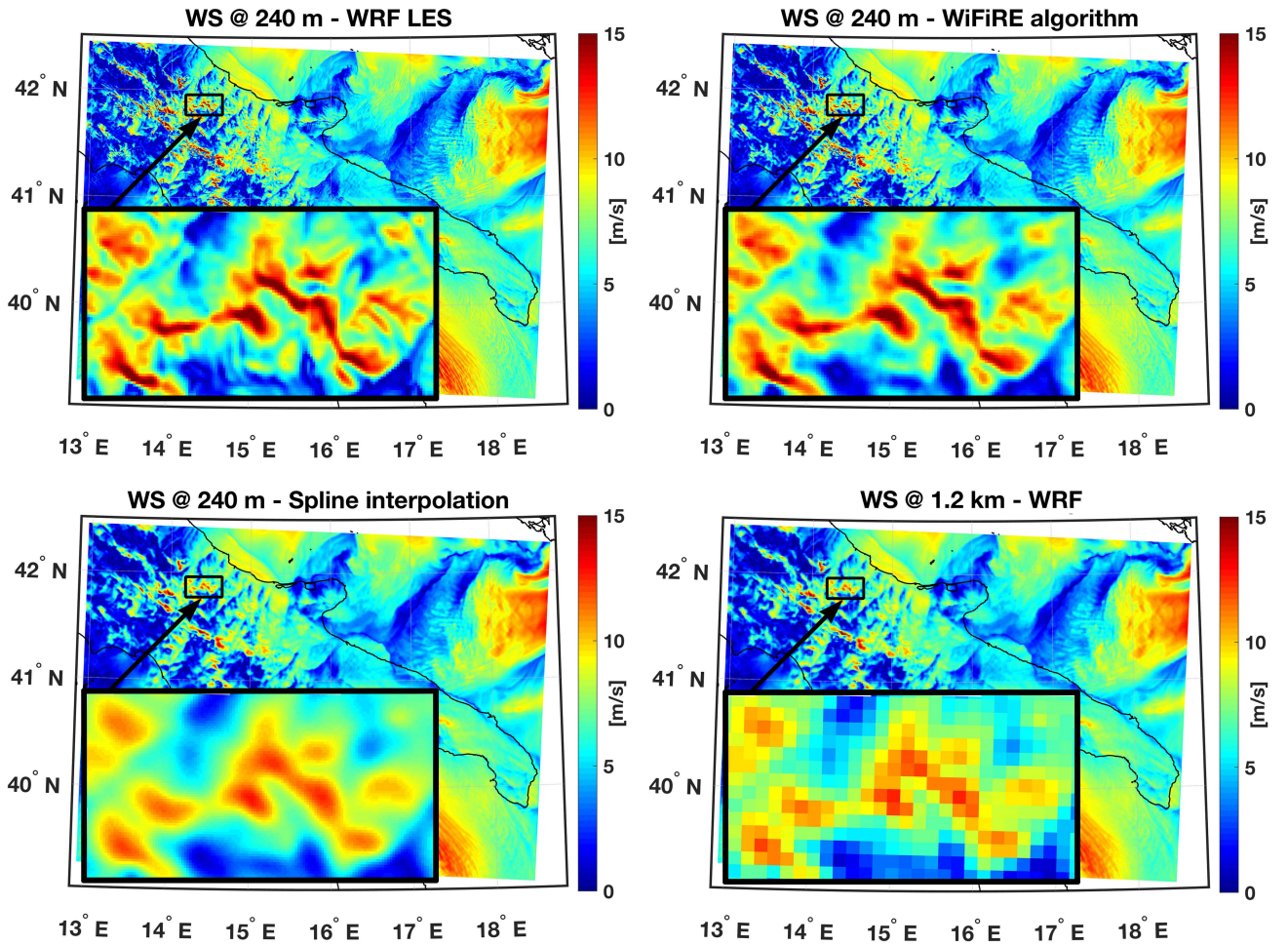
Fig. 25.　Example of downscaling results for the third σ-level (60 m HAGL) for the WRF simulation at 06:00 UTC on 15-03-2017.

result, the interpolation method falls short in accurately capturing the dynamics of the values, often truncating the extremes. This is well highlighted in the binned analyses, which shows an overestimation of low wind speeds and an underestimation of higher ones. In contrast, the WiFiRE algorithm improves in reconstructing field dynamics, yielding values closer to those of the WRF model at 240 m. The density plots confirm these results, with distributions more similar to each other for the outputs of the WRF model and the WiFiRE algorithm than those of the interpolations. This result is also evident in the analysis of vertical profiles, where the WiFiRE profiles closely mirror those of the WRF model, while the interpolations exhibit greater deviation. Furthermore, the PCC analysis highlights the WiFiRE algorithm's superior performance in accurately reconstructing wind field structures, including extremes, outperforming the interpolations.

Overall, the WiFiRE algorithm's downscaled fields demonstrate a closer alignment with the WRF output at 240 m compared to the interpolations, which produce notably similar results to each other.

The MBD of the vertical profiles consistently hovers around zero for the WiFiRE algorithm, yet is nonnegligible for the interpolation methods. Specifically, when assessing WS over land,

the WiFiRE algorithm outperforms the interpolation methods, exhibiting an average improvement of approximately 0.3 m/s for MBD and 1.1 m/s for RMSD across all levels. In particular, for the third and fourth σ-levels over land, corresponding to approximately 60 m and 87 m $HAGL$—most significant levels for wind turbines in the South of Italy—the disparities between the WiFiRE algorithm and the interpolations amount to approximately 0.4 m/s for MBD and 1.5 m/s for RMSD. The overall improvement achievable using the WiFiRE algorithm compared to the interpolation methods is significant. An error less than 1 m/s in WS estimation can equate to millions of dollars in annual revenue loss [4]. With the wind power proportional to the cube of WS, the power error (PE) between estimated power $\hat{P}$ and actual power P can be defined as

$$\text{PE} = \left[1 - \left(\frac{\hat{P}}{P} \right) \right] \cdot 100 \qquad (31)$$

$$\text{PE} = \left[1 - \left(\frac{WS + \text{error}}{WS} \right)^3 \right] \cdot 100. \qquad (32)$$

Using the *cut-in* speed of 3 m/s as an example for WS, which indicates the threshold at which a turbine starts generating power
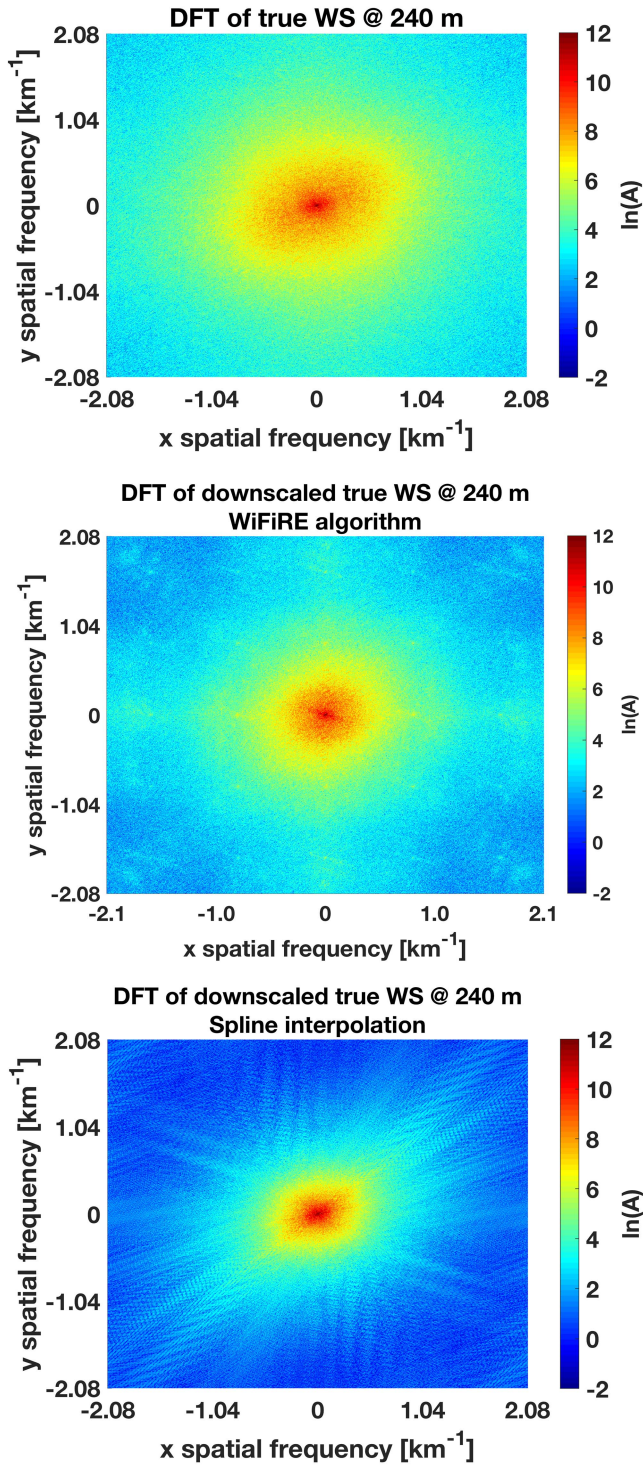
Fig. 26. Comparison of the DFT log-amplitudes of the WS output at 240 m against the downscaled true WS using both spline interpolation and the WiFiRE algorithm. WRF simulation at 06:00 UTC on 15-03-2017.

[103], and considering the MBD as the error metric, the PE for the Spline interpolation at 60 m HAGL (MBD -0.2 m/s) is approximately -21%, whereas the WiFiRE algorithm shows virtually no error (MBD about 0). For a typical *rated-speed* of 10 m/s, representing the speed at which the turbine achieves its maximum rated power, the PEs for the Spline interpolation

(MBD about -1 m/s) and the WiFiRE algorithm (MBD about -0.1 m/s) are 27% and 3%, respectively. This indicates a difference of 24% at the maximum production. If the RMSDs were utilized as the error metric, these differences would be further magnified.

Although downscaling other meteorological fields than wind components can support wind energy forecasts, they were not considered in this study due to their secondary importance. In fact, the available wind power P_{av} of the e free-air stream that flows through a rotor cross-sectional area A_r can be written as [104]

$$P_{av} = \frac{1}{2} A_r D_{air} WS^3 \tag{33}$$

where D_{air} is the air density. Since D_{air} depends on air temperature, pressure, and humidity, it might be useful to downscale these variables as well, or more simply D_{air}. However, WS remains the most crucial variable due to its cubic dependence and greater spatial variability compared to D_{air}.

For instance, in the Evaluation dataset, the (mean $\pm$ standard deviation) within the (5×5) box at 240 m for the fourth σ-level yields approximately (4.0 ± 0.3) m/s and (1.179 ± 0.002) kg/m^3 for WS and D_{air}, respectively. The magnitude difference between mean and standard deviation is one order for WS and three orders for D_{air}.

The analysis of spatial resolution, although carried out under simplified assumptions, is consistent with the results previously obtained. In particular, the analysis performed in Section III-A, where a Gaussian low-pass filter had to be applied prior to sampling, revealed differences in both sampling and spatial resolution between the wind fields in the D02 and D03 domains. Consequently, WiFiRE algorithm's capability of reconstructing the wind field akin to the WRF model suggests an enhancement in spatial resolution consistent with the high level of detail that can be observed in downscaled fields. The calculated spatial resolutions show reasonable values overall and meet the Nyquist limit of 1/480 m^{-1}. Indeed, the highest spatial resolution, estimated at 600 m, corresponds to the output of the WRF model. This resolution translates to a value of (1/600) m^{-1} spatial frequency, which falls below the Nyquist limit. The same limit applies to the downscaled fields, resulting from the spatial resampling process alone from 1.2 km to 240 m. However, linear interpolation only marginally increases the maximum spatial frequency present in the signal. For the wind components U and V—those downscaled, as WS is their sum—the maximum spatial frequency is 1/2.4 km^{-1}. It is noteworthy that this value matches the Nyquist limit of the nondownscaled wind field at 1.2 km. This indicates that linear interpolation allowed for the highest spatial frequency theoretically present in nondownscaled fields but failed to surpass it. The spline interpolation, being a cubic interpolation allowed for slightly better results, by introducing higher spatial frequencies, estimated at 1/1.8 km^{-1} for the U and V components but considerably lower than that obtained with the WiFiRE algorithm (1/0.8 km^{-1}). The standard deviation is contained within 17% of the estimated resolution at most, showing reasonable fluctuations overall. The noise assessment shows a maximum value of 10^{-2} m/s for the WRF
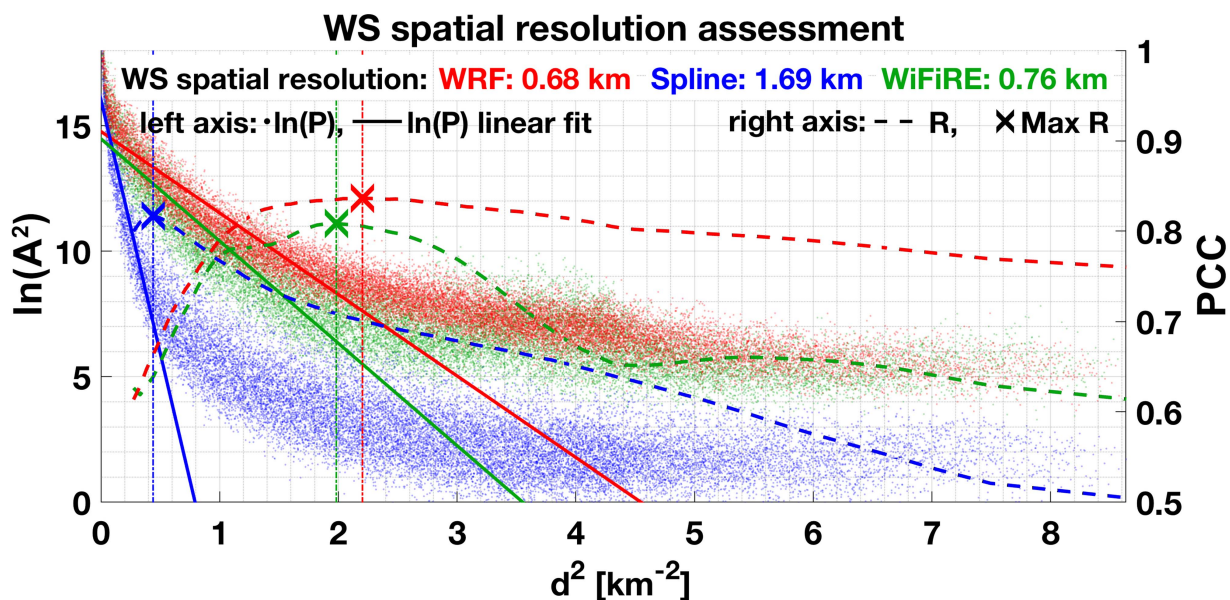
Fig. 27.   Spatial resolution assessment of the WS for the output of the WRF at 240 m (red), spline interpolation (blue), and the WiFiRE algorithm (green) for the third σ-level (~61 m HAGL) for the WRF simulation at 06:00 UTC on 15-03-2017. The point clouds and regression lines refer to the left y-axis, while dashed lines with PCCs values are relative to the right y-axis. The linear fit is calculated for each cloud points from zero up to the d^2_{thr} identified by the cross marker corresponding to the maximum values of the dash line (max PCC). To make the graph more readable, only 1 point per 10 is shown.
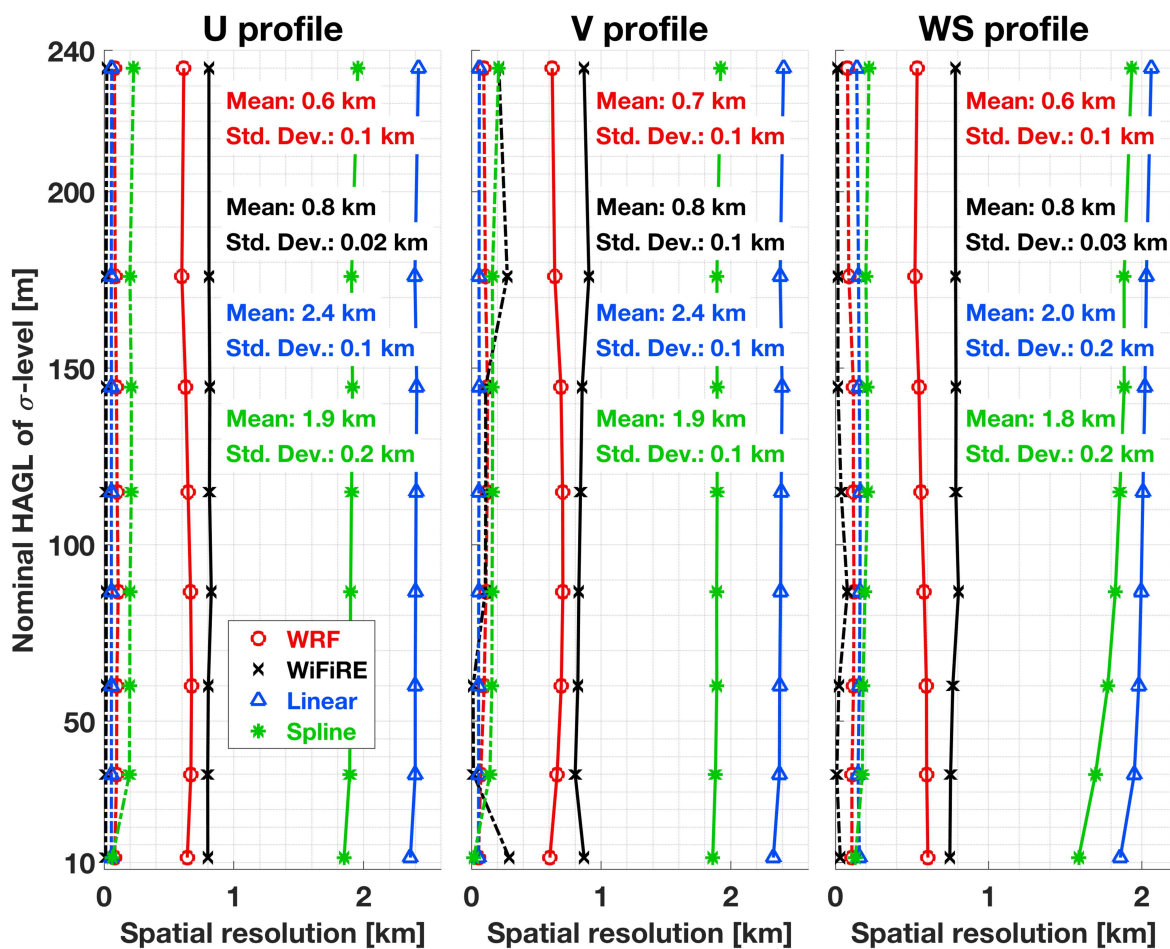
Fig. 28.   Vertical profiles of the mean (solid lines) and standard deviation (dashed lines) of the estimated spatial resolution for the WRF output, WiFiRE algorithm output, and the two proposed interpolation methods across different σ-levels.
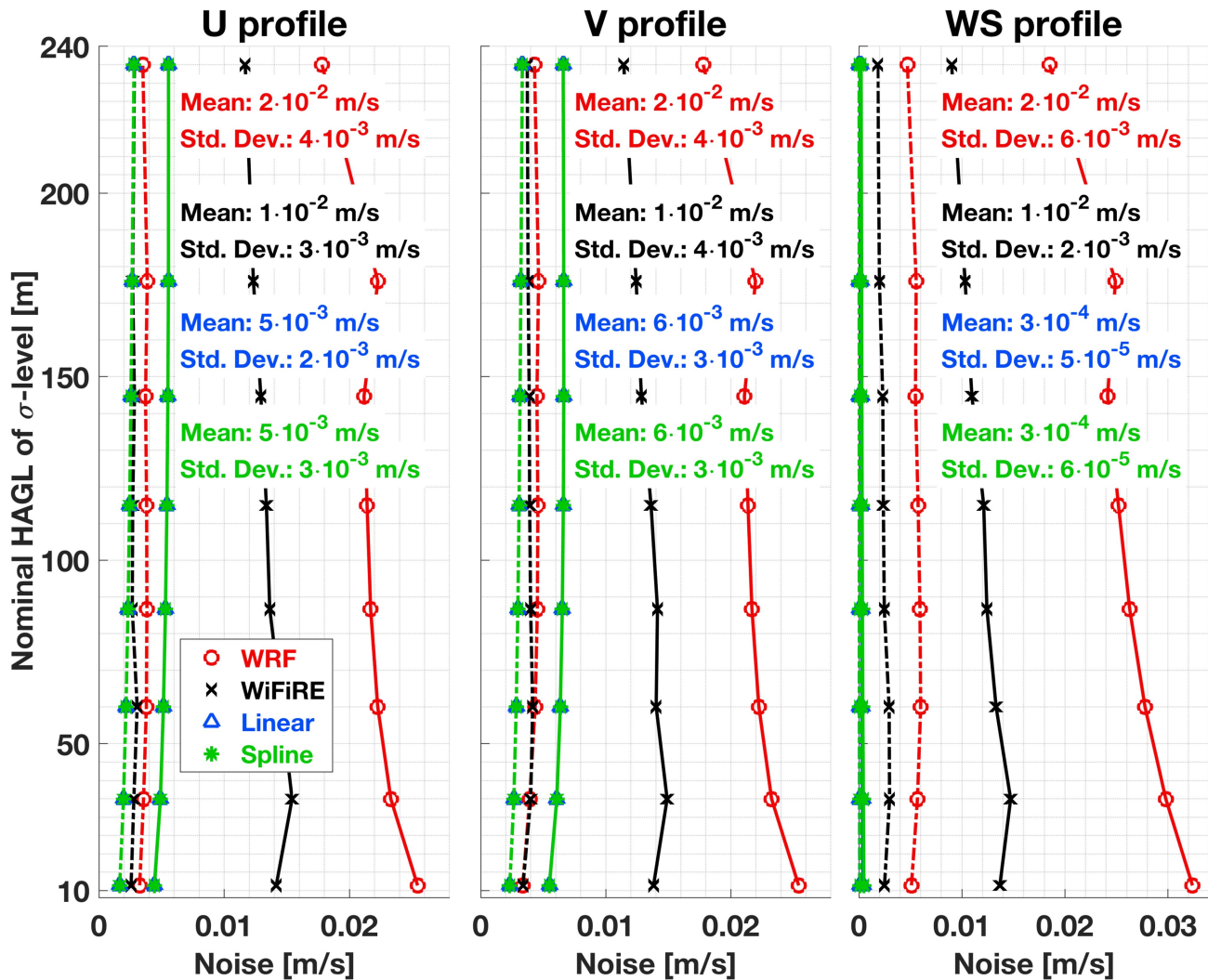
Fig. 29. Vertical profiles of mean (solid lines) and standard deviation (dashed lines) of the estimated noise for the WRF output, WiFiRE algorithm output, and the two proposed interpolation method across different σ-levels.

model. This could be attributed either to a numerical effect of the model or to an imperfect removal of structures operated by the filter L of (26). However, the values obtained are very low and thus deemed negligible.

Overall, the developed algorithm enables the downscaling of wind fields at a superior spatial resolution and with fewer errors compared to the two proposed interpolation methods.

Although the results obtained by the WiFiRE algorithm do not perfectly match those from the WRF-LES at 240 m, the computational cost is significantly reduced. For instance, employing the WRF model with three domains at 3.6 km, 1.2 km, and 240 m grid spacing over the study area in southern Italy demands approximately 20 h of computation time per hour of output on a server equipped with 56 cores running at 2.6 GHz and 256 GB of RAM. Conversely, utilizing the model with only two domains at 3.6 and 1.2 km, combined with the WiFiRE algorithm, requires only about 20 min—15 min for WRF simulation and 5 min for applying the WiFiRE algorithm.

VIII. CONCLUSION

The study has detailed an ANN-based algorithm, WiFiRE, developed for downscaling the WS from the WRF model at 1.2 km grid spacing to a finer spacing at 240 m. This process involves the first 8 σ-levels within the first 250 m $HAGL$ for wind power generation. The input analysis revealed that the PCs of wind's horizontal and vertical components, horizontal speed, and friction velocity are of utmost importance among the values calculated by the WRF model at 1.2 km. Pressure, humidity, air density, and temperature PCs also contribute, although to a lesser extent, yet support the characterization of atmospheric conditions. For the surface static variables at 240 m used in the downscaling, the PCs of ground height and the two components of the surface normal versor directed eastward and northward were found to be particularly relevant. The upward-directed component offered a lesser contribution, while surface roughness, geopotential height, land fraction, and geographical

coordinates were considered to have minor or almost negligible importance. The comparison with the WRF output at 240 m demonstrates that the WiFiRE algorithm outperforms both linear and spline interpolations, which serve as the baseline for evaluation, across various metrics including MBD, RMSD, and PCC, observed over both land and sea. In addition, in terms of spatial resolution, the algorithm yields superior results compared to interpolations, without introducing a notable increase in noise. Future studies will concentrate on validating the algorithm using real measurements. This validation will include assessing its performance alongside that of the WRF model across various configurations. In addition, the study will investigate the effects of downscaling other meteorological variables on wind turbine power curves. Furthermore, optimal methods for vertical spatial resolution will be explored to enhance the output of the WiFiRE algorithm. The approach proposed in this study could extend to other domains requiring HRES meteorological variable reanalysis or forecasting and could assist in evaluating solar irradiance to optimize photovoltaic system energy production or for surface agro-meteorological variables to support precision agriculture.

APPENDIX A
ANN TRAINING ALGORITHMS

The supervised training algorithm functions as an iterative process based on the error backpropagation algorithm, a method applied to a Training dataset to discover optimal values for weights and biases which starts from random weights and biases. The algorithm calculates the output for each iteration, comparing it to the output of the training dataset and calculates a suitable cost function C, often equal to the MSE. The weights and biases are subsequently adjusted by minimizing the cost function, a process that involves calculating its partial derivatives $\partial C/\partial w$ and $\partial C/\partial b$ with respect to each weight w and bias b. This method helps converge, iteration by iteration, toward a local minimum. The term "backpropagation" refers to the technique used to calculate the partial derivatives, starting from the output nodes and proceeds backward through the hidden layers to the input layer [105]. The iterative process ceases when the cost function C hits its minimum or when the iterations no longer lead to an acceptable improvement.

A. Resilient Backpropagation

The Resilient Backpropagation algorithm hinges on an adaptive learning scheme. For each iteration—or epoch—the weights are adjusted by adding a corrective term Δw_{ij} based on the squared error cost function E, with positive sign if $\partial E/\partial w_{ij}$ is positive and negative sign, otherwise. The value of Δw_{ij} is initially set equal to a starting value Δ_0. If the sign of $\partial E/\partial w_{ij}$ has not changed from the previous epoch, it is multiplied by η^+, or η^-, otherwise. The update of the corrective term Δw_{ij} is confined in the range between $\Delta_{\min}$ and $\Delta_{\max}$. The parameters are not particularly critical and are commonly chosen as suggested by Riedmiller and Braun [41]. These include $\Delta_0 = 0.1$, $\Delta_{\min} = 1e-6$, $\Delta_{\max} = 50$, $\eta^+ = 1.2$ ed $\eta^- = 0.5$ [106], [107].

B. Levenberg–Marquardt

The Levenberg–Marquardt algorithm also relies on an adaptive learning scheme. Unlike the previous one, it uses both the first and second derivatives of the squared error with respect to the weights to converge faster to a local minimum. The vector of all the N weights and biases w_n at the t_{th} epoch is defined as $\boldsymbol{w^{(t)}}$. Its update is calculated using

$$\boldsymbol{w^{(t)}} = \boldsymbol{w^{(t-1)}} - \left[\boldsymbol{J^T J} + \mu \boldsymbol{I}\right]^{-1} \boldsymbol{J^T e} \qquad (A1)$$

where $\boldsymbol{e}$ is the vector of the errors e_{kp}, obtained as the difference between the k_{th} output node of the p_{th} training pattern and the corresponding training target. $\boldsymbol{J}$ is the Jacobian matrix, which contains the first-order partial derivatives of the errors e_{kp} with respect to the weights and biases w_n. $\boldsymbol{I}$ is the identity matrix, and μ is a dynamically adjusted learning parameter during the training process to control the algorithm's behavior.

The product of $\boldsymbol{J^T e}$ is the gradient of the squared error, and the product of $\boldsymbol{J^T J}$ is used to approximate the Hessian matrix made up of the second-order partial derivatives of e_{kp} with respect to w_n. This approximation is valid as the cost function consists of a sum of squared terms, i.e., the sum of squared errors. In the first training epoch, the learning parameter μ is set equal to an initial value μ_{ini} and the weights and biases are initialized with random values. In subsequent epochs, the weights and biases are updated according to (A1), and the squared error is evaluated. If it results less than that of the previous epoch, the weight and bias update is accepted, and the parameter μ is updated by dividing it by a factor β. Otherwise, the update is rejected, μ is updated by multiplying it by the same factor β, and the weight and biases update is calculated using (A1) again, accepting or rejecting the new update according to the same scheme. The configuration parameters are not particularly critical and are assumed to be equal to the values widely used in literature: $\mu_{\text{ini}} = 10^{-3}$ e $\beta = 10$ [108], [109].

APPENDIX B
– REMOVAL OF ANN INPUTS AND UPDATING OF WEIGHTS

The input removal procedure and the subsequent weight adjustment were calculated using the corrective term δ_{nm}, which needed to be added to the weights w_{nm}. These weights exist between the nth input and the mth node of the first hidden layer

$$\sum_{n=1}^{N} w_{nm} h_n^{(d)} = \sum_{n=1}^{N-1} \left(w_{nm} + \delta_{nm}\right) h_n^{(d)} \qquad (B1)$$

where N represents the number of the ANN's inputs and $h_n^{(d)}$ is the nth input of the dth training pattern. The left member represents the input to the mth node of the first hidden layer due to the dth training pattern, taking into account all N inputs of the ANN. The right member illustrates the adjusted value following the input removal, achieved through the addition of the corrective terms δ_{nm}. If r is defined as the index of the removed input, (B1) can be rephrased as

$$\sum_{n=1}^{N-1} \delta_{nm} h_n^{(d)} = w_{rm}\, h_r^{(d)}. \tag{B2}$$

This equation, when applied to all D patterns, can be depicted in matrix form as

$$\boldsymbol{h_{\sim r}}\, \boldsymbol{\delta_m} = w_{rm}\, \boldsymbol{h_r} \tag{B3}$$

where $\boldsymbol{h_{\sim r}}$ is the matrix of D rows and $N-1$ columns containing all training patterns and all inputs, excluding the removed one. $\boldsymbol{\delta_m}$ is the column-vector of $N-1$ elements containing the corrective terms for updating the connection weights between the unremoved inputs and the mth node of the first hidden layer, while $\boldsymbol{h_r}$ is the column vector of D elements containing the removed input for all training patterns. The transposition operation is represented by $(\cdot)^{\boldsymbol{T}}$, and by multiplying both sides of (B3) by the transpose of $\boldsymbol{h_{\sim r}}$, it can be rewritten as

$$\boldsymbol{h_{\sim r}^T}\, \boldsymbol{h_{\sim r}}\, \boldsymbol{\delta_m} = \boldsymbol{h_{\sim r}^T}\, w_{rm}\boldsymbol{h_r} \tag{B4}$$

which can be depicted as

$$\boldsymbol{A}\, \boldsymbol{\delta_m} = \boldsymbol{b} \tag{B5}$$

with $\boldsymbol{A} = \boldsymbol{h_{\sim r}^T}\, \boldsymbol{h_{\sim r}}$ and $\boldsymbol{b} = \boldsymbol{h_{\sim r}^T}\, w_{rm}\boldsymbol{h_r}$. Defining $\|\cdot\|$ as the Euclidean norm, it is possible to find a pseudosolution of (B5) minimizing the quadratic error ρ

$$\rho = \|\boldsymbol{A}\boldsymbol{\delta_m} - \boldsymbol{b}\|_2 \tag{B6}$$

by using the CG method, given that $\boldsymbol{A}$, as defined, is an $(N-1) \times (N-1)$ square matrix, symmetric and positive definite. The CG method is a well-known iterative procedure, which requires a low computational cost, and which allowed in about 10^2 iterations to solve the proposed problem, by reducing the relative residual error ρ_{rel} below the tolerance threshold, arbitrarily chosen equal to 10^{-8}

$$\rho_{\text{rel}} = \frac{\|\boldsymbol{A}\boldsymbol{\delta_m} - \boldsymbol{b}\|_2}{\|\boldsymbol{b}\|_2} \tag{B7}$$

Equation (B7) needs to be solved for all M nodes of the first hidden layer, and the resulting ANN from the corresponding weight update does not require any additional training steps.

REFERENCES

[1] R. J. Barthelmie and S. C. Pryor, "Climate change mitigation potential of wind energy," *Climate*, vol. 9, no. 9, Aug. 2021, Art. no. 136, doi: 10.3390/cli9090136.

[2] M. S. Nazir, N. Ali, M. Bilal, and H. M. Iqbal, "Potential environmental impacts of wind energy development: A global perspective," *Curr. Opin. Environ. Sci. Health*, vol. 13, pp. 85–90, Feb. 2020, doi: 10.1016/j.coesh.2020.01.002.

[3] M. Hutchinson and F. Zhao, "Global wind report 2023," Global Wind Power Council, Brussels, Belgium, Apr. 2023. [Online]. Available: https://gwec.net/globalwindreport2023/

[4] P. F. Melani, F. Di Pietro, M. Motta, M. Giusti, and A. Bianchini, "A critical analysis of the uncertainty in the production estimation of wind parks in complex terrains," *Renewable Sustain. Energy Rev.*, vol. 181, Jul. 2023, Art. no. 113339, doi: 10.1016/j.rser.2023.113339.

[5] M. R. Davidson and D. Millstein, "Limitations of reanalysis data for wind power applications," *Wind Energy*, vol. 25, no. 9, pp. 1646–1653, Jun. 2022, doi: 10.1002/we.2759.

[6] I. Durre, R. S. Vose, and D. B. Wuertz, "Overview of the integrated global radiosonde archive," *J. Climate*, vol. 19, no. 1, pp. 53–68, Jan. 2006, doi: 10.1175/JCLI3594.1.

[7] T. Driesenaar et al., "Quality information document for the global ocean wind products WIND_GLO_WIND_L3_NRT_OBSERVATIONS_012_002 WIND_GLO_WIND_L3_REP_OBSERVATIONS_012_005 WIND_GLO_PHY_CLIMATE_L4_REP_012_003© EU copernicus marine service," 2022, Last Access: Jul. 26, 2023. [Online]. Available: https://catalogue.marine.copernicus.eu/documents/QUID/CMEMS-WIND-QUID-012-002-003-005.pdf

[8] H. Hersbach et al., "The ERA5 global reanalysis," *Quart. J. Roy. Meteorological Soc.*, vol. 146, no. 730, pp. 1999–2049, Jul. 2020, doi: 10.1002/qj.3803.

[9] E. Kalnay et al., "The NCEP/NCAR 40-year reanalysis project," in *Renewable Energy*. Evanston, IL, USA: Routledge, 2018, pp. 146–194.

[10] R. Gelaro et al., "The modern-era retrospective analysis for research and applications, version 2 (MERRA-2)," *J. Climate*, vol. 30, no. 14, pp. 5419–5454, Jul. 2017, doi: 10.1175/JCLI-D-16-0758.1.

[11] S. Rose and J. Apt, "What can reanalysis data tell us about wind power?," *Renewable Energy*, vol. 83, pp. 963–969, Nov. 2015, doi: 10.1016/j.renene.2015.05.027.

[12] K. L. Nefabas, L. Söder, M. Mamo, and J. Olauson, "Modeling of Ethiopian wind power production using era5 reanalysis data," *Energies*, vol. 14, no. 9, Apr. 2021, Art. no. 2573, doi: 10.3390/en14092573.

[13] J. Bosch, I. Staffell, and A. D. Hawkes, "Temporally-explicit and spatially-resolved global onshore wind energy potentials," *Energy*, vol. 131, pp. 207–217, Jul. 2017, doi: 10.1016/j.energy.2017.05.052.

[14] C. Draxl, A. Clifton, B. M. Hodge, and J. McCaa, "The wind integration national dataset (wind) toolkit," *Appl. Energy*, vol. 151, pp. 355–366, Aug. 2015, doi: 10.1016/j.apenergy.2015.03.121.

[15] A. N. Hahmann et al., "The making of the New European Wind Atlas–part 1: Model sensitivity," *Geoscientific Model Develop.*, vol. 13, no. 10, pp. 5053–5078, Oct. 2020, doi: 10.5194/gmd-13-5053-2020.

[16] W. Miller, "Predicting wind power with greater accuracy," *Sci. Technol. Rev.*, Apr./May 2014, pp. 1–9. [Online]. Available: https://str.llnl.gov/content/pages/april-2014/pdf/04.14.1.pdf

[17] J. Zhao, Z. H. Guo, Z. Y. Su, Z. Y. Zhao, X. Xiao, and F. Liu, "An improved multi-step forecasting model based on WRF ensembles and creative fuzzy systems for wind speed," *Appl. Energy*, vol. 162, pp. 808–826, Jan. 2016, doi: 10.1016/j.apenergy.2015.10.145.

[18] A. Dinler, "Reducing balancing cost of a wind power plant by deep learning in market data: A case study for Turkey," *Appl. Energy*, vol. 289, May 2021, Art. no. 116728, doi: 10.1016/j.apenergy.2021.116728.

[19] J. Jin, Y. Che, J. Zheng, and F. Xiao, "Uncertainty quantification of a coupled model for wind prediction at a wind farm in Japan," *Energies*, vol. 12, no. 8, Apr. 2019, Art. no. 1505, doi: 10.3390/en12081505.

[20] B. Yang et al., "State-of-the-art one-stop handbook on wind forecasting technologies: An overview of classifications, methodologies, and analysis," *J. Cleaner Prod.*, vol. 283, Feb. 2021, Art. no. 124628, doi: 10.1016/j.jclepro.2020.124628.

[21] Z. Tian, H. Li, and F. Li, "A combination forecasting model of wind speed based on decomposition," *Energy Rep.*, vol. 7, pp. 1217–1233, Nov. 2021, doi: 10.1016/j.egyr.2021.02.002.

[22] M. Santhosh, C. Venkaiah, and D. M. Vinod Kumar, "Current advances and approaches in wind speed and wind power forecasting for improved renewable energy integration: A review," *Eng. Rep.*, vol. 2, no. 6, Jun. 2020, Art. no. e12178, doi: 10.1002/eng2.12178.

[23] M. N. Khoshrodi, M. Jannati, and T. Sutikno, "A review of wind speed estimation for wind turbine systems based on Kalman filter technique," *Int. J. Elect. Comput. Eng.*, vol. 6, no. 4, pp. 1406–1411, Aug. 2016, doi: 10.11591/ijece.v6i4.pp1406-1411.

[24] E. Erdem and J. Shi, "ARMA based approaches for forecasting the tuple of wind speed and direction," *Appl. Energy*, vol. 88, no. 4, pp. 1405–1414, Apr. 2011, doi: 10.1016/j.apenergy.2010.10.031.

[25] S. N. Singh and A. Mohapatra, "Repeated wavelet transform based ARIMA model for very short-term wind speed forecasting," *Renewable Energy*, vol. 136, pp. 758–768, Jun. 2019, doi: 10.1016/j.renene.2019.01.031.

[26] Z. Dzulfikri, N. Nuryanti, and Y. Erdani, "Design and implementation of artificial neural networks to predict wind directions on controlling yaw of wind turbine prototype," *J. Robot. Control*, vol. 1, no. 1, pp. 20–26, 2020, doi: 10.18196/jrc.1105.

[27] S. Barhmi and O. El Fatni, "Hourly wind speed forecasting based on support vector machine and artificial neural networks," *Int. J. Artif. Intell.*, vol. 8, no. 3, pp. 286–291, Sep. 2019, doi: 10.11591/ijai.v8.i3.pp286-291.

[28] M. U. Yousuf, I. Al-Bahadly, and E. Avci, "Current perspective on the accuracy of deterministic wind speed and power forecasting," *IEEE Access*, vol. 7, pp. 159547–159564, 2019, doi: 10.1109/ACCESS.2019.2951153.

[29] W. Y. Chang, "A literature review of wind forecasting methods," *J. Power Energy Eng.*, vol. 2, pp. 161–168, Apr. 2014, doi: 10.4236/jpee.2014.24023.

[30] Y. Liu, Y. Liu, D. Muñoz-Esparz, F. Hu, C. Yan, and S. Miao, "Simulation of flow fields in complex terrain with WRF-LES: Sensitivity assessment of different PBL treatments," *J. Appl. Meteorol. Climatol.*, vol. 59, no. 9, pp. 1481–1501, Sep. 2020, doi: 10.1175/JAMC-D-19-0304.1.

[31] M. Udina, À. Montornès, P. Casso, B. Kosović, and J. Bech, "WRF-LES simulation of the boundary layer turbulent processes during the BLLAST campaign," *Atmosphere*, vol. 11, no. 11, Oct. 2020, Art. no. 1149, doi: 10.3390/atmos11111149.

[32] S. Hanifi, X. Liu, Z. Lin, and S. Lotfian, "A critical review of wind power forecasting methods—Past, present and future," *Energies*, vol. 13, no. 15, Jul. 2020, Art. no. 3764, doi: 10.3390/en13153764.

[33] A. Castorrini, S. Gentile, E. Geraldi, and A. Bonfiglioli, "Investigations on offshore wind turbine inflow modelling using numerical weather prediction coupled with local-scale computational fluid dynamics," *Renewable Sustain. Energy Rev.*, vol. 171, Jan. 2023, Art. no. 113008, doi: 10.1016/j.rser.2022.113008.

[34] G. Yakoub, S. Mathew, and J. Leal, "Downscaling and improving the wind forecasts from NWP for wind energy applications using support vector regression," *J. Phys., Conf. Ser.*, vol. 1618, no. 6, Sep. 2020, Art. no. 062034, doi: 10.1088/1742-6596/1618/6/062034.

[35] W. C. Skamarock et al., "A description of the advanced research WRF model version 4," Nat. Center Atmos. Res., Boulder, CO, USA, p. 145, 2019.

[36] T. G. Farr et al., "The shuttle radar topography mission," *Rev. Geophys.*, vol. 45, no. 2, pp. 1–33, May 2007, doi: 10.1029/2005RG000183.

[37] "Rapporto Statistico 2021 – Energia da fonti rinnovabili in Italia," Gestore Servizi Energetici, Italy, Last Access: Jun. 27, 2023. [Online]. Available: https://www.gse.it/documenti_site/Documenti%20GSE/Rapporti%20statistici/Rapporto%20Statistico%20GSE%20-%20FER%202021.pdf

[38] C. M. Payne, J. E. Passner, R. E. Dumais, A. Abdelkefi, and C. M. Hocut, "Presence of longitudinal roll structures during synoptic forced conditions in complex terrain," *Atmosphere*, vol. 12, no. 6, Jun. 2021, Art. no. 737, doi: 10.3390/atmos12060737.

[39] P. Sanò, G. Panegrossi, D. Casella, A. C. Marra, F. Di Paola, and S. Dietrich, "The new passive microwave neural network precipitation retrieval (PNPR) algorithm for the cross-track scanning ATMS radiometer: Description and verification study over Europe and Africa using GPM and TRMM spaceborne radars," *Atmos. Meas. Techn.*, vol. 9, no. 11, pp. 5441–5460, Nov. 2016, doi: 10.5194/amt-9-5441-2016.

[40] E. A. Munoz, F. Di Paola, and M. A. Lanfri, "Advances on rain rate retrieval from satellite platforms using artificial neural networks," *IEEE Latin Amer. Trans.*, vol. 13, no. 10, pp. 3179–3186, Oct. 2015, doi: 10.1109/TLA.2015.7387219.

[41] M. Riedmiller and H. Braun, "A direct adaptive method for faster backpropagation learning: The RPROP algorithm," in *Proc. IEEE Int. Conf. Neural Netw.*, 1993, vol. 1, pp. 586–591, doi: 10.1109/ICNN.1993.298623.

[42] K. Levenberg, "A method for the solution of certain non-linear problems in least squares," *Quart. Appl. Math.*, vol. 2, no. 2, pp. 164–168, 1944, doi: 10.1090/qam/10666.

[43] D. W. Marquardt, "An algorithm for least-squares estimation of nonlinear parameters," *J. Soc. Ind. Appl. Math.*, vol. 11, no. 2, pp. 431–441, 1963, doi: 10.1137/0111030.

[44] Z. Cömert and A. Kocamaz, "A study of artificial neural network training algorithms for classification of cardiotocography signals," *Bitlis Eren Univ. J. Sci. Technol.*, vol. 7, no. 2, pp. 93–103, 2017, doi: 10.17678/beuscitech.338085.

[45] L. M. Saini, "Peak load forecasting using Bayesian regularization, resilient and adaptive backpropagation learning based artificial neural networks," *Electr. Power Syst. Res.*, vol. 78, no. 7, pp. 1302–1310, Jul. 2008, doi: 10.1016/j.epsr.2007.11.003.

[46] P. Malik, A. Gehlot, R. Singh, L. R. Gupta, and A. K. Thakur, "A review on ANN based model for solar radiation and wind speed prediction with real-time data," *Arch. Comput. Methods Eng.*, vol. 29, pp. 3183–3201, Jan. 2022, doi: 10.1007/s11831-021-09687-3.

[47] H. Wang, W. C. Skamarock, and G. Feingold, "Evaluation of scalar advection schemes in the advanced research WRF model using large-eddy simulations of aerosol–cloud interactions," *Monthly Weather Rev.*, vol. 137, no. 8, pp. 2547–2558, Aug. 2009, doi: 10.1175/2009MWR2820.1.

[48] J. J. Danielson and D. B. Gesch, "Global multi-resolution terrain elevation data 2010 (GMTED2010)," U.S. Geological Survey Open-File Rep. 2011–1073, U.S. Dept. Interior, Washington, DC, USA, p. 26, 2011.

[49] G. Büttner, T. Soukup, and B. Kosztra, "CLC2012 addendum to CLC2006 technical guidelines," Copenhagen, Denmark: Final draft, Aug. 2014.

[50] P. A. Jimenez et al., "WRF-Solar: Description and clear-sky assessment of an augmented NWP model for solar power prediction," *Bull. Amer. Meteorological Soc.*, vol. 97, no. 7, pp. 1249–1264, Jul. 2016, doi: 10.1175/BAMS-D-14-00279.1.

[51] G. Thompson and T. Eidhammer, "A study of aerosol impacts on clouds and precipitation development in a large winter cyclone," *J. Atmos. Sci.*, vol. 71, no. 10, pp. 3636–3658, Oct. 2014, doi: 10.1175/JAS-D-13-0305.1.

[52] T. Yamaguchi and G. Feingold, "Large-eddy simulation of cloudy boundary layer with the advanced research WRF model," *Proc. J. Adv. Model. Earth Syst.*, vol. 4, no. 3, pp. 1–16, Sep. 2012, doi: 10.1029/2012MS000164.

[53] C. H. Moeng, J. Dudhia, J. Klemp, and P. Sullivan, "Examining two-way grid nesting for large eddy simulation of the PBL using the WRF model," *Monthly Weather Rev.*, vol. 135, no. 6, pp. 2295–2311, Jun. 2007, doi: 10.1175/MWR3406.1.

[54] B. Zhou, J. S. Simon, and F. K. Chow, "The convective boundary layer in the terra incognita," *J. Atmos. Sci.*, vol. 71, no. 7, pp. 2545–2563, Jul. 2014, doi: 10.1175/JAS-D-13-0356.1.

[55] R. K. Rai et al., "Evaluation of the impact of horizontal grid spacing in terra incognita on coupled mesoscale–microscale simulations using the WRF framework," *Monthly Weather Rev.*, vol. 147, no. 3, pp. 1007–1027, Mar. 2019, doi: 10.1175/MWR-D-18-0282.1.

[56] S. E. Haupt et al., "On bridging a modeling scale gap: Mesoscale to microscale coupling for wind energy," *Bull. Amer. Meteorological Soc.*, vol. 100, no. 12, pp. 2533–2550, Dec. 2019, doi: 10.1175/BAM-S-D-18-0033.1.

[57] R. K. Rai, L. K. Berg, B. Kosović, J. D. Mirocha, M. S. Pekour, and W. J. Shaw, "Comparison of measured and numerically simulated turbulence statistics in a convective boundary layer over complex terrain," *Boundary-Layer Meteorol.*, vol. 163, no. 1, pp. 69–89, Nov. 2016, doi: 10.1546/s10546-016-0217-y.

[58] Z. Zhang et al., "Convection-permitting fully coupled WRF-Hydro ensemble simulations in high mountain environment: Impact of boundary layer-and lateral flow parameterizations on land–atmosphere interactions," *Climate Dyn.*, vol. 59, pp. 1355–1376, 2022, doi: 10.1007/s00382-021-06044-9.

[59] J. Arnault et al., "Precipitation sensitivity to the uncertainty of terrestrial water flow in WRF-Hydro: An ensemble analysis for central Europe," *J. Hydrometeorol.*, vol. 19, no. 6, pp. 1007–1025, 2018, doi: 10.1175/JH-M-D-17-0042.1.

[60] P. A. Jiménez, J. Navarro, A. M. Palomares, and J. Dudhia, "Mesoscale modeling of offshore wind turbine wakes at the wind farm resolving scale: A composite-based analysis with the weather research and forecasting model over Horns Rev," *Wind Energy*, vol. 18, no. 3, pp. 559–566, 2015, doi: 10.1002/we.1708.

[61] D. P. Dee et al., "The ERA-Interim reanalysis: Configuration and performance of the data assimilation system," *Quart. J. Roy. Meteorological Soc.*, vol. 137, no. 656, pp. 553–597, 2011, doi: 10.1002/qj.828.

[62] J. Zhang and J. Li, *Spatial Cognitive Engine Technology*. Amsterdam, The Netherlands: Elsevier, 2023.

[63] F. Cabello, J. León, Y. Iano, and R. Arthur, "Implementation of a fixed-point 2D Gaussian filter for image processing based on FPGA," in *Proc. Signal Process., Algorithms, Architectures, Arrangements, Appl.*, 2015, pp. 28–33, doi: 10.1109/SPA.2015.7365108.

[64] J. A. Sobrino and J. C. Jiménez-Muñoz, "Minimum configuration of thermal infrared bands for land surface temperature and emissivity estimation in the context of potential future missions," *Remote Sens. Environ.*, vol. 148, pp. 158–167, May 2014, doi: 10.1016/j.rse.2014.03.027.

[65] A. Q. Valenzuela and J. C. G. Reyes, "Basic spatial resolution metrics for satellite imagers," *IEEE Sensors J.*, vol. 19, no. 13, pp. 4914–4922, Jul. 2019, doi: 10.1109/JSEN.2019.2902512.

[66] F. Di Paola and S. Dietrich, "Resolution enhancement for microwave-based atmospheric sounding from geostationary orbits," *Radio Sci.*, vol. 43, no. 6, pp. 1–14, Dec. 2008, doi: 10.1029/2007RS003789.

[67] M. Frigo and S. G. Johnson, "FFTW: An adaptive software architecture for the FFT," in *Proc. IEEE Int. Conf. Acoust., Speech Signal Process.*, 1998, vol. 3, pp. 1381–1384, doi: 10.1109/ICASSP.1998.681704.

[68] P. Podder, T. Z. Khan, M. H. Khan, and M. M. Rahman, "Comparative performance analysis of Hamming, Hanning and Blackman window," *Int. J. Comput. Appl.*, vol. 96, no. 18, pp. 1–7, Jun. 2014, doi: 10.5120/16891-6927.

[69] A. Broström and K. Mølhave, "Spatial image resolution assessment by Fourier analysis (SIRAF)," *Microsc. Microanalysis*, vol. 28, no. 2, pp. 469–477, Apr. 2022, doi: 10.1017/S1431927622000228.

[70] M. Nixon and A. Aguado, *Feature Extraction and Image Processing for Computer Vision*. New York, NY, USA: Academic, 2019.

[71] P. Enevoldsen and G. Xydis, "Examining the trends of 35 years growth of key wind turbine components," *Energy Sustain. Develop.*, vol. 50, pp. 18–26, Jun. 2019, doi: 10.1016/j.esd.2019.02.003.

[72] M. Bilodeau and D. Brenner, "Principal components," in *Theory of Multivariate Statistics*. Berlin, Germany: Springer, 1999, pp. 161–173, doi: 10.1007/978-0-387-22616-3_10.

[73] W. Tan, L. Tian, H. Shen, and C. Zeng, "A new downscaling-calibration procedure for TRMM precipitation data over Yangtze river economic belt region based on a multivariate adaptive regression spline model," *IEEE Trans. Geosci. Remote Sens.*, vol. 60, 2022, Art. no. 4702819, doi: 10.1109/TGRS.2021.3087896.

[74] B. S. Sharratt and V. Vaddella, "Threshold friction velocity of crusted windblown soils in the Columbia Plateau," *Aeolian Res.*, vol. 15, pp. 227–234, Dec. 2014, doi: 10.1016/j.aeolia.2014.08.002.

[75] J. L. Laughner, A. Zare, and R. C. Cohen, "Effects of daily meteorology on the interpretation of space-based remote sensing of NO2," *Atmos. Chem. Phys.*, vol. 16, no. 23, pp. 15247–15264, Dec. 2016, doi: 10.5194/acp-16-15247-2016.

[76] E. P. Agbo and C. Edet, "Meteorological analysis of the relationship between climatic parameters: Understanding the dynamics of the troposphere," *Theor. Appl. Climatol.*, vol. 150, pp. 1677–1698, Oct. 2021, doi: 10.1007/s00704-022-04226-x.

[77] D. Bolton, "The computation of equivalent potential temperature," *Monthly Weather Rev.*, vol. 108, no. 7, pp. 1046–1053, Jul. 1980, doi: 10.1175/1520-0493(1980)108<1046:TCOEPT>2.0.CO;2.

[78] A. Zheng and A. Casari, *Feature Engineering for Machine Learning: Principles and Techniques for Data Scientists*. Sebastopol, CA, USA: O'Reilly Media, 2018.

[79] M. Duda, "The WRF preprocessing system: Description of general functions," Joint NCAR-NCAS WRF Tutorial, Edinburgh, U.K., 2011.

[80] P. Ritter, "A vector-based slope and aspect generation algorithm," *Photogramm. Eng. Remote Sens.*, vol. 53, no. 8, pp. 1109–1111, 1987.

[81] P. A. Burrough, *Principles of Geographic Information Systems for Land Resource Assessment*. Oxford, U.K.: Oxford Science, 1986.

[82] F. Di Paola et al., "MiRTaW: An algorithm for atmospheric temperature and water vapor profile estimation from ATMS measurements using a random forests technique," *Remote Sens.*, vol. 10, no. 9, Sep. 2018, Art. no. 1398, doi: 10.3390/rs10091398.

[83] C. H. Aladag, E. Egrioglu, and C. Kadilar, "Improvement in forecasting accuracy using the hybrid model of ARFIMA and feed forward neural network," *Amer. J. Intell. Syst.*, vol. 2, no. 2, pp. 12–17, 2012, doi: 10.5923/j.ajis.20120202.02.

[84] J. Snoek, H. Larochelle, and R. P. Adams, "Practical Bayesian optimization of machine learning algorithms," in *Advances in Neural Information Processing Systems*, vol. 25. F. Pereira, Ed., Glasgow, U.K.: Curran Associates, 2012, pp. 2951–2959.

[85] H. Yonaba, F. Anctil, and V. Fortin, "Comparing sigmoid transfer functions for neural network multistep ahead streamflow forecasting," *J. Hydrologic Eng.*, vol. 15, no. 4, pp. 275–283, Mar. 2010, doi: 10.1061/(ASCE)HE.1943-5584.0000188.

[86] F. Scarselli and A. C. Tsoi, "Universal approximation using feedforward neural networks: A survey of some existing methods, and some new results," *Neural Netw.*, vol. 11, no. 1, pp. 15–37, Jan. 1998, doi: 10.1016/S0893-6080(97)00097-X.

[87] R. Hecht-Nielsen, "Theory of the backpropagation neural network," in *Neural Networks for Perception*. New York, NY, USA: Academic, 1992, pp. 65–93, doi: 10.1016/B978-0-12-741252-8.50010-8.

[88] A. J. Thomas, M. Petridis, S. D. Walters, S. M. Gheytassi, and R. E. Morgan, "Two hidden layers are usually better than one," in *International Conference on Engineering Applications of Neural Networks, Communications in Computer and Information Science*, vol. 744. Berlin, Germany: Springer, 2017, pp. 279–290, doi: 10.1007/978-3-319-65172-9_24.

[89] C. R. M. Ibnu, J. Santoso, and K. Surendro, "Determining the neural network topology: A review," in *Proc. 8th Int. Conf. Softw. Comput. Appl.*, 2019, pp. 357–362, doi: 10.1145/3316615.3316697.

[90] G. Castellano and A. M. Fanelli, "Variable selection using neural-network models," *Neurocomputing*, vol. 31, no. 1/4, pp. 1–13, Mar. 2022, doi: 10.1016/S0925-2312(99)00146-0.

[91] C. C. Paige and M. A. Saunders, "LSQR: An algorithm for sparse linear equations and sparse least squares," *ACM Trans. Math. Softw.*, vol. 8, no. 1, pp. 43–71, 1982, doi: 10.1145/355984.355989.

[92] M. R. Hestenes and E. Stiefel, "Methods of conjugate gradients for solving," *J. Res. Nat. Bur. Standards*, vol. 49, no. 6, pp. 409–436, Dec. 1952.

[93] M. An, "A simple method for determining the spatial resolution of a general inverse problem," *Geophysical J. Int.*, vol. 191, no. 2, pp. 849–864, 2012, doi: 10.1111/j.1365-246X.2012.05661.x.

[94] T. Knopp, S. Biederer, T. F. Sattel, M. Erbe, and T. M. Buzug, "Prediction of the spatial resolution of magnetic particle imaging using the modulation transfer function of the imaging process," *IEEE Trans. Med. Imag.*, vol. 30, no. 6, pp. 1284–1292, Jun. 2011, doi: 10.1109/TMI.2011.2113188.

[95] G. Duveiller and P. Defourny, "A conceptual framework to define the spatial resolution requirements for agricultural monitoring using remote sensing," *Remote Sens. Environ.*, vol. 114, no. 11, pp. 2637–2650, 2010, doi: 10.1016/j.rse.2010.06.001.

[96] R. Mizutani et al., "A method for estimating spatial resolution of real image in the Fourier domain," *J. Microsc.*, vol. 261, no. 1, pp. 57–66, 2016, doi: 10.1111/jmi.12315.

[97] W. Tan, L. Tian, H. Shen, and C. Zeng, "A new downscaling-calibration procedure for TRMM precipitation data over Yangtze river economic belt region based on a multivariate adaptive regression spline model," *IEEE Trans. Geosci. Remote Sens.*, vol. 60, 2022, Art. no. 4702819, doi: 10.1109/TGRS.2021.3087896.

[98] Y. Kim and N.-W. Park, "Comparison of regression models for spatial downscaling of coarse scale satellite-based precipitation products," in *Proc. IEEE Int. Geosci. Remote Sens. Symp.*, 2017, pp. 4634–4637.

[99] J. Hu, X. Wu, and J. Zhou, "Noise robust single image super-resolution using a multiscale image pyramid," *Signal Process.*, vol. 148, pp. 157–171, 2018, doi: 10.1016/j.sigpro.2018.02.020.

[100] J. Immerkaer, "Fast noise variance estimation," *Comput. Vis. Image Understanding*, vol. 64, no. 2, pp. 300–302, 1996, doi: 10.1006/cviu.1996.0060.

[101] F. Bañuelos-Ruedas, C. Angeles-Camacho, and S. Rios-Marcuello, "Analysis and validation of the methodology used in the extrapolation of wind speed data at different heights," *Renewable Sustain. Energy Rev.*, vol. 14, no. 8, pp. 2383–2391, Oct. 2010, doi: 10.1016/j.rser.2010.05.001.

[102] S. Lawrence, C. L. Giles, and A. C. Tsoi, "Lessons in neural network training: Overfitting may be harder than expected," in *Proc. 14th Nat. Conf. Artif. Intell.*, 1997, pp. 540–545.

[103] M. S. Adaramola, M. Agelin-Chaab, and S. S. Paul, "Assessment of wind power generation along the coast of Ghana," *Energy Convers. Manage.*, vol. 77, pp. 61–69, Jan. 2014, doi: 10.1016/j.enconman.2013.09.005.

[104] P. Wais, "Two and three-parameter Weibull distribution in available wind power analysis," *Renewable Energy*, vol. 103, pp. 15–29, 2017, doi: 10.1016/j.renene.2016.10.041.

[105] H. Leung and S. Haykin, "The complex backpropagation algorithm," *IEEE Trans. Signal Process.*, vol. 39, no. 9, pp. 2101–2104, Sep. 1991, doi: 10.1109/78.134446.

[106] K. L. Du and M. N. S. Swamy, "Multilayer perceptrons: Architecture and error backpropagation," in *Neural Networks and Statistical Learning*. Berlin, Germany: Springer, 2014, pp. 83–126, doi: 10.1007/978-1-4471-5571-3_4.

[107] A. D. Anastasiadis, G. D. Magoulas, and M. N. Vrahatis, "New globally convergent training scheme based on the resilient propagation algorithm," *Neurocomputing*, vol. 64, pp. 253–270, Mar. 2005, doi: 10.1016/j.neucom.2004.11.016.

[108] S. M. Awan, Z. A. Khan, and M. Aslam, "Solar generation forecasting by recurrent neural networks optimized by Levenberg-Marquardt algorithm," in *Proc. IEEE 44th Annu. Conf. Ind. Electron. Soc.*, 2018, pp. 276–281, doi: 10.1109/IECON.2018.8591799.

[109] L. Xiao, X. Chen, and X. Zhang, "A joint optimization of momentum item and Levenberg-Marquardt algorithm to level up the BPNN's generalization ability," *Math. Probl. Eng.*, vol. 2014, Apr. 2014, Art. no. 653072, doi: 10.1155/2014/653072.

Francesco Di Paola received the university degree in physics from "Sapienza" University, Rome, Italy, in 2004, and the Ph.D. degree in geophysics from University "Alma Mater Studiorum," Bologna, Italy, in 2008.

Since 2008, he has been a Researcher with the National Research Council of Italy. His past research was focused mainly on rainfall estimation and nowcasting with multisensor approach combining microwave and infrared (MW-IR) satellite data with lightning data from surface networks. His research activities primarily focused on atmospheric satellite remote sensing using MW and IR passive radiometers. His current work involves the satellite retrieval of temperature and humidity vertical profile, techniques and algorithms development to increase the spatial resolution of remotely sensed data, and mesoscale atmospheric circulation numerical model for weather analysis and forecasting.

Domenico Cimini received the laurea (*cum laude*) and Ph.D. degrees in physics from the University of L'Aquila, L'Aquila, Italy, in 1998 and 2002, respectively.

He is a Research Manager with the National Research Council of Italy, Institute of Methodologies for the Environmental Monitoring (CNR-IMAA), Potenza, Italy. Since 2002, he has been a Researcher with the Center of Excellence for Remote Sensing and Modeling of Severe Weather, L'Aquila, a Research Assistant with the Cooperative Institute for Research in Environmental Sciences, University of Colorado, Boulder, CO, USA, and an Adjunct Professor with the Department of Electrical and Computer Engineering, University of Colorado, Boulder. He has more than 20-year experience with ground- and satellite-based passive remote sensing, particularly microwave radiometry. He lead and participated in several international projects funded by EUMETSAT and the European Space Agency.

Dr. Cimini is the Vice Chair of the EU COST Action CA18235 PROBE, grouping participants from more than 37 European and non-European countries, and Vice Chair of the World Meteorological Organization (WMO) Expert Team on Upper-Air Measurement. He is also the Chair of the Expert Team on Microwave Radiometers Profilers within the EUMETNET E-PROFILE Program and a Cochair of the Ground-Based Task Team of the WMO Global Climate Observing System Reference Upper Air Network. He is a Life Member of the European Geophysical Union. He was the recipient of the Fondazione Ugo Bordoni Award 2008 in memory of Prof. G. D'Auria, and the 6th Hans Liebe Lectureship bestowed by the U.S. National Committee for the Union of Radio Scientists Internationale, 2019.

Maria Pia De Natale received the High School Diploma of Surveyor in 1990.

She is currently a Technical Collaborator with the National Research Council of Italy, Institute of Methodologies for the Environmental Monitoring (CNR-IMAA), Potenza, Italy. Since 2019, she has been collaborating with the Satellite Remote Sensing for Clouds and Precipitations Research Group of the CNRIMAA.

Donatello Gallucci received the master's degree in experimental physics from Siena University, Siena, Italy, in 2014, and the Ph.D. degree in applied mathematics (to physics) from Newcastle University, Newcastle upon Tyne, U.K., in 2013.

Since 2015, he has been a one-year Postdoc Research Fellow with the Joint Quantum Institute (Newcastle-Durham, U.K.), three-year Postdoc Research Fellow with the Institute of Methodologies for Environmental Analysis, National Research Council in Italy, and finally a full-time tenure Researcher with the National Research Council, after the successful national competition in 2019. He has more than seven-year experience with satellite-based passive remote sensing, radiative transfer modeling, statistical and physical retrieval techniques, as well as developing new methods for short-term forecasting at midlatitude of severe weather and surface solar irradiance based on active and passive remote sensing in the visible, infrared and microwave spectral regions, using ground or space-borne sensors aboard geostationary and polar satellites. He participated in several international projects funded by the EU and Italian research frameworks.

Sabrina Gentile received the master's and Ph.D. degrees in physics from the University of L'Aquila, L'Aquila, Italy, in 2007 and 2011, respectively.

She is a Research Scientist with CNR-IMAA, Potenza, Italy, and also affiliated with the Center of Excellence for Remote Sensing and Modeling of Severe Weather (CETEMPS), University of L'Aquila. She has more than ten-year experience in atmospheric physics, meteorological modeling, and convective events. She has been the Topic Editor for *Remote Sensing* since 2020. She contributed to several national and international projects funded by the Italian Ministry of Economic Development (SOLARCLOUD, SPOT), EU (CAPRADNET), ESA (WRAD), and EUMETSAT (VICIRS). Her research activity focuses on mesoscale numerical weather prediction modeling and data assimilation, particularly dedicated to the optimization of renewable energy harvest (wind and solar).

Edoardo Geraldi received the M.Sc. degree in engineering from the University of Basilicata (UniBas), Potenza, Italy, in 1996.

In 2001, he joined the Italian National Research Council, Institute for Archaeological and Monumental Heritage, and in 2018, he joined the Institute of Methodologies for Environmental Analysis. During 2005–2012, he was an Adjunct Professor with the Faculty of Engineering, UniBas, Potenza, in the course of renewable energy technology. His current research interest focuses on renewable energy resource assessment and forecast.

Salvatore Larosa received the laurea degree in geology and the Ph.D. degree in environmental science and engineering, construction and energy from the University of Calabria, Rende, Italy, in 2002 and 2020, respectively.

He is a Research Scientist with the National Research Council of Italy, Institute of Methodologies for the Environmental Monitoring (CNR-IMAA), Potenza, Italy. He has participated in several international projects funded by EUMETSAT and the European Space Agency. His research interests concern Earth observations from space/remote sensing, meteorology, atmospheric modeling and dynamics, clouds and precipitations, and microwave radiometry. He has more than ten-year experience with storing and managing remotely sensed data in multidimensional databases, collecting data and analyzing for trends, using statistical techniques and programming software to create algorithms and predictive models, creating tools for data interoperability, sharing and visualizations, data management systems, information retrieval and digital libraries, data fusion, and machine learning.

Saverio Teodosio Nilo received the M.S. degree in telecommunication engineering from the University of Pise, Pise, Italy, in 2012, and the Ph.D. degree in environmental engineering from the University of Basilicata, Potenza, Italy, in 2018, with a specialization in the processing of remote sensed data for atmospheric physics applications.

Since June 2013, he has been a Researcher with the National Research Council of Italy, Institute of Methodologies for the Environmental Monitoring (CNR-IMAA), Potenza. His research deals with satellite remote sensing of clouds and precipitations. One main activity has covered the prediction of incident solar radiance at specific points of the Earth's surface, also in nonstandard atmospheric conditions such as fog or snow, applied to the estimation of energy production from renewable sources. Over the last years, he has been involved, also with the scientific responsibility, in research activities focused on the Earth-space communication systems such as the ESA-funded WRad and REFDAT4ESAMWR projects aimed at characterizing the tropospheric attenuation or at defining a reference set of data and algorithms to be used in operations to monitor the radiometric accuracy of a microwave radiometer network.

Mariassunta Viggiano received the master's degree in mathematics from the University of Basilicata, Potenza, Italy, in 1997.

She then joined the Physics Group of the Faculty of Science, University of Basilicata, to study some problems related to elementary particle physics, such as formal aspects of the theory of decay and theoretical predictions of CP violation. Since 1999, she has been involved in research on atmospheric physics. Within this topic, she is mainly interested in radiative transfer models for both clear and cloudy atmospheric conditions, the development and validation of calculation codes for the treatment of the forward and inverse problems of satellite atmospheric sounding, and the analysis of satellite remotely sensed data. Over the years, her scientific activity has also focused on cloud detection over the polar regions and on the development of spatial interpolation schemes for meteorological variables. As part of the activities aimed at optimizing applied meteorological and hydrological modeling, she is involved in the study of temporal sampling and optimal procedures for the calculation and correction of relative humidity and other variables of meteorological interest. She is also interested in the application of mathematical-statistical methods to support the interpretation of chemical and biochemical problems.

Elisabetta Ricciardelli received the M.S. degree in physics from the University of Bologna, Bologna, Italy, in 1998, and the Ph.D. degree in methods and technologies for environmental monitoring from the University of Basilicata, Potenza, Italy, in 2008.

In 2005, she was with the National Research Council of Italy, Institute of Methodologies for the Environmental Monitoring. Her research activity mainly concerns cloud detection and classification.

Filomena Romano received the M.S. degree in physics from the University of Bologna, Bologna, Italy, in 1990.

In 1992, she joined the Institute of Methodologies for Environmental Analysis, Tito Scalo, Italy, where she got experience in experimental and theoretical studies in atmospheric remote sensing. She collaborated in studies concerning the retrieval of atmospheric aerosol from solar spectra at ground level. She has currently specialized in satellite data handling for meteorological and climatological studies. Her main research interests include cloud detection, cloud clearing, and cloud microphysical retrieval of infrared and microwave radiance from space-borne sensors are her main activities.

Ermann Ripepi received the High school diploma in electronics and telecommunications, in 2004.

He has been an ICT Technician with the National Research Council of Italy, Institute of Methodologies for Environmental Monitoring (CNR-IMAA), Potenza, Italy, since 2007. He has more than 15 years of experience in data center infrastructure management, particularly in the field of cybersecurity, networking, and virtualization environments. Currently, at CNR-IMAA, he holds the position of ICT Services Manager and APM GARR. He also manages the ICT infrastructure of the ACTRIS data center for aerosol profiling (ARES) of the Research Infrastructure ACTRIS. He has also gained experience in managing IT infrastructures dedicated to the reception and processing of data from satellite platforms (GEO/LEO), aerial, and ground sensors. He has been a member of the Italian Chapter of the Internet Society since 2012 and a member of the council since 2021.